UNIVERSIDADE
BEIRA INTERIOR

Simulation of heat transfer of carbon fibres felts and microstructure effects on thermal conductivity of carbon/phenolic ablators

(Versão final após defesa)

Diana Isabel Ribeiro Martins

Dissertação para obtenção do Grau de Mestre em

Engenharia Aeronáutica

(mestrado integrado)

Orientador: Prof. Doutor Pedro Vieira Gamboa

Co-orientador: Prof. Doutor Thierry Magin

Junho de 2023

Declaração de Integridade

Eu, Diana Isabel Ribeiro Martins, que abaixo assino, estudante com o número de inscrição 39704 do Mestrado Integrado em Engenharia Aeronáutica da Faculdade de Engenharia, declaro ter desenvolvido o presente trabalho e elaborado o presente texto em total consonância com o **Código de Integridades da Universidade da Beira Interior**.

Mais concretamente afirmo não ter incorrido em qualquer das variedades de Fraude Académica, e que aqui declaro conhecer, que em particular atendi à exigida referenciação de frases, extratos, imagens e outras formas de trabalho intelectual, e assumindo assim na íntegra as responsabilidades da autoria.

Universidade da Beira Interior, Covilhã 22/06/2023

Assinado por: **Diana Isabel Ribeiro Martins**
Num. de Identificação: 14694857
Data: 2023.06.22 11:43:21+02'00'

Dedicatória

Dedicado à minha família que sempre me incentivou a seguir os meus sonhos e a acreditar que eu era capaz de os concretizar. Ao meu namorado, pelo seu incondicional apoio ao longo desta desafiante caminhada. A todos o meu maior obrigado.

Agradecimentos

Words cannot describe how grateful I am to everyone that helped me with their contribution or support during six demanding months of internship to make this thesis possible.

First of all, I would like to thank Professor Pedro Gamboa for his guidance, time and for agreeing to have me as his master's thesis student working outside our university.

I want to share my appreciation to Professor Thierry Magin for his constant guidance and support dedicated to this project and for all the feedback given.

I could not have undertaken this journey without my advisor, Francisco, whose invaluable patience, continuous support and help over these months made this challenging experience possible to accomplish. Thanks for all the knowledge and expertise shared, for always being available and for the time spent in the numerous meetings that I needed. You have my deepest gratitude. Se lo agradezco de corazón.

I also want to express my thankfulness to Bernd and Alessandro for their help, feedback and for all the meetings where they generously shared their understanding with me.

To everyone working in the von Karman institute, especially to all the friends that I made, thanks for making me feel comfortable so quickly in another country. In those six months, you made me feel at home.

Não tenho palavras para expressar o quanto agradeço aos meus pais, à minha madrinha e aos meus avós, que sempre me apoiaram incondicionalmente nos meus sonhos e acreditaram em mim. Apesar da distância e das inúmeras saudades, a vossa confiança e orgulho em mim manteve-me motivada para conseguir terminar esta etapa. Na distância, iremos sempre achar formas de nos encontrarmos. Quero também agradecer à Milka por todo o entretenimento e apoio emocional que a sua presença me dá.

Ao meu namorado, o grande impulsionador desta jornada, obrigada pela força que sempre me transmitiste, pela paciência, pela tua presença nos bons e nos maus momentos e pelo amor demonstrado nesta longa caminhada que juntos partilhamos.

Não podia deixar de agradecer a todos aqueles que ao longos destes 5 anos fizeram da Covilhã a minha segunda casa.

Resumo

A entrada atmosférica é uma das fases mais críticas das missões de exploração espacial. Os veículos espaciais são equipados com Sistemas de Proteção Térmica (TPS) para garantir a integridade da estrutura perante os intensos fluxos de calor a que é sujeito. Nos últimos anos, materiais leves, como materias ablativos de carbono/fenólicos, tornaram-se a opção preferida como TPS para a entrada atmosférica. Estes materiais são feitos de uma pré-forma de fibra de carbono impregnada com uma resina fenólica e combinam alta porosidade, leveza, baixa densidade e baixa condutividade térmica efetiva.

A modelagem precisa da resposta térmica do TPS requer uma caracterização adequada das propriedades termofísicas. A condutividade térmica efetiva dos materias ablativos de carbono/fenol é um dos fatores mais significativos da transferência de calor para o interior do TPS. Com o aumento das capacidades computacionais, as simulações numéricas de materiais em resolução microescala tornaram-se mais acessíveis, minimizando a necessidade de dispendiosas campanhas experimentais. Isso pode ser alcançado com o software Porous Microstructure Analysis (PuMA) e sua versão em Python, *pumapy*, desenvolvido no NASA Ames Research Center. O principal objetivo deste trabalho é analisar o efeito da microestrutura e das diferentes propriedades intrínsecas na condutividade térmica efetiva.

A primeira etapa consistiu em desenvolver um modelo numérico para o CALCARB CBCF 18-2000, que consiste na pré-forma de carbono do material em estudo, ZURAM, através da geração artificial de um material isotrópico transversal com distribuição normal no plano vertical e uniforme no plano horizontal do material, sendo posteriormente verificado e validado por forma avaliar a influência da microestrutura. Adicionalmente, por forma a analisar o material ZURAM num estado carbonizado gerou-se um cilindro coaxial que se assemelha a um revestimento uniforme no topo das fibras. Para estudar o material no estado virgem, deve-se considerar que o material é composto por fibras, gás e resina fenólica. Para tal, foi implementado um novo gerador de material, que combina o código anterior desenvolvido para o CALCARB com vóxeis uniformemente distribuídos no domínio, que se assemelha ao gás aprisionado no interior do material. Neste último, o meio representa a resina fenólica. Todos os códigos foram posteriormente comparados com dados experimentais disponíveis.

Embora haja um comportamento semelhante dos resultados numéricos com os experimentais, a divergência observada pode residir no fato de algumas das propriedades não serem conhecidas, bem como a condutividade intrínseca das fibras à temperatura dos experimentos.

Apesar de mais desenvolvimentos serem necessários ao nível dos códigos implementados, este trabalho fornece informações importantes sobre o efeito dos diferentes componentes e características geométricas das propriedades microscópicas de materiais ablativos porosos na sua avaliação do modelo macroscópico.

Palavras-chave

Sistemas de proteção térmica, materias ablativos de carbono/fenólicos, condutividade térmica, simulações numéricas microscópicas

Abstract

Atmospheric entry is one of the most critical phases of space exploration missions. Spacecraft are equipped with Thermal Protection Systems (TPS) to ensure the structure's integrity from the encountered intense heat fluxes. In recent years, lightweight materials such as carbon/phenolic ablators have become the preferred option as TPS for atmospheric entry. These materials are made of a carbon fibre preform impregnated with a phenolic resin and combine high porosity, lightweight, low density and low effective thermal conductivity.

Accurate modeling of the thermal response of TPS requires adequate characterization of thermophysical properties. Effective thermal conductivity of carbon/phenolic ablators is one of the most significant factors of heat transfer towards the interior of TPS. With increased computational capabilities, numerical simulations of materials at microscale resolution have become more affordable, minimizing the need for expensive experimental campaigns. This can be achieved with the Porous Microstructure Analysis software (PuMA) and its Python version *pumapy*, developed at NASA Ames Research Center. The main objective of this work is to analyse the effect of the microstructure and the different intrinsic properties on the effective thermal conductivity.

The first step consisted in developing a numerical model for CALCARB CBCF 18-2000, the carbon preform of the material in the study, ZURAM, by artificially generating a transverse isotropic material with a normal distribution in the Through-Thickness (TT) and a uniform distribution in the In-Plane (IP) that was later verified and validated to assess the influence of microstructure. In addition, the charred and virgin ZURAM material was analyzed by generating a coaxial cylinder resembling a uniform coating on the fibre. To stuy the virgin carbon/phenolic, it must be considered that the material comprises fibres, gas and phenolic resin. A new synthetic material generator has been implemented in PuMA, which combines the previous code developed for CALCARB with a generation of uniformly distributed voxels in the domain that mimics the gas trapped inside the material. In the latter, the medium represents the phenolic resin. Both codes were later compared with available experimental data. Although there is a fair agreement between the behaviour of the simulated and measured conductivities, the disparity can reside in the fact that some of the properties are not known such as the fibres' intrinsic conductivity at the experi-

ments' temperature.

Even though further developments are required, this work provides important information about the effect of different components and geometrical features of the microscopic properties of porous ablative materials on their macroscopic model evaluation.

Keywords

Thermal protection systems, carbon/phenolic ablators, thermal conductivity, microscale numerical simulations

Contents

1 Introduction **1**

1.1 Thermal protection systems for atmospheric entries 1

1.2 Importance of micro-structure for thermal protection materials 3

1.3 Thesis objectives and outline 5

2 Physics of lightweight ablators **7**

2.1 Physico-chemical process of thermal protection systems 7

2.2 Porous materials 9

2.2.1 Physical properties of porous materials 9

2.2.2 Fundamentals of heat transfer within porous media 13

2.3 Carbon/phenolic ablator: the ZURAM material 17

2.3.1 Material description and processing 17

2.3.2 Carbon fiber preform properties 19

2.4 Graphitization of carbon fibers 20

3 Simulation tools for porous materials **23**

3.1 Porous Microstructure Analysis Software 24

3.1.1 Domain generation 26

3.1.2 Effective material properties 28

3.1.3 Limitations 32

3.2 Quantity of interest: thermal conductivity 33

3.2.1 Simulation inputs and outputs 34

3.3 Surrogate modelling 35

4 Software development and analysis **37**

4.1 Preliminary study 37

4.1.1 Synthetic material model 37

4.1.2 Study of the microstructure effects on the thermal conductivity . . 41

4.1.3 Sensitivity analysis based on a surrogate model 44

4.2 Development of the CALCARB CBCF 18-2000 material model 49

4.2.1 Validation with experimental data 54

4.3 Material model with fiber coating 56

4.3.1 Verification of the simulated model 59

4.4 Artificial generation of ZURAM virgin material 61

5 Application **63**

5.1 Reproduction of Laser Flash Analysis test cases for fully charred material . 63

5.2 Comparison with experimental data on virgin ZURAM 65

5.3 Assessing the effect of graphitization 69

6 Conclusions and future work **71**

6.1 Conclusions 71

6.2 Recommendations for future work 73

Bibliography **75**

A PuMA effective material properties **85**

A.1 Tortuosity 85

A.2 Electrical conductivity 87

A.3 Permeability 88

A.4 Material response 89

B Conference abstract **91**

List of Figures

1.1 Illustration of an ablative material applied to different spacecraft. 2

1.2 Ablative TPS reentry environments of previous missions demonstrate the vast spectrum of applications. 2

1.3 Importance of each property for both virgin and charred state material. . . 4

1.4 Artificially generation in *pumapy*. 4

2.1 Structure scheme and heat fluxes over a charring ablating surface for the in-depth temperature response of the material. Representation of SEM pictures of both virgin and charred state material. 8

2.2 Representation of the surface recession of a charring ablative material. . . 9

2.3 Illustration of the different phases of a porous composite material. 10

2.4 Schema of a constant volume gas pycnometer. 11

2.5 Schematic illustration of the micro-computed tomography technique. . . . 12

2.6 Representation of the definition of REV for a normalized property. 13

2.7 Principle of the LFA technique for thermal diffusivity measurements. . . . 16

2.8 Illustration diagram of GHP method. 16

2.9 Thermal conductivities of three mediums: vacuum, argon and nitrogen as a function of temperature computed with Mutation++. 19

2.10 Thermal conductivities of CALCARB CBCF 18–2000 under different environments as a function of temperature from Mersen experimental data. . . 19

2.11 Thermal conductivity measurements of rayon-based (TC2) carbon fibers. . 20

3.1 Macroscale and microscale modelling of thermal protection systems. . . . 23

3.2 Visualization of PuMA's workflow. 25

3.3 Schematic of PuMA's software architecture. 26

3.4 Micro-tmography image of a fibrous material and its representation in PuMA. 27

3.5 Random fibers artificially generated in PuMA. 27

3.6 Inputs for random fiber generation and visualization output of the fibers phase on GUI. 27

3.7 The 15 different configurations of Marching Cube algorithm. 30

4.1 Virgin CALCARB CBCF 18-2000 SEM pictures taken at different scales. . . 38

4.2 Representative Elementary Volume analysis in an argon environment. . . 40

4.3 Representative Elementary Volume analysis in a helium environment. . . 40

4.4 Artificially-generated model, representing the CALCARB material using straight solid cylinders in an argon environment 41

4.5 Artificially-generated model, representing the CALCARB material using straight solid cylinders in a helium environment. 41

4.6 Influence of porosity and fibers' orientation in z direction on the effective thermal conductivity. Case for porosity = [0.85, 0.86, 0.89, 0.91, 0.92] and orientation (°) = [15, 18, 20, 22, 25]. 42

4.7 Influence of length and fibers' orientation in z direction on the effective thermal conductivity. Case for length (µm) = [50, 100, 200, 400, 600] and orientation (°) = [15, 18, 20, 22, 25]. 43

4.8 Influence of radius and fibers' orientation in z direction on the effective thermal conductivity. Case for radius (µm) = [4, 5, 6, 7, 8] and orientation (°) = [15, 18, 20, 22, 25]. 43

4.9 Representation of the typical four steps for a sensitivity analysis using SALib 44

4.10 Representation of one-dimensional data interpolation for porosity with 50 training points. 46

4.11 Training accuracy of the proposed surrogate model. 46

4.12 Residual plot describing the difference between actual and predicted values of porosity. 47

4.13 Training accuracy of the proposed surrogate model for three variables. . . 47

4.14 Number of samples required to achieve the convergency of the first-order indices. The porosity is represented in blue, the fiber orientation in green and the length in orange. 48

4.15 Number of samples required to achieve the convergency of the second-order indices. The blue bar represents the influence of porosity-length, the orange bar the effect of porosity-angle and the green bar the impact of the fiber's length-angle on the effective thermal conductivity. 48

4.16 Number of samples required to achieve the convergency of the total-order indices. The porosity is represented in blue, the fiber orientation in green and the length in orange. 48

4.17 Sobol indices are given for each variable accounting for effect on the effective thermal conductivity ($\mathrm{W\,m^{-1}\,K^{-1}}$). 49

4.18 Differences between both implementation of the quantity of fibers present in the IP plane. 50

4.19 Successive steps of the fiber's development. 51

4.20 Visualization of multiple fibers generated centred in the middle of the domain. 51

4.21 Verification of the angle distributions implemented. 51

4.22 2D representation of the periodic boundary conditions applied. 52

4.23 Demonstration of a test case of 1 fiber generated with the applied periodic boundary conditions. 53

4.24 Artificial generation of random straight fibers for a given porosity of 0.89. . 53

4.25 Comparison of experimental and computationally determined values for the effective thermal conductivity of Calcarb CBCF 18-2000 as a function of temperature in an argon environment. 55

4.26 Comparison of experimental and computationally determined values for the effective thermal conductivity of Calcarb CBCF 18-2000 as a function of temperature in a nitrogen environment. 55

4.27 SEM pictures of a charred state material taken at a different scales. 56

4.28 Visualization of the geometrical implementation of the charred resin coating. 57

4.29 2D representation of a possible intersection between fiber and coating and solution. 58

4.30 2D representation of a possible intersection between coated fibers and solution. 59

4.31 Visualization of a slice of the material at the same position for the implementation of the coating in a test case. 59

4.32 SEM micrograph of virgin ZURAM showing the carbon fibers surrounded by the phenolic resin. 61

4.33 Visualization of a slice of the material at the same position along z direction for both implementations. fibers are represented in grey, the phenolic resin in white and the gas trapped in black. 62

5.1 Comparison between the simulations from PuMA and the experiments on LFA (dashed lines) for a final porosity of 0.84 and 0.86 of charred ZURAM. 65

5.2 Comparison between the simulations from PuMA and the experiments on LFA (dashed lines) for both 1 and $0.01\ \mathrm{W\,m^{-1}\,K^{-1}}$ of charred ZURAM. . . 66

5.3 Comparison between the simulations from PuMA and the experiments on LFA (dashed lines) for both porosity of 0.1 and 0.001 for virgin ZURAM material. 68

5.4 The behaviour of the effective thermal conductivity through the heating and cooling process in the TT plane on charred ZURAM. 69

A.1 Microscale oxidation simulation on a carbon fiber preform material, fiberForm. 89

List of Tables

1.1 Influence of the geometry on the effective thermal conductivity ($\mathrm{W\,m^{-1}\,K^{-1}}$). 5

2.1 Thermal conductivity ($\mathrm{W\,m^{-1}\,K^{-1}}$) of CALCARB CBCF 18-2000 at different temperatures and mediums (vacuum, argon, nitrogen). 18

4.1 Comparison of the effective thermal conductivity ($\mathrm{W\,m^{-1}\,K^{-1}}$) values for the in-plane and through-thickness cases obtained through a simulation in a C^{++} and python code. 45

4.2 Possibility matrix of the material intersections at the end of the generation function. 58

4.3 Possibility matrix of the material intersections at the end of each porosity loop. 58

4.4 Test case results comparison. 60

4.5 Comparison of the outcomes of the CALCARB CBCF 18-2000 and coating thermal conductivity simulations in both IP and TT directions. The conditions given are: k_{coat}=k_f=$15.63\,\mathrm{W\,m^{-1}\,K^{-1}}$ and k_{gas}=$0.318\,\mathrm{W\,m^{-1}\,K^{-1}}$. . . 61

5.1 Comparison between the volume fractions measured and simulated for charred ZURAM and error associated. 64

5.2 Comparison between the volume fractions measured and simulated for virgin ZURAM and error associated. Case for spheres generation. 67

5.3 Comparison between the volume fractions measured and simulated for virgin ZURAM and error associated. Case for voxels generation. 67

5.4 Comparison between the volume fractions measured and simulated for virgin ZURAM and error associated. Case for the volume fraction of the gas equal to 0.85. 67

Nomenclature

Roman Symbols

$\mathcal{F}$	Diffusive flux	$[\mathrm{g\,cm^{-2}\,s^{-1}}]$
$\overline{c}$	Mean velocity	$[\mathrm{m\,s^{-1}}]$
cp	Heat capacity	$[\mathrm{J\,kg^{-1}\,K^{-1}}]$
D	Mass diffusivity	$[\mathrm{m^2\,s^{-1}}]$
d	Thickness	$[\mathrm{m}]$
d_f	Fiber's diameter	$[\mu\mathrm{m}]$
l	Representative physical length scale	$[\mathrm{m}]$
l_f	Fiber's length	$[\mu\mathrm{m}]$
P	Pressure	$[\mathrm{Pa}]$
q	Heat flux	$[\mathrm{W^2\,m^{-1}}]$
r	Radius	$[\mu\mathrm{m}]$
T	Temperature	$[\mathrm{K}]$
t	Time	$[\mathrm{s}]$
u	Flow velocity	$[\mathrm{m\,s^{-1}}]$
V	Phase volume	$[\mathrm{m^3}]$
N	Number of voxels	-

Greek Symbols

α	Thermal diffusivity	$[\mathrm{m^2\,s^{-1}}]$
β_R	Extinction coefficient	-
ε	Porosity or void volume fraction	-
η	Turtuosity factor	-
μ	Mean value	-
$\overline{\lambda}$	Mean free path length	$[\mathrm{nm}]$
ϕ	Elevation angle	$[^\circ]$
Φ	Volume fraction	-
ρ	Mass density	$[\mathrm{kg\,m^{-3}}]$
σ	Stefan–Boltzmann constant	$[\mathrm{W\,m^{-2}}]$
σ^2	Covariance	-

σ_e	electrical conductivity	$[\mathrm{S\,m^{-1}}]$
σ_f	Standard deviation of the fiber's angle	[°]
θ	Azimuthal angle	[°]
$\underline{\underline{\kappa}}$	Thermal conductivity tensor	$[\mathrm{W\,m^{-1}\,K^{-1}}]$
k	Thermal conductivity	$[\mathrm{W\,m^{-1}\,K^{-1}}]$

Subscript

C	Chamber
$coat$	Coating
D	Domain
eff	Effective property
f	Fibers or solid phase
g	Gas phase
i	Single phase
int	Intrinsic property
IP	In-Plane
mfp	Mean free path
R	Radiative
ref	Reference
S	Sample
t	Resevoir
T	Total material
tot	Total
TT	Through-Thickness
V	Voxel
xy	In-plane
z	Through-plane

List of Abbreviations

2D	Two Dimensional
3D	Three Dimensional
API	Application Programming Interface
μCT	Micro-Computed Tomography
BiCGSTAB	Bi-Conjugate Stabilized method
DLR	German Aerospace Center
EJFD	Explicit Jump Finite Difference method
ESA	European Space Agency
FD	Finite Difference method
FFT	Fast Fourier Transform
GHP	Guarded Hot Plate
GUI	Graphical User Interface
HTT	Heat Treatment Temperature
ID	Identification
IR	Infrared
IT	In-plane
LFA	Laser Flash Analysis
LTE	Local Thermal Equilibrium
Mutation ++	MUlticomponent Thermodynamic And Transport properties for IONized gases
NASA	National Aeronautics and Space Administration
PICA	Phenolic Impregnated Carbon Ablator
PuMA	Porous Microsctructure Analysis
ReCHAR	Reliable material characterisation methods for Thermal Protection Systems critical ablative materials
REV	Representative Elementary Volume
SA	Surface Area
SEM	Scanning Electron Microscope
SMT	Surrogate Modelling Toolbox
SSA	Specific Surface Area
TIFF	Tag Image File Format
TPS	Thermal Protection Systems

TT	Through-Thickness plane
UBI	Universidade da Beira Interior
VKI	von Karman Institute for Fluid Dynamics
vx	Voxel

Chapter 1

Introduction

1.1 Thermal protection systems for atmospheric entries

Aerospace technologies and space exploration missions started to have rapid development and interest during the Cold War in the 1950s, which culminated with the launch of Sputnik-I in 1957 and the successful landing on the Moon of the first humans during the Apollo program in 1969. For early spaceflight researchers, atmospheric entry was a significant challenge. As Theodore von Karman said: "*re-entry…is perhaps one of the most difficult problems one can imagine… It is certainly a problem that constitutes a challenge to the best brains working in these domains of modern aerophysics…*" When entering to a planet with an atmosphere, the excess kinetic energy that the spacecraft has when it is in orbit has to be dissipated. Thus, the vehicle gets slowed down by friction drag [1]. During the initial stage of reentry, high-speed flow induce a strong shock in front of the vehicle compressing the air to temperatures often greater than $10\,000\,\mathrm{K}$ [2]. Convection of this flow and radiation from the shock progressively heat up the spacecraft which can reach surface temperatures of approximately $3000\,\mathrm{K}$, a temperature that can lead to mission failure.

To mitigate the heat load and protect the spacecraft's integrity, a Thermal Protection System (TPS) is employed. The first concept about protective materials was in 1920 by Robert H. Goddard, that described the material as "*layers of a very infusible hard substance with layers of a poor heat conductor in between.*", similar to a shooting star which ablates during atmospheric entry. Figure 1.1 illustrates the difference in the ablator material before and after atmospheric entry.

There are two main types of TPS classified as reusable or ablative materials, depending on the entry velocity and expected heat load. The present thesis focuses on the ablative TPS since they are the most used in atmospheric entry applications. These absorb the thermal energy and result in mass loss and recession while the remaining virgin solid material insulates the vehicle substructure. A charred porous residue is one product of the resin's

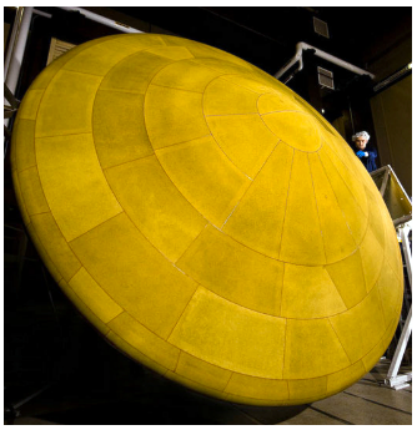

(a) MSL before atmospheric entry.

(b) Apollo 12 Command Module after atmospheric entry.

Figure 1.1: Illustration of an ablative material applied to different spacecraft.

thermal decomposition.

Over the last 40 years, National Aeronautics and Space Administration (NASA) entry probes have employed a few ablative TPS materials. Each mission is different, requiring distinct TPS according to the peak heat flux to which the spacecraft is subjected, as can be noticed from Figure 1.2.

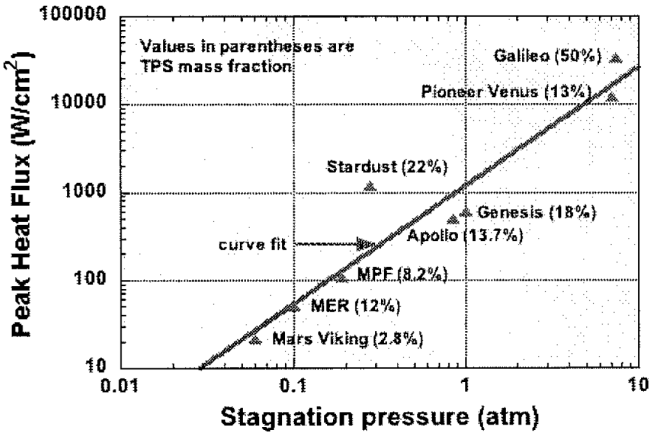

Figure 1.2: Ablative TPS reentry environments of previous missions demonstrate the vast spectrum of applications [3].

The TPS used on early missions, such as the Apollo programme, were dense heavy ablators, but space missions have become more challenging in recent decades, demanding the deployment of new materials. It was necessary to develop advanced TPS materials capable of reducing TPS mass fraction to allow for considerably higher payload masses [4] without compromising the mission due to total weight limitation. The current used ablatives are highly porous materials ($\varepsilon \sim 0.8$) with low densities ($300\,\mathrm{kg\,m^{-3}}$) [5]. This class

of lightweight TPS is made of a short carbon fiber preform impregnated with a phenolic resin, denominated as carbon/phenolic ablators. The Phenolic Impregnated Carbon Ablator (PICA) developed by NASA [5], the European ablator Asterm, developed by Airbus DS and the research material developed by the German Aerospace Center (DRL), ZURAM [6], are three examples of these materials. PICA has already been successfully used on the Stardust mission (2006) [7], on the MSL (2012) [8] and on the Perseverance (2020) [9] mission. PICA-X [10], developed by SpaceX and based on PICA, has also been successfully employed in the Dragon Capsule. Continuous research is necessary to enhance the development of novel materials that promote higher performance and more effective design to meet the more demanding thermal protection requirements of future exploration missions.

The ability to predict complex multiphysics-chemical phenomena inside these materials is of foremost priority for TPS design and margins analysis, preventing mission failure.

1.2 Importance of micro-structure for thermal protection materials

To effectively predict how TPS will perform, it is important to accurately characterize its thermal properties. Most TPS design evaluation still heavily relies on experimental characterization. However, some difficulties are associated with this method, such as the limited temperature range of experimental facilities, the differences in the testing conditions and costs. Numerical modelling of TPS can improve this problem.

Computational tools are able to predict the in-depth temperatures experienced by the internal structure of the material and understanding thermophysical properties and dependence with temperatures. They minimize the need for costly experiments and guide safety margins in the heat shield design process.

Effective thermal conductivity is an important parameter in a porous material to develop a material response code. As seen in Figure 1.3, sensitivity analysis shows that thermal conductivity is an essential parameter for both virgin and char material.

Prediction of effective thermal conductivity can be difficult since it depends on the correct knowledge of the parameters that affect its value, such as porosity, the intrinsic con-

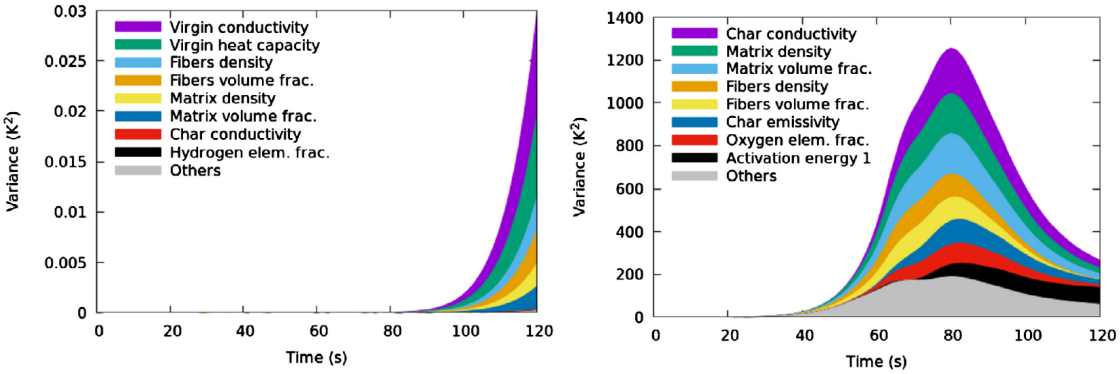

(a) Virgin material. (b) Charred material.

Figure 1.3: Importance of each property for both virgin and charred state material [11].

ductivities of each phase of the material and their microstructure distribution [12]. As an example, two different materials were generated to understand the importance of microstructure in effective thermal conductivity. In the first, random spheres were generated, whereas in the other, these were replaced by random cylinders, which represent the geometry used in this study to represent carbon fibers. Both generations are depicted in Figure 1.4.

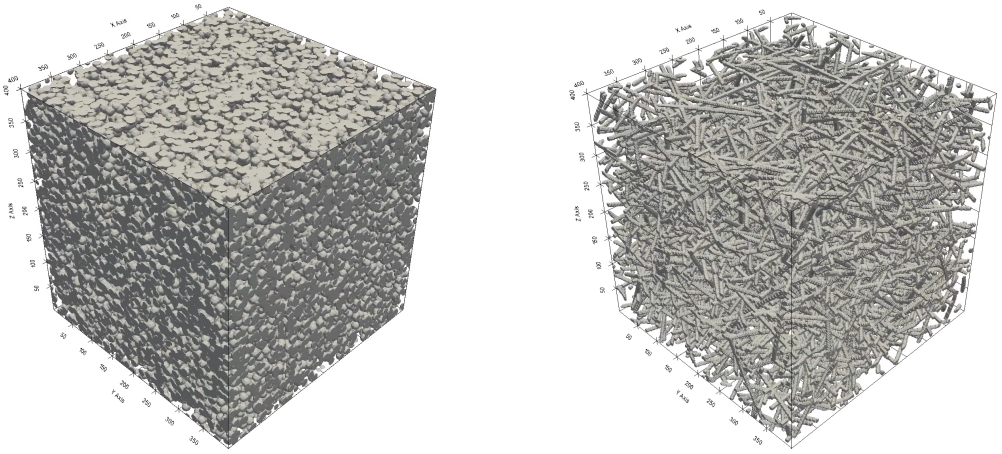

(a) Generation of random spheres. (b) Generation of random fibers.

Figure 1.4: Artificially generation in *pumapy*.

By first setting for both simulations the same domain, volume fractions and intrinsic conductivities of each material's phase and then computing the effective thermal conductivity, it is possible to show that in fact microstructure is important, as showcased in Table 1.1. The results notably differ depending on the geometry. This effect must be studied and understood to improve prediction capabilities.

Table 1.1: Influence of the geometry on the effective thermal conductivity ($\mathrm{W\,m^{-1}\,K^{-1}}$).

	k_{xy}	k_z
Spheres	0.11	0.11
Cylinders	0.97	0.16

1.3 Thesis objectives and outline

This work aims to contribute to the development of advanced numerical tools valuable for the design of TPS. It seeks to answer the following research question:

- How does the microsctructure and properties of carbon fiber felts affect its effective thermal conductivity?

This can be investigated with the Porous Microstructure Analysis software (PuMA) [13] and its Python version *pumapy* [14], developed by NASA Ames Research Center.

In order to answer this question, four objectives were found to be crucial to accomplish. **Objective 1** consists in understanding the effect of different intrinsic properties and geometry on the effective thermal conductivity. To do this, a parametric study is first conducted on a synthetic material model developed that resembles the characteristics of the carbon fiber preform in study followed by a sensitivity analysis based on surrogate modelling of the most important geometrical parameters. **Objective 2** studies the effect of thermal conductivity on charred and virgin resin. The latter is summarized by developing and verifying a material model for both virgin and charred states of the material in study, ZURAM. Once the models are verified, **Objective 3** comprises their comparison to the experimental data available of thermal conductivity at different conditions. Finally, **Objective 4** assesses the impact that graphitization may have on the performance of thermal protection systems.

This thesis is structured into chapters as follows:

- Chapter 2 introduces the fundamentals of the physico-chemical properties and phenomena involving porous materials.
- Chapter 3 provides a description of the PuMA software and an explanation of how properties are computed.

- Chapter 4 presents the development and validation of a synthetic model based on CALCARB CBCF 18-2000 and showcases the study's results on the influence of the geometrical properties of interest on effective thermal conductivity. It also describes the artificial process of generation of both virgin and charred states of ZURAM material and the verification of the developed codes.
- Chapter 5 showcases the results of the comparison of the charred and virgin material models with the experimental data.
- Chapter 6 outlines different results obtained through the development of this work and responds to the research question previously defined. It also proposes foreseen future work.

Chapter 2

Physics of lightweight ablators

In this chapter, an overview of the physical and chemical phenomena that must be accounted for during atmospheric entry in Thermal Protection Systems (TPS) for porous ablators is presented. Afterwards, some properties and concepts for composite materials required for understanding the volume average assumptions of this thesis are defined. Consequently, the necessary background on heat transfer of porous composites is provided. The problem of graphitization of carbon-based materials is also addressed. Finally, this chapter concludes with an introduction and characterization of the TPS applied in this research, ZURAM material, a carbon/phenolic ablator.

2.1 Physico-chemical process of thermal protection systems

This section reviews the ablative heat shield materials in more depth and introduces their main degradation mechanisms. During atmospheric entry, the environment that a spacecraft encounters is very demanding and involves a sequence of physico-chemical processes of TPS materials, which help protect the spacecraft.

As described in Section 1, a strong bow shock appears in front of the spacecraft during the early stage of reentry due to the low-pressure environment and high-speed flow. The shock between the vehicle and the surface generates high temperatures ($10\,000\,\mathrm{K}$) due to chemical dissociation. The heat encountered by the protective material is transferred towards the material's interior by conduction, increasing the composite's temperature.

Ablative TPS absorbs the incoming heat by means of thermal decomposition and material removal. In other words, these heat-shield materials dissipate large heat fluxes through physical and chemical degradation, converting the thermal energy into mass loss and surface recession, while the remaining virgin solid material insulates the body substructure [15, 16]. This process can be divided into two mechanisms: pyrolysis and ablation. Figure 2.1 illustrates the physico-chemical interactions between an ablating material and the

boundary layer.

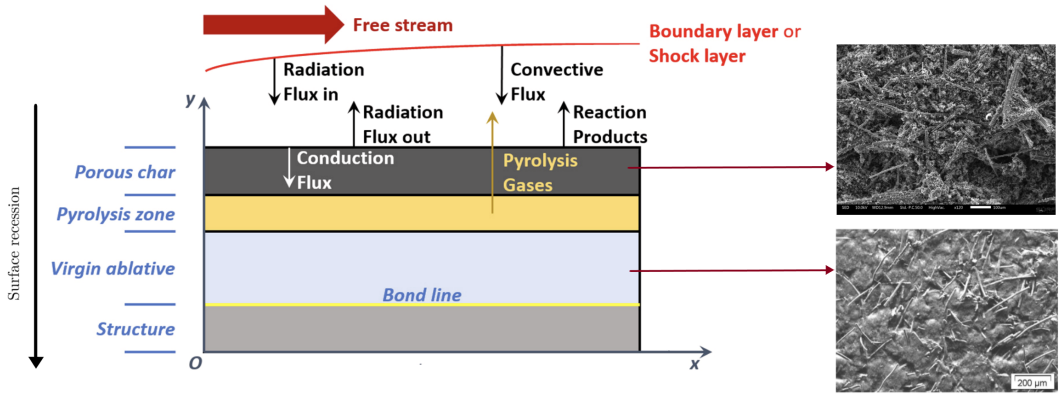

Figure 2.1: Structure scheme and heat fluxes over a charring ablating surface [17] for the in-depth temperature response of the material. Representation of SEM pictures of both virgin and charred state material [18].

As the temperature of the material increases, the resin starts to decompose due to an endothermic process known as pyrolysis. During pyrolysis, the resin is carbonized into a low-density porous char layer, losing around 50 % of its mass and releasing gaseous products. The charred resin protects the material by re-radiating energy. These gases are convected out of the porous char reaching the external heated surface until they are exhausted into the boundary layer, causing a reduction of the convective heat flux acting on the TPS by blowing and undergoing additional chemical reactions [16, 19]. The generation of the hydrocarbon gases mitigates the energy transfer through the material and blowing produces cooling of the boundary layer and creates a blockage effect deflecting part of the incoming flow. Nevertheless, the gases may experience chemical reactions with the boundary layer gases that will also affect the net heating to the surface [20].

The ablation of the char layer, which consists of the carbonized resin and the remaining carbon fibers, is the result of a combination of thermochemical and mechanical processes leading to recession of the heat-shield surface material [21, 2, 22]. Those chemical reactions can be endothermic (vaporization, sublimation) or exothermic [20]. The ablator thickness is a crucial problem in the design of an ablative material since the remaining thickness for a specific mission must be adequate to ensure the effective function of a heat shield and is represented in Figure 2.2.

When exposed to high temperatures, the ablative material transits from a virgin state to a charred state. The resin char stays connected to the carbon fibres after pyrolysis in the form of amorphous carbon structure. When this decomposition occurs earlier in-depth in

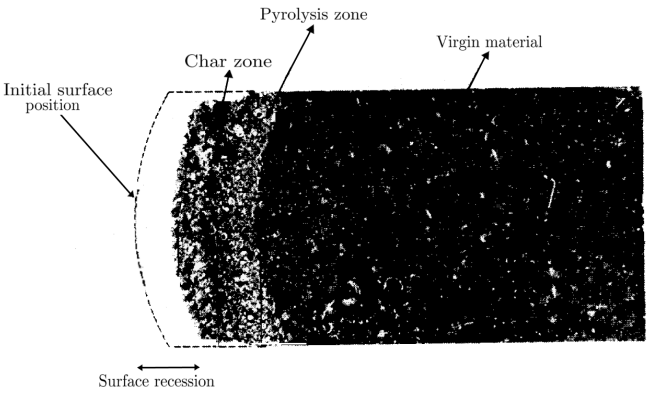

Figure 2.2: Representation of the surface recession of a charring ablative material [23].

the material, the correct characterization of the material properties at this state becomes more meaningful [18]. In Section 5.1, the impact of the char on the effective thermal conductivity is discussed in further detail.

2.2 Porous materials

In this section, the porous solid materials and the features that are of primary interest for the scope of this research will be characterized and described. Lastly, heat transfer and thermal conductivity of porous solids will be addressed with a particular focus on the dominant heat transfer mode within this type of material. Additionally, as material properties are often obtained experimentally, a brief review of the experimental techniques used to characterize them is presented in the following.

2.2.1 Physical properties of porous materials

Porous material are defined simply as any solid containing void space(s), also known as pores, that consists of space not occupied by the main framework of atoms that make up the structure of the solid [24], which are generally saturated by different fluid phases. The void space allows fluid motion through the porous media. A representation of a porous material is depicted in Figure 2.3.

When describing a porous solid it is necessary to define certain concepts that are relatively straightforward but necessary to comprehend the work conducted. The intrinsic and bulk

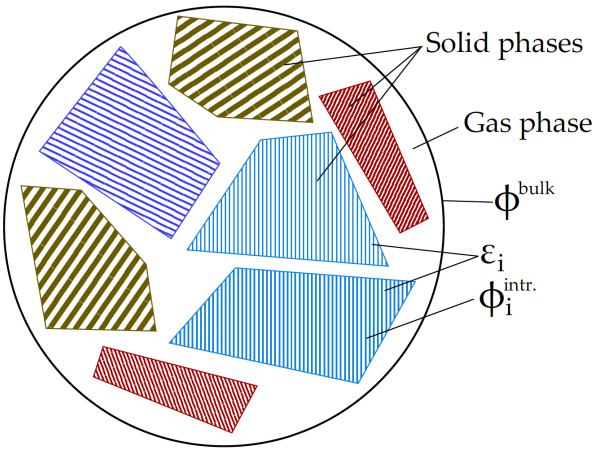

Figure 2.3: Illustration of the different phases of a porous composite material [2].

properties of the material should be distinguished. Intrinsic quantities are associated with a single phase, i, whereas bulk or effective properties are related to the composite. An intrinsic property is defined as the value of the property when the volume fraction of that phase is equal to unity. The bulk property can be related to a specific phase, according to equation 2.1 or to the composite, following equation 2.2 [2].

$$\Phi_i^{\text{bulk}} = f\left(\varepsilon_i, \Phi_i^{\text{intr.}}\right) \quad (2.1)$$

$$\Phi^{\text{bulk}} = f\left(\varepsilon_i, \Phi_i^{\text{intr.}}\right) \quad i \in [0, N_P] \quad (2.2)$$

Each property of a porous solid is a combination of the distinct phases present in the material. As shown in Figure 2.3, each material phase occupies a specific volume denominated as volume fraction, ε_i. It is expressed as the ratio of the volume of the corresponding phase, V_i, with respect to the complete volume of the material, V_T, and follows equation 2.3.

$$\varepsilon_i = \frac{V_i}{V_{\text{T}}} \quad (2.3)$$

The volume fraction of the void phase, also denominated as porosity ε, is a dimensionless quantity, varying from 0 to 1 and often expressed as a percentage. It is computed as the ratio of the total pore (void) volume to the apparent (bulk) volume of the material [25], as

presented in equation 2.4.

$$\varepsilon = \frac{V_{\text{void}}}{V_{\text{T}}} \quad (2.4)$$

For the purpose of this study, for ablative TPS materials, porosity and pore size are significant material properties. Typically, ablative materials feature a high porosity ($\varepsilon > 0.8$), which leads to the ability to dissipate the gaseous phase of the resin through the material, decreasing the effective thermal conductivity [26]. The volume fraction of a material can be measured using non-destructive techniques, such as pycnometry or mirotomographies.

Pycnometry determines the volume of a material by employing Archimedes' principle of fluid displacement and Boyle's law of volume-pressure relationships, respectively, for liquid and gas pycnometers [27]. Helium is the most widely used gas due to its excellent capacity to penetrate small open pores. Gas penetration is affected by pore size and gas molecule diameter. The measured volume excludes the volume filled by open pores but includes the volume occupied by sealed pores inaccessible to the gas. It can be characterized as a simple method, Figure 2.4, possessing many advantages, such as good reproducibility and reliability.

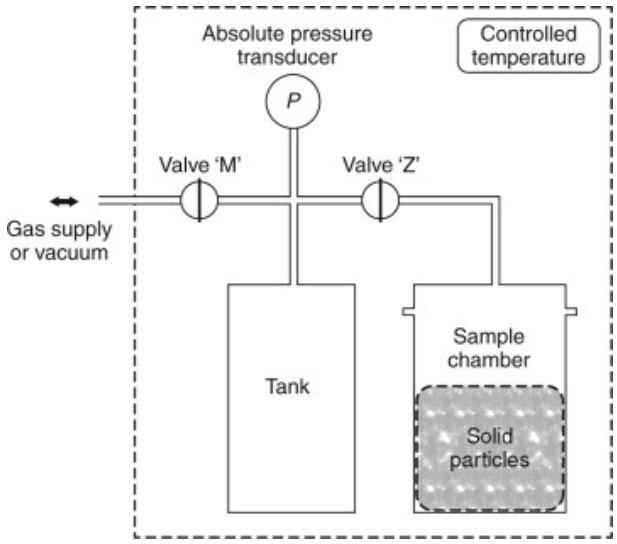

Figure 2.4: Schema of a constant volume gas pycnometer [27].

To obtain the volume of the sample, equation 2.5 can be used considering that the gas acts ideally and that the expanding gas rapidly achieves equilibrium

$$V_S = V_c + V_t \left(P_f - P_j\right) / \left(P_f - P_i\right) \quad (2.5)$$

where V_s represents the sample volume, V_c the sample chamber volume, V_t the reservoir volume and P the pressure at different moments of the experiment. This type of method will be addressed in Chapter 5.

Micro-computed tomography (μCT) is a radiographic imaging non-destructive experimental technique that can produce 3D images of a material's internal structure at a spatial resolution better than 1 μ scale. The scans combine information from a series of 2D X-ray absorption images recorded as the object is rotated about a single axis while pulses are emitted. This series of images are reconstructed to produce a 3D digital image where each voxel represents the X-ray absorption at that point [28]. The resulting 3D images are usually displayed as a series of 2D "slices" as shown in Figure 2.5.

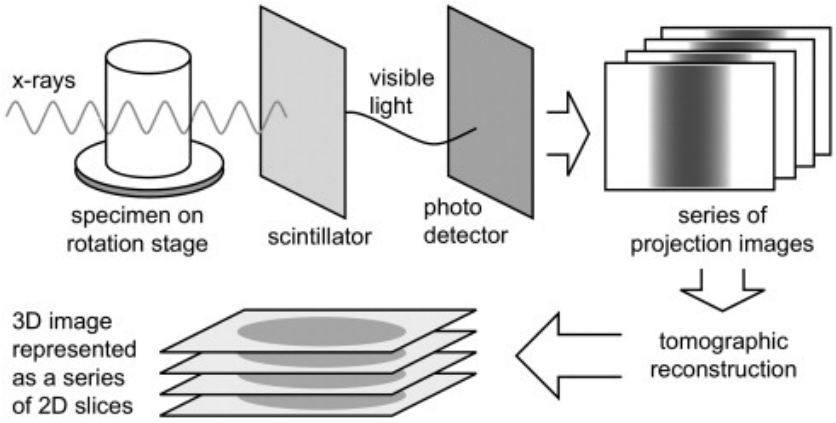

Figure 2.5: Schematic illustration of the micro-computed tomography technique [28].

This method allows to obtain faithful virtual representations of a material geometry at the microscale and retrieve properties information needed for studying TPS in the aerospace industry.

The concept of Representative Elementary Volume (REV) is essential in porous media and volume-averaged modelling approaches. It is defined as the absolute minimum domain volume which can provide a representative value for the characteristics of the whole material, and that is not affected by any small-scale heterogeneity of the porous medium [29]. As the materials employed in TPS have high porosity values, the measurements can vary if the sample size is too small because only one of the phases was measured or their proportions are locally different.

Figure 2.6 shows that as the volume increases, the fluctuations observed tend to stabilize to a specific value as soon as the REV is achieved. As the domain becomes larger, it will become more homogeneous until the properties become constant under a given threshold

(2 %) defined as the normalized standard deviation. The REV analysis should be done independently for each property, as some of them can converge towards the REV faster than the others, requiring different domain sizes as previous studies have shown, for example, that porosity converges more quickly than thermal conductivity.

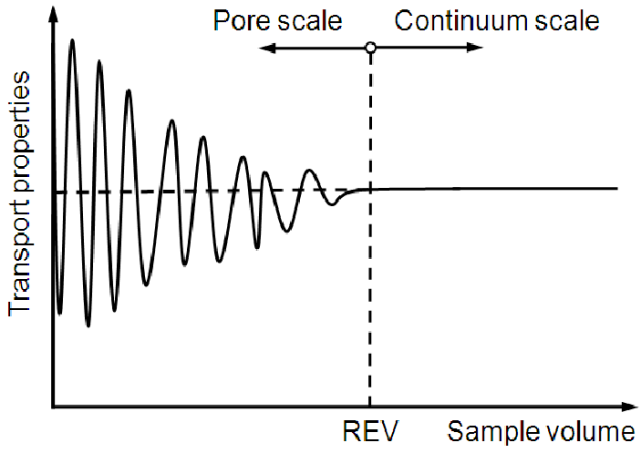

Figure 2.6: Representation of the definition of REV for a normalized property [30].

The REV analysis is not only important for numerical simulation, allowing the lowest computational resources possible, but also for experiments to guarantee that the property measured is representative of the overall material.

2.2.2 Fundamentals of heat transfer within porous media

From the study of thermodynamics, energy can be transferred by interactions of a system with its surroundings. Different heat transfer processes are referred to as modes: conduction, convection and radiation. In porous media, heat transfer occurs significantly due to conduction [31]. In solid insulating materials, the transport property that controls heat conduction is the thermal conductivity in the steady state, and the combination of thermal conductivity and specific heat capacity in transient situations [32], which depends on the thermal conductivity and surface radiation properties of the solid material as well as the nature and volumetric fraction of the void space [31].

Thermal energy transport may be due to two effects: the migration of free electrons and lattice vibrational waves. The lattice vibration quanta are phonons. In insulators, the phonon contribution is prevalent since electrons form covalent bonds which do not have much mobility. Therefore, the thermal conductivity of insulating material is determined by phonons' heat capacity, average velocity and mean free path [31]. Equation 2.6 for heat

conductivity from the kinetic theory reads

$$k = \frac{1}{3} C \bar{c} \overline{\lambda} \quad (2.6)$$

where C is the volumetric specific heat, $\bar{c}$ the mean velocity and $\overline{\lambda}$ the mean free path. It is possible to conclude that the mean free path has an influence on thermal conductivity. Materials with small size pore have lower conductivity because the mean distance between adjacent pores becomes shorter and phonon scattering is no longer effective [33]. Additionally, when pores are periodically arranged there is an easiness of phonon transport, increasing conductivity.

The mode conduction is described as the transfer of energy from the more energetic to the less energetic particles due to their interaction. To model the amount of energy being transferred in the heat transfer process, it is required to employ appropriate equations. For heat conduction, the heat flux equation is known as Fourier's law (equation 2.7) and is defined as the amount of heat that is transferred per unit of time and per unit area when it is exposed to a thermal gradient between two opposite sides of a material,

$$\vec{q} = -\underline{\underline{\kappa}} \nabla T \quad (2.7)$$

where $\vec{q}$ represents the heat flux ($\mathrm{W\,m^{-2}}$), k the thermal conductivity ($\mathrm{W\,m^{-1}\,K^{-1}}$) and ∇T is the thermal gradient (K). The minus signal in equation 2.7 is a consequence of the fact that heat is transferred in the direction of decreasing temperature.

Thermal conductivity in not a scalar, but rather a 3×3 symmetric tensor where the main diagonal represents the conductivity of the material in the three given axis as depicted in equation 2.8.

$$k_{ij} = \begin{pmatrix} k_{xx} & k_{xy} & k_{xz} \\ k_{yx} & k_{yy} & k_{yz} \\ k_{zx} & k_{zy} & ka_{zz} \end{pmatrix} \quad (2.8)$$

For an isotropic material, the thermal conductivity is a scalar. However, the material in the current study has a transverse isotropic behavior, meaning that in the principal axis of equation 2.8, their physical properties are symmetric about an axis (k_x=$k_y \neq k_z$).

Combining equation 2.7 with the conservation of energy, the general heat conduction

equation can be expressed as in equation 2.9

$$\frac{\partial T(\mathbf{r},t)}{\partial t} = \left(\alpha \underline{\underline{\kappa}} \nabla T)\right) \quad (2.9)$$

where k is the thermal diffusivity defined by equation 2.6. For isotropic materials, thermal diffusivity ($\mathrm{m}^2\,\mathrm{s}^{-1}$) measures the ability of a material to conduct thermal energy relatively to its ability to store thermal energy [31].

$$\alpha = \frac{k}{\rho c_p} \quad (2.10)$$

Effective thermal conductivity, k_{bulk}, is not an additive property. It varies with the medium's porosity, the intrinsic thermal conductivity of each phase, k_{int}, the geometry, pore structure and nanoscale phenomenons. Hence, k_{bulk} can be defined as function of these properties as $k_{bulk} = f\left(k_g, k_f, \varepsilon, \text{geometry}\right)$. In general, the thermal conductivity of fluids is lower than that of solids. Intermolecular spacing is much larger and the molecules' motion is more random for the fluid state than for the solid state leading to a less effective thermal energy transport [31].

Predicting the effective thermal conductivity can be difficult and requires detailed knowledge of the parameters of the porous material. Several numerical correlations have been developed for these composite materials, but sometimes they are not valid for the type of material in the study. Several experiments can extract thermal conductivity such as the Laser Flash Analysis (LFA) and the Guarded Hot Plate (GHP) [34]. An alternative approach to experimental techniques is to use simulation to compute effective thermal conductivity.

LFA is a non-contact transient thermal measurement method used for measuring the thermal diffusivity, α, with excellent repeatability at very high temperatures [35]. This method's operation measures the temperature variation on one side of a few millimetres material sample resulting from instantaneous heating applied to the other side. The pulse's energy is absorbed on the front surface and the resulting rear face temperature rise is recorded. Figure 2.7 represents the principle of the LFA technique. The thermal diffusivity of the material is obtained according to equation 2.11 from the resulting half-time of the temperature rise at the rear face measured with an infrared (IR) detector,

$$\alpha = 0.1388 \frac{d^2}{t_{1/2}} \quad (2.11)$$

where d is the thickness of the sample and $t_{1/2}$ the time required to achieve half of the maximum temperature rise [36]. Thereafter, thermal conductivity can be determined through equation 2.10, given heat capacity, c_p, and density, ρ.

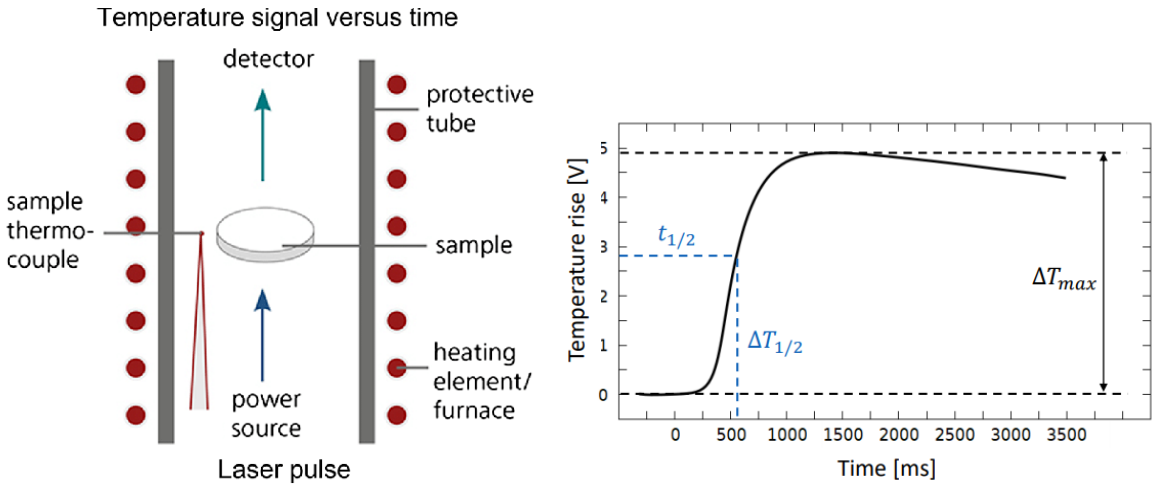

Figure 2.7: Principle of the LFA technique for thermal diffusivity measurements [37]

GHP is a steady state measurement method which determines experimentally the effective thermal conductivity, k, by using the electrical power output of a hot plate with guided heat conduction. An electrically heated plate heats the sample from one side embedded in a metal plate known as guard, which is heated to the same temperature as the plate. A cooling plate controls the temperature on the other side of the sample. The guard heaters minimize lateral heat transfer from the main metering area. Ideally, there should be no radial temperature differential in the metre section, such that all heat travels axially through the specimen section under the metre [38]. The schema of this technique is portrayed in Figure 2.8.

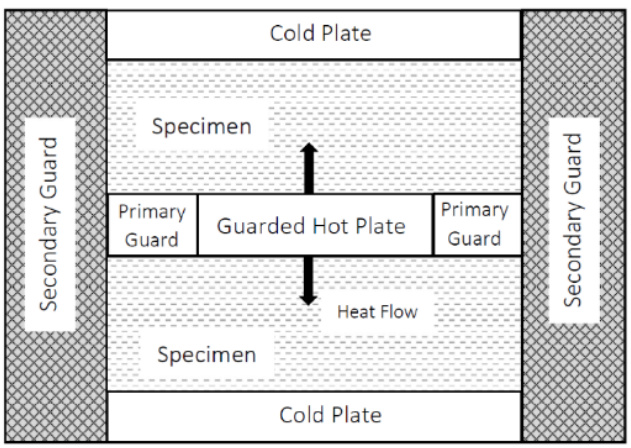

Figure 2.8: Illustration diagram of guarded hot plate method [39].

Radiative heat transfer

Even though heat transfer by radiation within the porous structure may be important at high temperatures, in this work we have focused only on the conductive component. Modelling the radiative transfer within the pores is challenging and it would involve substantial effort that is outside the scope of the current project.

Thermal radiation is emitted by all matter [31]. As an alternative to computing the effective thermal conductivity taking into account the radiative component, the Rosseland diffusion relation 2.12 can be implemented,

$$k_R = \frac{16\sigma T^3}{3\beta_R} \quad (2.12)$$

where σ is the Stefan-Boltzmann constant and β_R the extinction coefficient which can be defined as the sum of the absorption and scattering coefficient. This approximation is valid if the medium is optically thick and exhibits an isotropic scattering phase [40].

The extinction coefficient is not a local property and is dependent on the porosity and morphological structure of the material. There are different possibilities for the determination of this property. Tomography images, by means of scattering theory, are processed to retrieve the morphological properties required for its computation. Moreover, it can also be measured by Scanning Electron Microscope (SEM) [40].

2.3 Carbon/phenolic ablator: the ZURAM material

This section begins by providing a description of the study's material constituents and its manufacturing processes, a lightweight porous ablator known as ZURAM. Finally, it concludes by characterizing CALCARB CBCF 18-2000, the preform used in ZURAM material.

2.3.1 Material description and processing

As mentioned before, this work models ZURAM, a lightweight carbon/phenolic porous ablator developed for high enthalpy entry missions by the German Aerospace Center (DLR), featuring low densities of $0.36 - 0.4\,\mathrm{g\,cm^{-1}}$ and high porosity ($\varepsilon > 0.8$) [6]. It was designed for research purposes to understand the behaviour and underlying physics of ablative ma-

terials. It allows the scientific community access to a consistent set of material data and benefits it by exchanging results and model comparisons.

ZURAM is manufactured similarly to other lightweight carbon/phenolic ablators, such as PICA [5] and ASTERM. It consists of a rigid carbon preform impregnated with phenolic resin. The preform material is CALCARB CBCF 18-2000, a non-flexible carbon-fiber felt manufactured by Mersen Ltd [41, 42]. One other advantage of using this material is the possibility to evaluate the preform and the phenolic resin separately. For the present work, ZURAM 18/50 was used. The ZURAM manufacturing process consists of three steps: impregnating CALCARB with the phenolic resin, curing at $145°\mathrm{C}$ and tempering, followed by a drying process [18].

CALCARB CBCF 18–2000 is made of short carbon fibers product of the pyrolysis of rayon. These are arranged with a certain preferential plane, while on the other axis are distributed more randomly. Therefore, it is considered to have a transverse isotropic behaviour having properties in the In-Plane (IP) and Trough-Thickness (TT). It presents a bulk density of $180\,\mathrm{kg\,m^{-3}}$ and a nominal porosity of 0.89 [41]. The variation in density is reported as nonnegligible, affecting the final density of ZURAM. Therefore, a 0.02 variability in porosity must be taken into consideration to account for the $\pm 30\ \mathrm{kg\,m^{-3}}$ variation in the bulk density reported in the real material [6]. Table 2.1 shows the manufacturer's data for the bulk thermal conductivity of CALCARB® CBCF-2000 at different temperatures and mediums.

Table 2.1: Thermal conductivity ($\mathrm{W\,m^{-1}\,K^{-1}}$) of CALCARB CBCF 18-2000 at different temperatures and mediums (vacuum, argon, nitrogen).

	673 K	773 K	1073 K	1273 K	1473 K	1673 K	1873 K	2073 K	2273 K
Vacuum	0.25	0.26	0.35	0.41	0.48	–	0.69	–	1
Argon	0.33	0.36	0.45	0.54	0.63	0.74	0.86	0.99	1.16
Nitrogen	0.45	0.48	0.64	0.72	0.84	–	1.15	–	1.47

Due to the material's low porosity, the testing gas has a significant impact on the material's effective conductivity as depicted in in Table 2.1. The CALRCARB conductivity in a vacuum medium is the lowest, whereas the conductivity in nitrogen is the highest. This can be explained by the gas contribution to the effective conductivity since vacuum, argon and nitrogen are listed in increasing order of values for gas conductivity, as represented in Figure 2.9. Helium is added in Figure 2.9 since this is the testing gas employed in the LFA and GHP experiments referred to in Chapter 6.

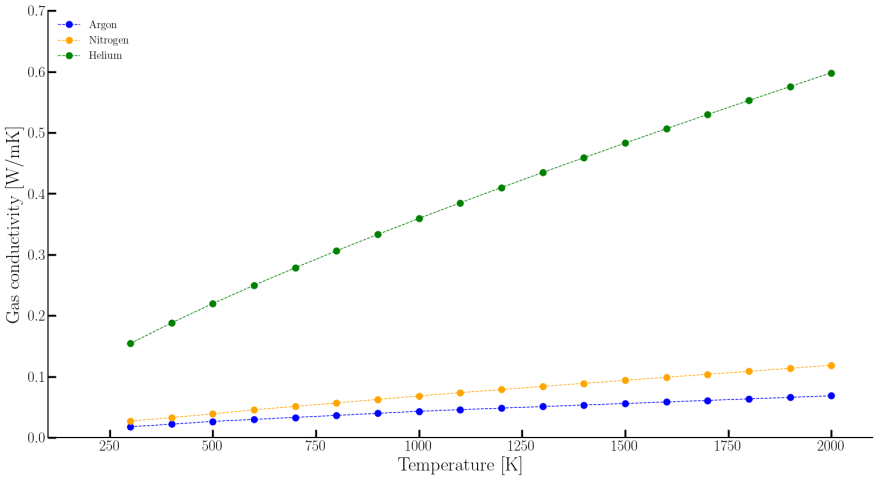

Figure 2.9: Thermal conductivities of three mediums: vacuum, argon and nitrogen as a function of temperature computed with Mutation++ [43].

In conclusion, for porous material, increasing the intrinsic conductivity of the medium leads to a rise in the bulk conductivity of the material. Additionally, Figure 2.10 demonstrates that effective conductivity is a function of temperature.

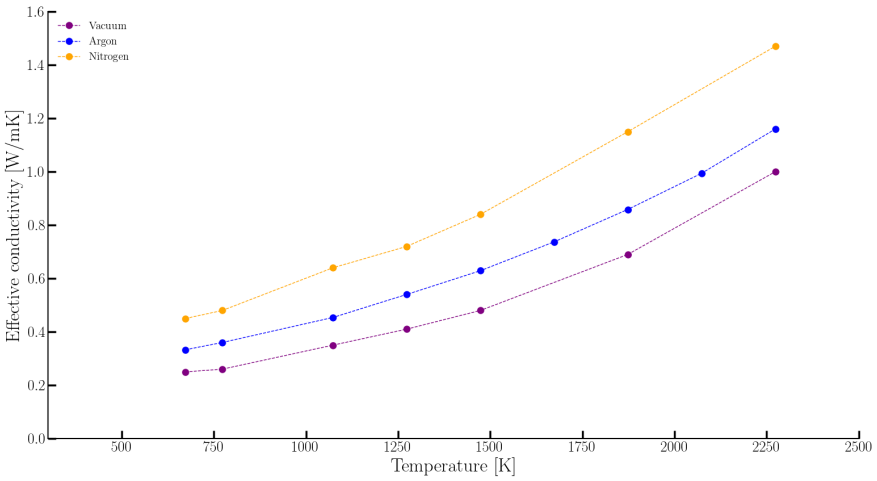

Figure 2.10: Thermal conductivities of CALCARB CBCF 18–2000 under different environments as a function of temperature from Mersen experimental data [41, 42].

2.3.2 Carbon fiber preform properties

Carbon fibers are typically made of 90 % in mass of carbon. Due to their properties at high temperature, such as wide range of Young modulus, thermal conductivity and coefficient of thermal expansion, carbon fibers are particularly attractive for aeronautics, aerospace and military applications [44]. Rayon fibers are the preferred option in the aerospace field for use in TPS due to their low thermal conductivity. To study the influence of the Heat

Treatment Temperature (HTT) on the thermal conductivity of rayon fibers, Figure 2.11 was plotted according to the measurements performed by Pradere [44]. It can be inferred that the thermal conductivity is influenced by the type of post temperature treatment employed.

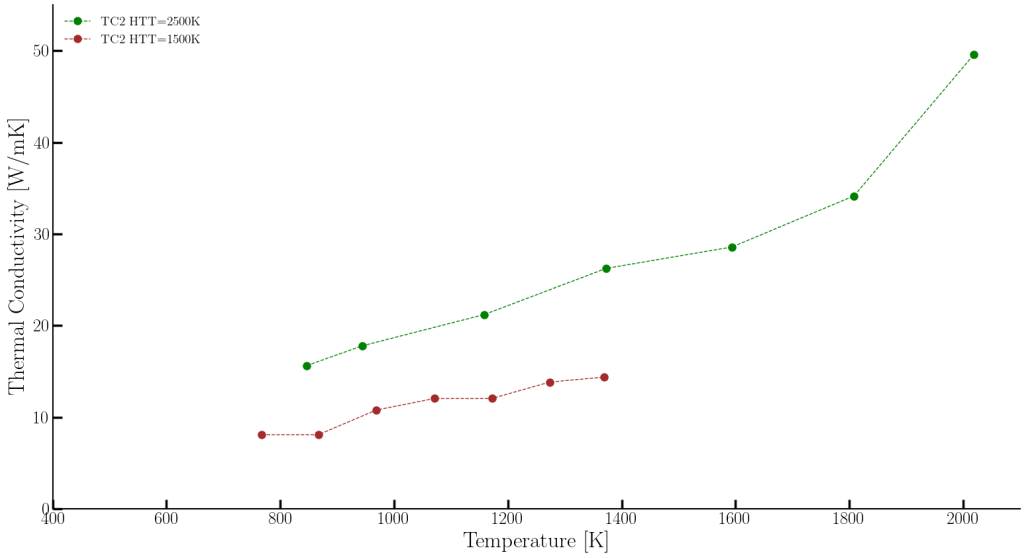

Figure 2.11: Thermal conductivity measurements of rayon-based (TC2) carbon fibers [44].

CALCARB uses rayon fibers as the material of the preform [6]. Even though the HTT of this material (2273 K) is slightly lower than the temperature used in the rayon-based fiber from Pradere (2500 K) [44], previous works have demonstrated that this difference does not vary the intrinsic conductivity of the fibers in this temperature range [18]. Therefore, by digitizing the provided data from the TC2 fibers, the temperature-dependent intrinsic conductivity of CALCARB fibers was determined.

2.4 Graphitization of carbon fibers

From Figure 2.11, it can be seen that the HTT has an important effect on the thermal conductivity of the fibers. TC2 fibers pre-treated at higher temperature (2500 K) present a higher conductivity which can be explained by graphitization. Carbon fibers can undergo this phenomenon, and it occurs when submitted to high temperatures at approximately around 2500 K to 3000 K [45]. To counteract this phenomenon, carbon fiber producers often pre-treat their materials at high temperatures. Recent experimental measurements of charred ZURAM material have also shown an increase in the effective thermal conduc-

tivity when the heating temperature exceeds the HTT [46].

The graphitization process can be described as the re-arrangement of the carbon atoms within the material into graphite-like structures, resulting in an enhancement of the thermal conductivity of the material. The magnitude of this process depends on temperature, pressure, nature, and structure of the material being graphitized [47]. This process enhances packing efficiency towards a hexagonal crystal structure, diminishing the interplanar distance and promoting a more uniform alignment of the structure. As a result, there is an increase in the crystallite size and density of the fibers and removal of lattice defects and grain boundaries [2]. In addition, modifications to the mechanical and chemical properties of the fibers have also been studied. For example, these materials have higher resistance to oxidation due to their reduced number of defects [47, 48].

For atmospheric entry applications this is particularly important since thermal conductivity is the main driver for heat transport [11]. The rise of in-depth temperature in the material can damage the spacecraft's structure, causing mission failure. Characterizing and understanding this phenomenon becomes essential.

The degree of graphitization can be determined experimentally by X-Ray Diffraction and Raman spectroscopy [2].

Chapter 3

Simulation tools for porous materials

When designing a TPS, it is critical to employ numerical techniques to predict material performance. As previously addressed in Section 1.2, adequate characterization of thermophysical properties allows reliable predictions which are used to optimize sizing and mass and, consequently, reduce safety factors, allowing for a higher payload fraction of the spacecraft. To do so, the first step is to understand the difference between macro and microscale modelling, as displayed in Figure 3.1, and why it is essential for this study.

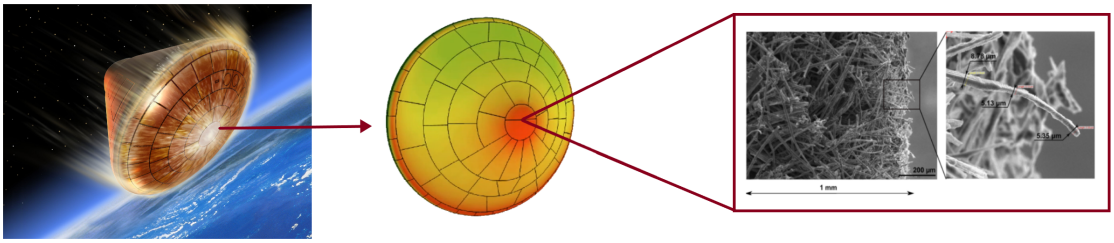

Figure 3.1: Macroscale and microscale modelling of thermal protection systems [49].

Macroscale modelling refers to the full-scale material response solver that typically uses volume-averaging techniques, while microscale modelling provides information about the material properties and response parameters applied in the full-scale model. When using composite or porous materials in research, the objective is to be able to simulate the complete system. This is not numerically possible since resolving the actual pore structure of the full material would be computationally too expensive. Therefore, averaging or homogenization techniques need to be adopted at the macroscale and for that, the effective material properties must be provided [13]. These properties can be computed with various methods. The first and most obvious is also the oldest one that researchers make use of, the measurement through experiments. Experimental work, as discussed in Section 1.2, can be very helpful but it can also be very expensive and have numerous limitations, such the range of conditions in which the experiments can be conducted. Moreover, more recently, modelling at the microscale has become commonly preferred, and what made this conceivable was the development of μCT, a very important tool in material science that allows non-destructive characterization of microstructures up to micron-level spa-

tial resolution [50, 51]. The final three-dimensional digital representation of the physical samples of a given material constitutes a high-fidelity image of what the material looks like at the microscale and a great framework to quantify the effective material properties used in macroscale material response models.

In the past few years, several research projects have developed and validated analytical and numerical models for studying the thermal and mechanical behaviour of thermal structures employed in reentry vehicles. This motivated the development of commercial software for microstructure analysis, such as GeoDict [52], Avizo XLab [53], and Simpleware [54], which compute thermal, mechanical, and morphological properties of material structures based on μCT. Academic software like TauFactor [55], iMorph [56] and TomoWrap2 [57] can also determine some physical properties. Even though some of them are open-source, they focus primarily on low-temperature applications, unable to accurately represent real aerospace applications.

For this reason, it was necessary to develop an open-source numerical tool that could simulate the high thermal gradients and chemistry conditions to which spacecraft are subjected, carried on by aerothermal reentry fluxes. Besides that, since it is an open source for research worldwide, it enables users to understand how the code functions and promotes innovation through collaboration, thus allowing rapid development in this field. Thereupon, the Porous Microstructure Analysis (PuMA) was developed with the initial goal of simulating the phenomena that occur when TPS are employed on heat shields based on microstructural data from μCT [13].

This chapter presents an overview of the PuMA software, such as the description of the architecture structure and its features, with a special emphasis on the computation of effective thermal conductivity. It concludes with a brief introduction of a surrogate model that will be used to allow the quantification of how the microstructure parameters influence the overall performance of real porous material.

3.1 Porous Microstructure Analysis Software

PuMA is a software developed at NASA Ames Research Center and is available as an open source under a US & Foreign release. It has been constantly updated since 2014, having a third version already released [13, 14].

PuMA can be defined as a collection of tools for the analysis of porous materials that are able to calculate, from a 3D sample material obtained from microtomography or artificially generated microstructures, effective material properties at the microscopic scale which can be used in macroscale models. It was first written in C^{++} for Linux operating systems and optimized for multi-processor workstations. The latest version introduces *pumapy*, a Python version of the PuMA software.

For a typical microscale simulation, the workflow is divided first into obtaining the microtomography samples, then going through the process of post-processing and segmentation of the data, performing the numerical simulation and finally integrating the bulk quantities. Numerical simulations can be carried out in diverse software. However, these involve meshing, imposing physical conditions on the numerical solver and post-processing the obtained quantities. This process is very time-consuming, and each step requires extensive competence and comprehension. Understanding how difficult this approach is, PuMA combines three aspects of the previous workflow (the meshing, the numerical solver and the integration of the retrieved properties) into one single step. As illustrated in Figure 3.2, the Puma workflow consists in obtaining the microtomography samples, post-processing and segmentation of the digitized images and running the PuMA simulation.

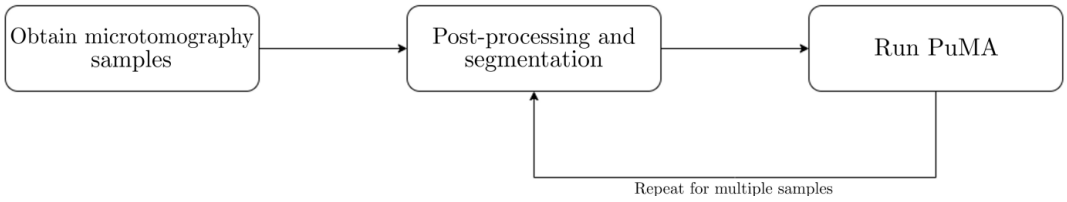

Figure 3.2: Visualization of PuMA's workflow.

Before going into more detail about PuMA's architecture, let us first understand the software's capabilities. It is a collection of solvers and tools for particular tasks, such as the determination of effective material properties and material response. Behind PuMA's solver, there is a set of unifying data structures, linear solvers and inputs and outputs tools that the user has access to, which allows further development of the code.

The user has three different ways of interfacing with the code, as shown in Figure 3.3. The first one to be released was the C^{++} version having full access to the PuMA Application Programming Interface (API). Besides this, there is the Graphical User Interface (GUI) that mostly calls the C^{++} code. Lastly, there is version 3.0 of the software that introduces

the python package *pumapy*, which contains almost all of the features of the previous version, with more advanced and extended capabilities.

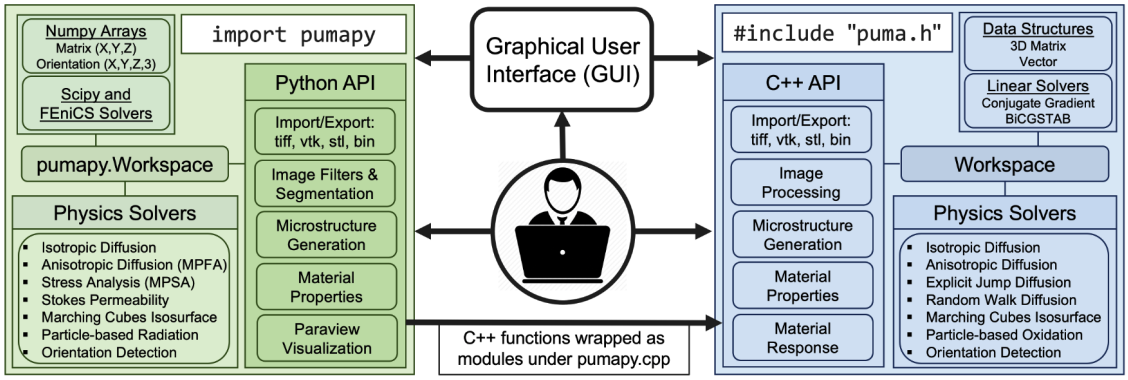

Figure 3.3: Schematic of PuMA's software architecture [14].

PuMA's architecture can be divided into three main modules: domain generation, material properties and material response. The latest is not included in version 3.0 of the software. This study primarily employs the functionalities of the Python version due to the fact that it was necessary to access and modify specific functions of the code and perform more complex tasks such as simulations of multi-phase materials. Before addressing the three main modules of PuMA it is important to understand how the software stores all the data of the microstructure being analyzed. This is achieved through a data structure called workspace that is made of small cubes, or voxels, holding a value on a uniform 3D Cartesian grid, as this is the typical format of microtomographic data.

3.1.1 Domain generation

Domain generation consists in generating the computational domain that can come from two different sources. The first is importing a microtomography image as a 3D Tag Image File Format (TIFF) stack, where the geometry of the fibers is captured as a 3D matrix of grayscale values, and the second is artificial generation of a material microstructure. Figure 3.4 and 3.5 represent both possibilities.

For the latest, given a set of specific macroscopic and microscopic parameters as an input to simulate the material to study, such as porosity, length, radius, angle distribution and domain size, the software is able to iteratively generate a geometry structure that converges towards the parameters previously established. Artificial models can also be stored as a TIFF image for further analysis. For both methods, the internal subdomain for each

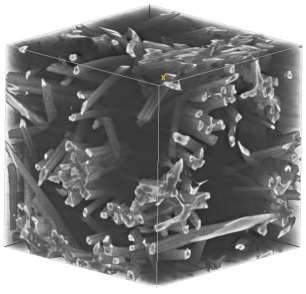

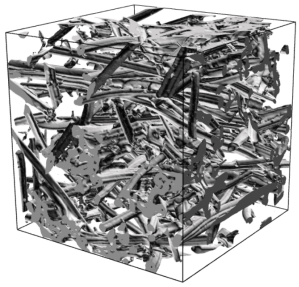

Figure 3.4: Micro-tmography image of a fibrous material and its representation in PuMA [58].

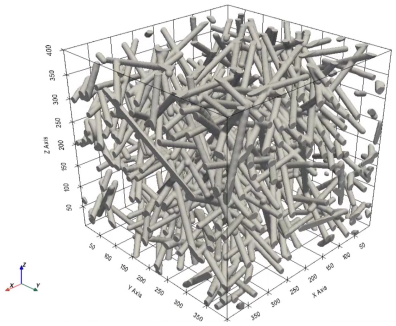

Figure 3.5: Random fibers artificially generated in PuMA.

material phase corresponds to an interval of grayscale values, and the voxel in microns serves as the unit of measurement.

PuMA allows to generate other geometries, such as boxes, spheres and cylinders and also random 3D fibers and spheres, packed spheres beds, periodic foams, triply periodic minimal surface and woven structures.

Since our study is focused on carbon fiber materials, artificial generation of random straight fibers was mainly used. This is done by randomly arranging cylinders that represent the fibers. The user can specify as inputs the domain size, the radius and length of the cylinders in voxels plus their variation, the material's porosity, the fiber angle variability and if it allows the intersection of the fibers, as depicted in Figure 3.6. This last parameter allows for a faster simulation response. It is also important to notice that the number of generated cylinders is a function of the porosity that the user inputs as a target value for the generated material. The code will iteratively create fibers until an approximate value for the porosity is reached.

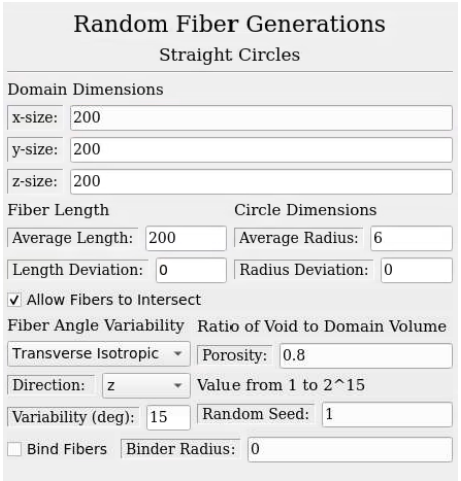

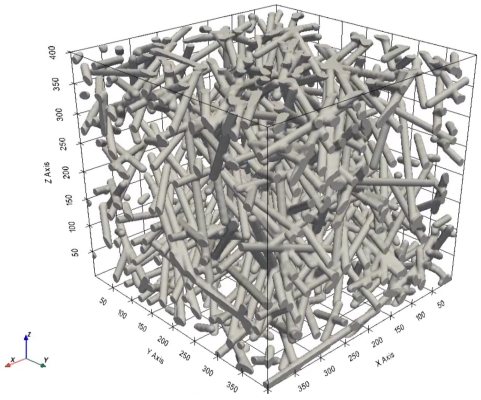

Figure 3.6: Inputs for random fiber generation and visualization output of the fibers phase on GUI.

The same inputs must be supplied for the python version. More details on how random fibers are generated will be stated in Section 4.2.

3.1.2 Effective material properties

The computation of morphological, thermal, transport and mechanical effective material properties is a prominent aspect of this software. It is possible to determine porosity, volume fractions, pore diameter, specific surface area, isotropic or anisotropic effective thermal and electrical conductivity, tortuosity, diffusivity, permeability and finally, elasticity. It should be emphasized once more, as in Section 2.2.1, that in order to correctly inform macroscale response simulations, these properties must be estimated at the scale of the REV.

In order to understand how PuMA computes these properties, a brief review of the most relevant physical properties of porous media for this work will be given in this section. The other physical properties are referenced in Appendix A. Previous investigations have revealed that the effective thermal conductivity of the carbon/phenolic ablators is one of the major drivers of the in-depth heat transfer [59]. Hence, this thermal property is the main focus of this project, and its computation will be described in more detail in Section 3.2.

Porosity and volume fraction

As previously addressed in Section 2.2.1, properties of composite materials are a combination of different phases. For the purpose of this study, carbon/phenolic ablators are porous materials, with the solid phase being represented by the fibers, while the void is represented by the surrounding gas and each phase occupies a certain volume fraction.

PuMA determines porosity and volume fractions based on a thresholding segmentation method. Therefore, the volume fraction of a specific phase can be expressed by $\Phi_{\mathrm{i}} = \frac{N_f}{N_{tot}}$ and it is defined as the ratio of the number of voxels of that phase, N_f, to the total number of voxels in the domain, N_{tot} . Porosity is defined as the volume fraction of the void phase, $\Phi_{\mathrm{void}} = \varepsilon = 1 - \frac{N_f}{N_{tot}}$, and its computation is an iterative process.

Specific surface area

First it is necessary to differentiate between Surface Area (SA) and Specific Surface Area

(SSA). The former, for fibrous materials, is defined as the sum of the area of all the fibers in the domain expressed in m^2, whilst the latter is defined as the ratio between the surface area and the complete volume of the sample and it is expressed in m^{-1}[60].

There are several approaches to the 3D surface generation problem [61]. To compute surface area, PuMA includes two of them, the voxel approach and the iso-surface based approximation. The voxel-based method, also denominated as the Cuberille Grid, involves summing each voxel's exposed solid face area to identify the total surface area and has an error of approximately 50% [13]. To improve this, an iso-surface approximation is used with a Marching Cube or a Marching Tetrahedra algorithm [61, 62], where the total area of the fibers' surface is calculated as the sum of each individual triangle area in the computed triangulation. The specific surface area can be defined in equation 3.1

$$SSA = \frac{\frac{1}{2} l_{\mathrm{v}}^2 \sum_{\mathrm{i}} |\vec{u}_{\mathrm{i}} \times \vec{v}_{\mathrm{i}}|}{V} \quad (3.1)$$

where $\vec{u}_{\mathrm{i}}$ and $\vec{v}_{\mathrm{i}}$ are the vectors defining each triangle i, and l_{v} is the voxel length.

In order to better understand how the algorithm functions, a quick overview will be given. The Marching Cube algorithm, developed by Lorensen and Cline [61], incorporates a discrete cube division of the input volume to generate triangular models of constant density surface. By performing linear interpolation on the collected data at each corner, surface intersection points are identified along the cube's edges, and the vertices are then connected. By iterating this cube over the data and generating surface patches whenever the cube intersects the surface, the whole iso-surface can be triangulated [62]. Considering the fact that each of the vertices may or may not be part of the geometry, it is possible to have 256 different cases. By symmetry, these can be reduced into 15, as illustrated in Figure 3.7.

However, this technique produces triangulations with numerous triangles having a low aspect ratio and does not ensure that the surface is topologically compatible with the data. Consequently, the Marching Tetrahedra algorithm avoids these problems, generating a higher number of triangles [62]. Even though, it should be noted that the solution will be a function of the resolution of the sample, depending on the precision of the measurements.

Material orientation estimation

The employment of TPS materials in atmospheric entry, which motivates the present

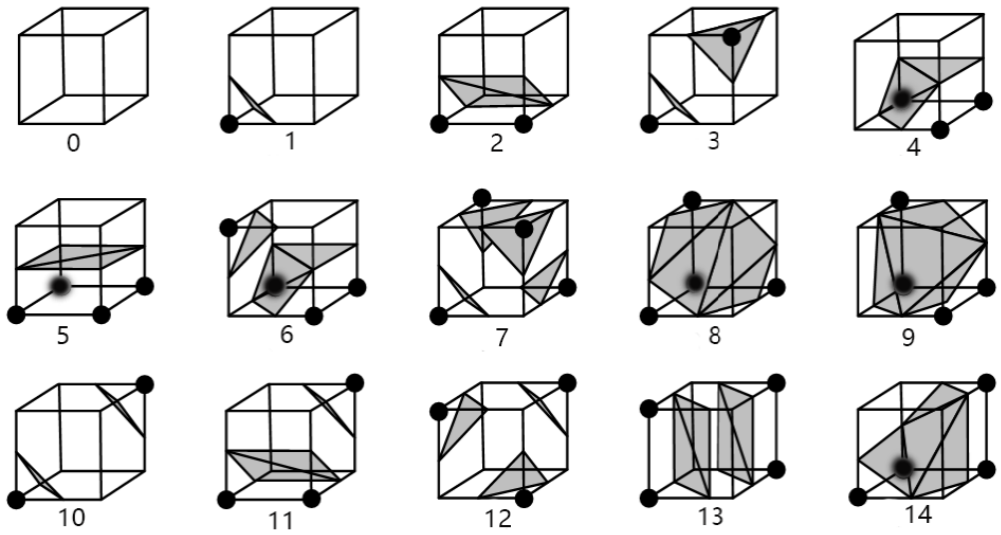

Figure 3.7: The 15 different configurations of Marching Cube algorithm [63].

study, requires knowledge of the local material orientation to properly address accurate modelling of the properties of such materials.

PuMA has three methods for estimating the material orientation of these microstructures [64] and in each technique, the first step is to identify the fibers using a grayscale cut-off. The structure tensor method is based on the eigenvector corresponding to the lowest eigenvalue discovered from the grayscale gradients. With temperature gradients imposed in all three directions, the artificial based technique calculates the orientation as the local steady-state flow vector in a heat transfer simulation. At last, in the raycasting approach, rays are generated at each solid voxel's centre and propagate until they first run into a material barrier and based on the distance that these rays travel, the local direction vector is computed.

Anisotropic conductivity and elasticity

In the new version of PuMA, it is possible to analyse the properties of anisotropic materials, such as their thermal conductivity and elasticity. Even though constituents of a material at the microscale are isotropic, at the mesoscale they can have effective properties that are anisotropic [14].

It is important to mention that anisotropy can be characterized at both bulk and local scales. As a consequence, a material can have locally isotropic components and at the same time a bulk anisotropic conductivity and vice-versa [65]. To account for anisotropy in a cartesian coordinate system, the local thermal conductivity tensor has to be consid-

ered as follow in equation 3.2.

$$\underline{\underline{k}} = \begin{bmatrix} k^{xx} & k^{xy} & k^{xz} \\ k^{yx} & k^{yy} & k^{yz} \\ k^{zx} & k^{zy} & k^{zz} \end{bmatrix} \quad (3.2)$$

The heat transfer with anisotropic local conductivity at steady-state and expanded to emphasize the impact of heterogeneity and anisotropy can be expressed as in equation 3.3.

$$\nabla \cdot \boldsymbol{q} = 0 \text{ where } \boldsymbol{q} = -\underline{\underline{k}} \cdot \nabla T = - \begin{bmatrix} k^{xx} & k^{xy} & k^{xz} \\ k^{xy} & k^{yy} & k^{yz} \\ k^{xz} & k^{yz} & k^{zz} \end{bmatrix} \begin{bmatrix} \partial T/\partial x \\ \partial T/\partial y \\ \partial T/\partial z \end{bmatrix} \quad (3.3)$$

After detecting the material's local orientation, a tensor rotation is required to convert the user-defined property tensor from the fiber aligned coordinate system to the global one, which is already implemented in the numerical solver in PuMA. The solver for the conductivity utilizes the Multi-Point Flux Approximation (MPFA)-O approach [66], since it can conserve the nature of the physical laws and the inherent discontinuity of the considered domain. An initial guess of the temperature is given and then in a conjugate gradient solver to achieve convergence. The final step involves determining the effective thermal conductivity. Once steady-state convergence is achieved, homogenization is accomplished by multiplying the converged flux by the total domain length for each direction as demonstrated in equations 3.4, 3.5 and 3.6.

$$k^{xx} = q^x \cdot L_x \quad k^{xy} = q^y \cdot L_x \quad k^{xz} = q^z \cdot L_x \quad (3.4)$$

$$k^{yy} = q^y \cdot L_y \quad k^{yz} = q^z \cdot L_y \quad (3.5)$$

$$k^{zz} = q^z \cdot L_z \quad (3.6)$$

The final effective conductivity tensor, $\underline{\underline{k}}_{eff}$, is derived by combining the results of the three simulations. Radiation at very high temperatures becomes important. Therefore, a ray-tracing method was added to estimate the optical radiative extinction coefficient, but this module is currently under development.

The computation of elasticity relies on a similar numerical model as the anisotropic conductivity and is solved in PuMA through a linear static solver and a finite volume approach based on Multi-Point Stress Approximation (MPSA)-W, where the divergence of the stresses at the steady-state, equation 3.7, is solved [14]. This method enforces the continuity of the stress and displacements in the boundary points.

$$\nabla \cdot \boldsymbol{\sigma} = \nabla \cdot (\boldsymbol{C}\varepsilon) = 0 \quad (3.7)$$

An initial guess of the unit displacement is given, and then an iterative solver yield converged stresses, from which it is possible to take the effective homogenized property. This approach enables the calculation of the elasticity tensor, the stress and the deformation field.

3.1.3 Limitations

PuMA is an open-source code and every external improvement is essential for the constant enhancement of the numerical simulator to have the highest fidelity tool to reproduce and predict the phenomenons and behaviour of ablative heat shield materials. The atmospheric entry involves a diverse set of phenomena, making the development of this tool a challenge. This leads to the introduction of assumptions into the models to simplify those phenomena. Even though the accuracy of these assumptions in assessing the material's efficiency are investigated, this can result in an inherent error in the property value.

This software is dependent on some parameters, such as geometry, fibers orientation, radius, length, porosity and the intrinsic properties of both gas and fibers and can be treated as a stochastic solver due to the random distributions given to some of those. Therefore, from the uncertainties of the parameters, the final value of the material property can vary. Even though accounting for the variability of the parameters of the material, such as the radius, length of the fibers and porosity, might lead to an underestimation of these values. Besides that, with the use of the artificial generator for the fibers, it is impossible to reproduce the exact material's physical structure since they are generated, taking into account that they are straight cylinders. Nonetheless, this is only an approximation of the actual geometry of the fibers. Also, the bundles of fibers that are possible to observe in a SEM image of CALCARB (Figure 4.1) are not represented in the generation, which could lead

to an error when computing, for example, the thermal conductivity [58].

Another limitation is that it does not consider the heat transfer by radiation between fibers at high temperatures, which should not be neglected. This has a significant impact at temperatures higher than approximately $2000\ ^\circ$C.

Computationally it is very expensive, taking a lot of time to run the necessary simulations. Additionally, the required processing power for very big domains is not always feasible, restricting the quality of the simulation since the samples may not be large enough to be representative.

3.2 Quantity of interest: thermal conductivity

To accurately compute the effective thermal conductivity of a material to be used on a macroscale model, it is essential to understand: 1) the dominant mode of heat transfer; 2) the constituent's parts; 3) if the material has an isotropic or anisotropic behaviour and 4) its microstructure. At very high temperatures, radiative heat transfer should not be neclected but for this study only the conductive component was included. However, the development team at NASA Ames and von Karman Institute for Fluid Dynamics (VKI) are interested in this topic and it should be addressed in future works. Besides that, it should also be guaranteed that the sample size used for the microstructure is sufficiently homogeneous at that scale through the REV analyses described in Section 2.2.1. The effective thermal conductivity is dependent on the material microstructure and the conductivity of its constituents [13].

The steady-state heat conduction equation is presented in equation 3.8,

$$\nabla \cdot (k \nabla T) = 0 \quad (3.8)$$

where k is the local thermal conductivity and T is the local temperature. In PuMA, it can be solved using three different approaches: a Finite Difference (FD) method, the Explicit-Jump Finite Difference (EJFD) method or the Random Walk method [13].

Both finite difference methods solve thermal conductivity by imposing a normalized temperature gradient across the domain. After, the steady-state temperature field at every

point in the 3 dimensional space is determined. Afterwards, the steady-state heat flux can be retrieved and used to compute the material's effective conductivity. Both finite difference methods should provide equivalent results [12].

The FD method utilises Dirichlet boundary conditions in the simulation direction. In contrast, the side direction employs periodic or reflective boundary conditions. The EJFD method uses periodic boundary conditions in all directions and is considerably faster. This method might not be appropriate for every material. However, since in our case the material is artificially generated, the structure itself is periodic and so it is suitable. This solver was specially implemented for the bulk thermal conductivity of a composite material [67]. It is highly automated and efficient, and the steady-state temperature field at every point is solved using Fast Fourier Transform (FFT), and the Bi-Conjugate Gradient Stabilized method (BiCGSTAB) [68]. It is stable and converges provided that the time step is smaller than half of the space step squared $\delta T^2 \leq \delta x^2/2$. For the conducted work, thermal conductivity computations were done by means of the EJFD method.

3.2.1 Simulation inputs and outputs

As addressed in Section 3.1.1, it is necessary to generate the computational domain before conducting the thermal simulation. Therefore, the user must input the parameters to specify the geometry. For the thermal conductivity simulations, it is also required to input the intrinsic conductivity of the constituent parts of the material. PuMA does not define temperature as a variable, hence the input parameters must be selected to represent it. This is accomplished by setting proper values for the intrinsic conductivities at the corresponding temperature. The accuracy of the iterative solver and the maximum number of iterations to be used are likewise inputs. For accuracy, the typical value is 10^{-4} and determines the threshold after which the residual becomes small enough to be considered a steady-state solution. The number of iterations is 10000 by default. These two values remain constant in the forthcoming simulations. The effective thermal conductivity in PuMA can be computed in the user's chosen direction.

3.3 Surrogate modelling

Optimization challenges often include executing a computationally intensive engineering function thousands of times with varying input parameters. Surrogate models are used to simulate the behaviour of a costly engineering model without the slow, expensive computing effort, reducing optimization time and costs. These models may also be used to simulate the behaviour of experimental data with a small sample size [69]. A surrogate model's role is to approximate the relationship between the input and output of a complicated function by generating a relationship between a group of inputs and outputs.

This section presents the Kriging model, which will be employed in Section 4.1.3 to simulate the model's behaviour. It was initially developed for geostatistics applications and built on the work of Krige [70]. Over the years it has seen widespread use due to being preferred for most generic applications and engineering problems. The suitability of a surrogate to a specific engineering issue is determined by the data set noise, number of samples, number of variables, and linearity of the problem.

It consists of an interpolating model that is a linear combination of a known function $f_i(\mathbf{x})$, which is added to a realization of a stochastic process $Z(\mathbf{x})$ as presented in equation 3.9.

$$\hat{y} = \sum_{i=1}^{k} \beta_i f_i(\mathbf{x}) + Z(\mathbf{x}) \quad (3.9)$$

For a mean zero and spatial covariance function $Z(\mathbf{x})$, a realization of a stochastic process, is given by equation 3.10

$$\operatorname{cov}\left[Z\left(\mathbf{x}^{(i)}\right), Z\left(\mathbf{x}^{(j)}\right)\right] = \sigma^2 R\left(\mathbf{x}^{(i)}, \mathbf{x}^{(j)}\right) \quad (3.10)$$

where σ^2 is the process variance, and R is the correlation.

Chapter 4

Software development and analysis

4.1 Preliminary study

The primary goal of this section is to understand the effect of microscopic properties of porous ablative materials on their macroscopic model evaluation. For the purpose of this study, the effective thermal conductivity is the quantity of interest and is a function of the porosity, the geometry and the intrinsic conductivity of the fibers and the medium, as aforementioned in Section 1.2.

Prediction of this effective property of a porous ablative material can be difficult and requires a detailed evaluation. Therefore, the developed parametric study was performed to evaluate the influence of some microscopic variables on the effective thermal conductivity and up to which extent. In order to better understand the effect of the different components and geometrical features of the material, an artificial synthetic model based on the carbon fiber felt of CALCARB CBCF 18-2000 was developed using PuMA derived from the data available in the literature. A REV analysis was also conducted on the synthetic model in helium and argon to verify that the domain size chosen for the experiments in Chapter 5 is representative of the bulk material and appropriate for properly representing the overall material's properties of interest.

Lastly, a sensitivity analysis based on a surrogate model was carried out, aiming to quantify how the effective thermal conductivity depends on the selected simulation inputs mentioned in Section 3.2.1.

4.1.1 Synthetic material model

To artificially generate materials in PuMA, a set of microscopic characteristics must be established in order to replicate the geometric sample of the material in the study. Since our material of interest is CALCARB CBCF 18-2000, the data gathered for this material

was based on the available literature, microscopic imaging data from Micro-Computed Tomography (μCT) and Scanning Electron Microscopy (SEM) [71, 2]. From the two SEM pictures of the virgin material, displayed in Figure 4.1, it is possible to observe bundles of combined fibers dispersed throughout the material and single fibers randomly distributed.

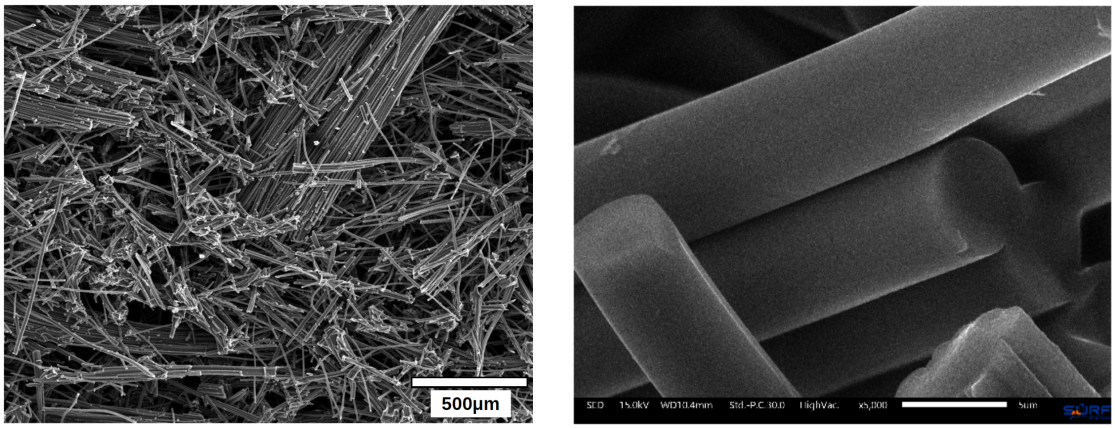

Figure 4.1: Virgin CALCARB CBCF 18-2000 SEM pictures taken at different scales [71, 2].

Helber [71] measured by SEM an average length of l_f=550 μm and diameter of d_f=6.5 μm for a single fiber. A value of 3 μm was chosen for the radius of a fiber since it is the needed input rather than the diameter, and it should be an integer voxel number. For each of these properties, a ± 30 % variation needs to be taken into account, considering the variability of the material model. It should be noted that 1 μm corresponds to 1 vx. CALCARB CBCF 18-2000 has a nominal initial density of about $180\,\mathrm{kg\,m^{-3}}$ and a nominal porosity of 0.89. A 0.02 variability in porosity ($\varepsilon = 0.89 \pm 0.02$) must be taken into consideration to account for the variation in the bulk density reported in the real material ($180\,\mathrm{kg\,m^{-3}} \pm 30\,\mathrm{kg\,m^{-3}}$) [6]. Bear in mind that this is a transversely isotropic material, a uniform distribution of fibers in the in-plane was set $\mathcal{U}(0,\ 360)$, whereas in the through-plane a normal distribution $\mathcal{N}(0, \sigma_f)$ was established, where σ_f represents the standard deviation of the angle between the IP plane and the fibers. ImageJ software [72] was applied to assess the angular variation of the fiber orientation out of the x-y plane, having a standard deviation of 30° and 0° mean.

Representative Elementary Volume

The synthetic model's validity is evaluated concerning the REV analysis to guarantee that the restricted domain size of the artificially generated sample is representative of the material, as already stated in Section 2.2.1. This is a significant feature, not only for numeri-

cal simulations but also for experiments. Moreover, the minimal representative size was attempted to be reached to minimise computational resources.

The REV analysis is a way to determine at what domain size for any given characteristic of the material it is reasonable to assume that the measured property is representative of the overall material. Hence, it should be done independently for each property, as some of them can converge towards the REV faster than the others, requiring different domain sizes. Previous studies have shown that porosity, specific surface area (SSA) and volume fraction converge quickly, while thermal conductivity requires much larger volumes to achieve convergence. On that account, a REV analysis for the thermal conductivity was carried out in *pumapy* with the material model developed in Section 4.2.

As it will be later seen, experiments and simulations were conducted in an argon and helium environment. Consequently, in both REV analyses were necessary. These analyses were also executed with the purpose of better understanding how REV varies as a function of the temperature and the medium. In order to save computational resources, only two different temperatures were chosen. For both media, the lowest temperature was established to be $846.54\,\mathrm{K}$, and the maximum temperature to be $1807.95\,\mathrm{K}$. This choice was based on the temperature range of the data available for the intrinsic thermal conductivity of the fibers pre-heated at HTT = $2500\,\mathrm{K}$ from Pradere [44]. The maximum temperature from the data was not used due to the possibility of graphitization.

It should be underlined that the previously described synthetic model was employed in all of these analyses. For the intrinsic conductivity of the fiber and the medium, a value was imposed at the corresponding temperature of the simulation. The intrinsic conductivity of the fibers was computed from [44] as showcased in Figure 2.11, while the conductivity of both mediums, argon and helium, was determined using Mutation++ [43].

To conduct the analyses, the first step is to define the domain sizes that will be created. Taking into consideration that the selected domains should be powers of two to minimise the prime factor for faster calculations, the numbers 64, 128, 256, and 384 were selected. The effective thermal conductivity was then computed for each domain size, medium, and temperature. To be able to calculate the normalised steady deviation to assess if the estimated REV values converge below $2\,\%$ (REV criterion) in each domain, the simulations were repeated five times. The convergence for the solver of the heat equation was set to 10^{-4}. Then, the values computed are extrapolated based on a power law to have an ap-

proximated representative elementary volume. The obtained results are shown in Figures 4.2 and 4.3.

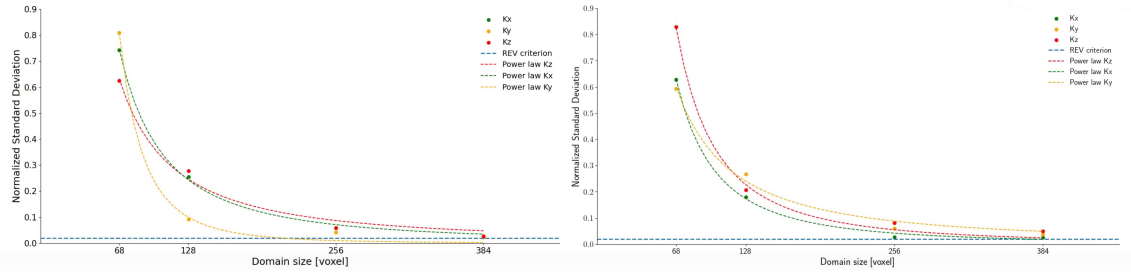

(a) T=846.54 K. (b) T=1807.95 K.

Figure 4.2: Representative Elementary Volume analysis in an argon environment.

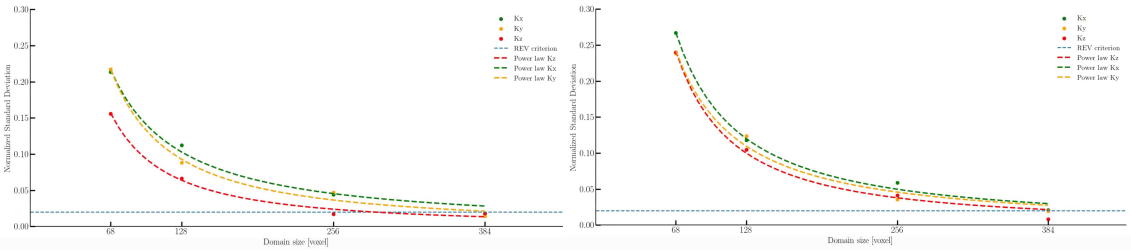

(a) T=846.54 K. (b) T=1807.95 K.

Figure 4.3: Representative Elementary Volume analysis in a helium environment.

It was decided to plot the conductivity in each direction, x, y and z, to demonstrate that at a representative volume, the x and y conductivity in a transversely isotropic material will perform similarly so that they can be averaged. It is also interesting to see that the most critical direction is the in-plane one. Based on the results of the analyses, it is possible to infer that the increase in the intrinsic medium conductivity has a positive effect on the reduction of the REV. However, it is also noticed that increasing the temperature, which can be translated into a higher intrinsic conductivity of the fibers, has the opposite effect on the REV values. For a constant gas, the ratio between the medium and fiber conductivity decreases with the increase in temperature. It is possible to deduce that when the ratio tends to a value closer to 1, the REV converges faster since the domain becomes more homogeneous. Hence, the properties become constant under a given threshold, $2\,\%$, not requiring larger domains.

For the argon environment, owing to the restricted computational resources, 600^3 vx was the largest domain size feasible to be generated, whereas, for the helium environment, a domain size of 410^3 vx was selected. Both were chosen with the purpose of optimising the time required for the computations. Figures 4.4 and 4.5 depict, respectively, the artificial generation of the synthetic material model in argon and helium.

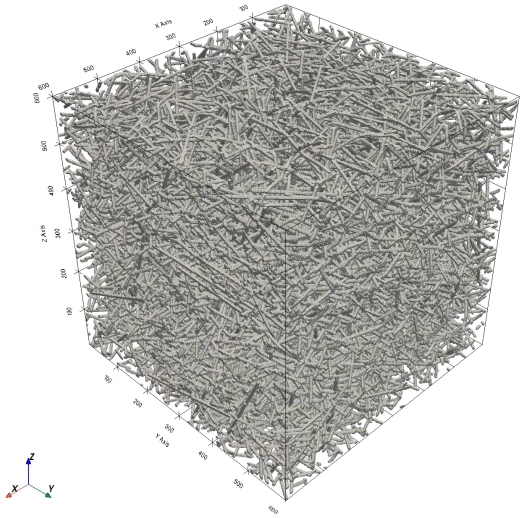

Figure 4.4: Artificially-generated model, representing the CALCARB material using straight solid cylinders in an argon environment

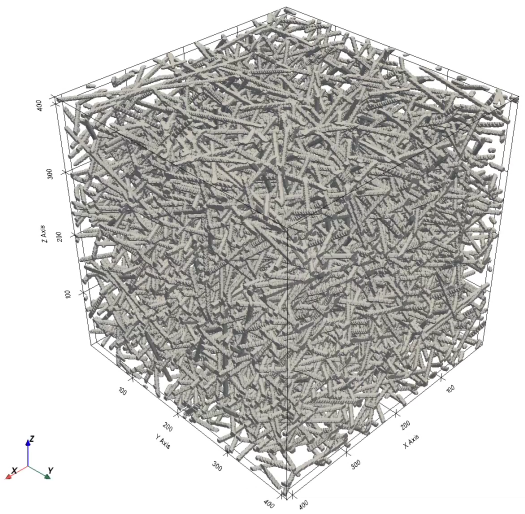

Figure 4.5: Artificially-generated model, representing the CALCARB material using straight solid cylinders in a helium environment.

4.1.2 Study of the microstructure effects on the thermal conductivity

The main objective of this parametric study was to get acquainted with the software and porous materials. It was also intended to evaluate the impact of microscopical parameters on thermal conductivity. It must be mentioned that for these analyses, only the GUI of the software was used since it was at the very initial phase of this work. Also, it should be noted that for this, the possibility to generate a transverse isotropic material with a normal distribution in the TT and a uniform distribution in the IP was already implemented. The initial generator had a uniform distribution in both directions.

It is important to understand how an aspect, such as the variation in geometry, can affect the response of carbon-phenolic ablators when exposed to high temperatures. In Section 1.2 it was already shown that, in fact, fiber distribution matters for the computation of thermal conductivity. Consequently, it is of foremost importance to understand which parameter is the most critical one in order for it to be more carefully characterized.

Different geometries were generated by varying parameters of interest, such as porosity, the angular variation of the fiber orientation out of the $x - y$ plane, fiber´s length, l, and diameter, D. The other properties of the material remain the same as previously described in Section 4.1.1 for the artificial generation for CALCARB CBCF 18-2000. All simulations were conducted in an argon environment at a temperature of $1000\,\mathrm{K}$ with an intrinsic conductivity of $0.0431\,\mathrm{W\,m^{-1}\,K^{-1}}$ obtained with the Mutation++ library [43]. The constant

intrinsic conductivity for the fibers was set to be $12\,\mathrm{W\,m^{-1}\,K^{-1}}$ and the accuracy for the solver of the heat equation was inputted as 10^{-4}. A voxel was defined as $1\,\mu\mathrm{m}^3$.

First the influence of the porosity and fiber's orientation was studied. A set of five values for each parameter was established. Typical values of porosity for carbon fiber preforms range between 0.85 to 0.92 [73] and for the orientation of the fibers between $15°$ to $35°$. From the obtained thermal conductivity simulation matrix, the values of main interest are in the diagonal representing the conductivity of the material in the three directions (x, y, z). The conductivity in the $x-y$ direction, K_{xy} and in the z direction, K_z correspond, respectively, to the IP plane and the TT plane conductivities. The former was obtained by averaging the values of the x and y directions, while the latter was represented only by the z direction. Figure 4.6 shows the results of the simulations performed in both directions.

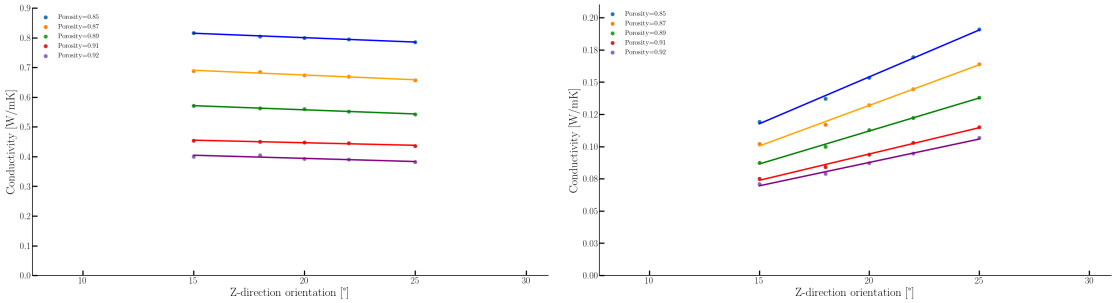

(a) In-Plane conductivity.

(b) Through-Thickness conductivity.

Figure 4.6: Influence of porosity and fibers' orientation in z direction on the effective thermal conductivity. Case for porosity = [0.85, 0.86, 0.89, 0.91, 0.92] and orientation (°) = [15, 18, 20, 22, 25].

It can be perceived that the IP plane's effective thermal conductivity (Figure 4.6a) is more affected by porosity than by the angular variation of the fibers. However, the contrary is observed in the TT plane effective thermal conductivity (Figure 4.6b). In both analyses, increasing the porosity decreases the effective thermal conductivity. This is explained by the reduction of the number of fibers in the domain and the low conductivity of the medium. The IP direction is less sensitive to the angle variation. As large number of fibers are in the IP plane, $68.24\,\%$ of them have an inclination in the range of $[-\sigma_f, \sigma_f]$, as seen in Figure 4.18, these will have a higher projection in the IP axis than in the TT axis. The angle variation is measured between the IP plane and the fibers, so the projections in the IP and TT direction are, respectively, with the cosine and the sine of the fiber's angle, σ_f. Additionally, it can be seen that a reduction of the influence on the angle variation of the fibers is obtained while increasing the porosity.

The second study was to investigate the impact of fiber length and orientation. The five

values used before for the orientation of the fibers in the z direction remain the same. The five values chosen for the length are $50\,\mu m$, $100\,\mu m$, $200\,\mu m$, $400\,\mu m$ and $600\,\mu m$.

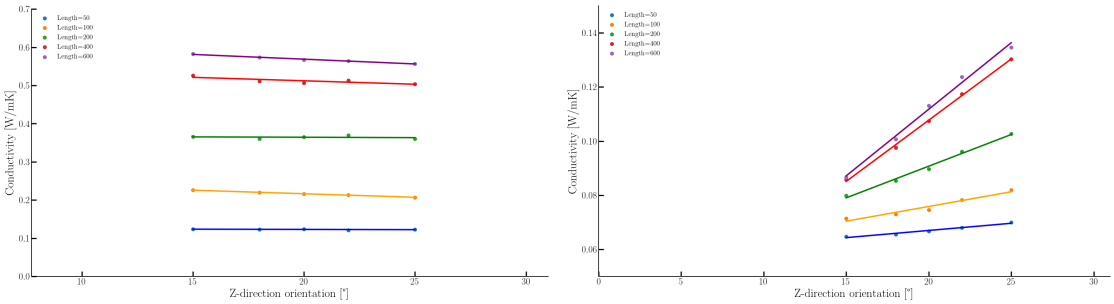

(a) In-Plane conductivity.

(b) Through-Thickness conductivity.

Figure 4.7: Influence of length and fibers' orientation in z direction on the effective thermal conductivity. Case for length (μm) = [50, 100, 200, 400, 600] and orientation (°) = [15, 18, 20, 22, 25].

As it can be seen in Figure 4.7, in both IP and TT planes, increasing the length results in an increase in the effective thermal conductivity. Increasing the length leads to a higher possibility of intersection between fibers. This means that the heat transferred is expected to rise and consequently, the thermal conductivity.

Lastly, it was decided to focus on the influence of the fiber radius and orientation. The analysis was conducted with the same values for the angle variation and for the radius $4\,\mu m$, $5\,\mu m$, $6\,\mu m$, $7\,\mu m$ and $8\,\mu m$ were the settled values.

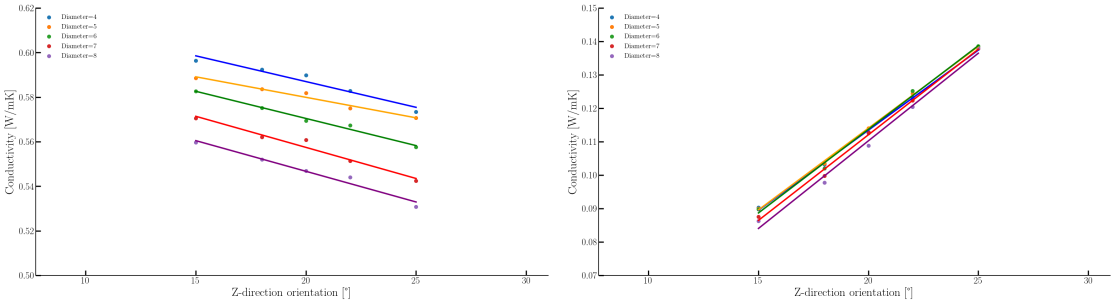

(a) In-Plane conductivity.

(b) Through-Thickness conductivity.

Figure 4.8: Influence of radius and fibers' orientation in z direction on the effective thermal conductivity. Case for radius (μm) = [4, 5, 6, 7, 8] and orientation (°) = [15, 18, 20, 22, 25].

The results presented in Figure 4.8 have an opposite behaviour compared to the ones from Figure 4.7. A bigger radius implies thicker fibers, and the intersection between them can become less probable because fewer fibers are needed to accomplish the desired porosity. On that account, increasing the radius decreases the effective thermal conductivity. Moreover, it is observable that the influence of the diameter in the TT direction is negligible.

4.1.3 Sensitivity analysis based on a surrogate model

To quantify how input parameters influence the overall performance of a real porous material, a very simple sensitivity analysis can be accomplished with the use of the Sobol indices, a variance-based statistical approach for global sensitivity analysis that quantifies the individual relevance of each parameter as well as their combined influence on model output, that in this case is the thermal conductivity. According to the analyses in Section 4.1.2, it is possible to conclude that porosity, angle variation and length are the parameters of most importance. Thus, a sensitivity analysis was performed with these parameters in the material model of CALCARB CBCF 18-2000. The selection of only three parameters is also founded on considering the computational efforts and the fact that there is no available information in the literature about their dependence.

To perform the sensitivity analysis, an open-source library written in python, SALib [74, 75], was used. SALib generates the model inputs using the *Saltelli sampler* function and computes the sensitivity indices from the model output through the *analyze* function. Nevertheless, first, the user needs to define the range of the input variables. Figure 4.9 shows a diagram of how the code works.

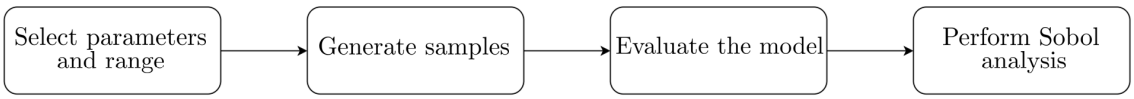

Figure 4.9: Representation of the typical four steps for a sensitivity analysis using SALib

Since running this simulation in python requires the generation of the material, following the model described in Section 4.2, the computational cost associated with generating a number of samples that allows for accurate analysis without errors, such as the lack of convergency of the Sobol indices, is not feasible. Hence, it was decided to generate and simulate the material in an identical code already developed in C^{++} since it is faster. The material model of CALCARB CBCF 18-2000 implemented in C^{++} is the same as described in Section 4.2. Nevertheless, a verification case was executed to ensure that both codes' effective thermal conductivity computation (python and C^{++}) is equivalent. A model was generated with a selected domain size of $400 \times 350 \times 380$ voxels, a radius of 4 voxels, a length of 250 voxels, a target porosity of 0.89 and a normal distribution for the angle variation out of the $x-y$ plane of $30°$. It was conducted in an argon environment at $1000\,\mathrm{K}$ and with an intrinsic conductivity of the fibers equal to $12\,\mathrm{W\,m^{-1}\,K^{-1}}$. The TIFF image from this C^{++} generation was loaded into the python code to ensure the same geometry

since the PuMA is stochastic. The differences between both simulations for the effective thermal conductivity are presented in Table 4.1. A small discrepancy in the outcomes is observed. Aside from that, the difference might be due to a variation in how the thermal conductivity iterative solver is implemented or in the way python loads the TIFF. As a result, it is reasonable to conclude that the samples can be generated employing the C^{++} code.

Table 4.1: Comparison of the effective thermal conductivity ($\mathrm{W\,m^{-1}\,K^{-1}}$) values for the in-plane and through-thickness cases obtained through a simulation in a C^{++} and python code.

	K_{IP}	K_{TT}
C^{++} simulation	0.45	0.25
Python simulation	0.42	0.23

The next step was to specify a range of the input parameters. Porosity was set to be between 0.83 and 0.95, angular variation of the fiber orientation out of the x-y plane between $0°$ and $60°$, and length between $400\,\mu\mathrm{m}$ and $700\,\mu\mathrm{m}$. The other properties for the artificial generation of CALCARB CBCF 18-2000 remain the same as previously described in Section 4.1.1. Also, the radius and length variation was assumed as 0. In Chapter 5 all the provided experimental data was measured in a helium environment. Hence, it was decided to study the influence of the variables on the effective thermal conductivity at the same medium at $943.87\,\mathrm{K}$. The intrinsic thermal conductivity of the fibers was established as $17.78\,\mathrm{W\,m^{-1}\,K^{-1}}$ [44] and for the medium as $0.34\,\mathrm{W\,m^{-1}\,K^{-1}}$ [43]. Even though in Section 4.1.1 it was concluded that for helium a domain size of 410 voxel at each direction was already representative of the total material, in this analysis it was decided to use a volume of 600^3 voxels^3 to reduce stochasticity. In the C^{++} code, there is no need to limit the domain size to save computational resources.

After having all the input variables defined for the generation of the material, 296 conductivity simulations were computed. With this, 296 random input values within the range settled and 296 outputs for each IP and TT direction were generated. Based on the samples, the analysis was then carried on. However, with this number of samples, the convergence of the Sobol indices was not accomplished.

To overcome this problem, a surrogate model was developed to simulate the model's behaviour, requiring only a few simulating points, without the expensive computational work and reducing time costs. Once constructed, the global surrogate model is reused for sensitivity analysis. It allows to calculate the underlying variances to compute Sobol indices. The Surrogate Modelling Toolbox (SMT) is an open-source python package that

comprises a set of surrogate modelling methods, sampling strategies, and benchmarking functions [76]. An interpolating model, Kriging, comprised in this package was used.

The metamodel was created with the 296 sampling data from the simulations conducted before in the C^{++} code. Additionally, 5 simulations with constant inputs were executed to retrieve the variance to add to the formulation of the Kriging model. It was found to be 2.04×10^{-7}. To first understand how the model works and how to use it, it was built for one single variable, the porosity. Therefore, for the same parameters of the synthetic model described in Section 4.1.1, 50 samples were generated having the effective thermal conductivity in the IP and TT directions as outputs. For this purpose, the data was split into training, 80 %, and testing, 20 %. The results are shown in Figure 4.10.

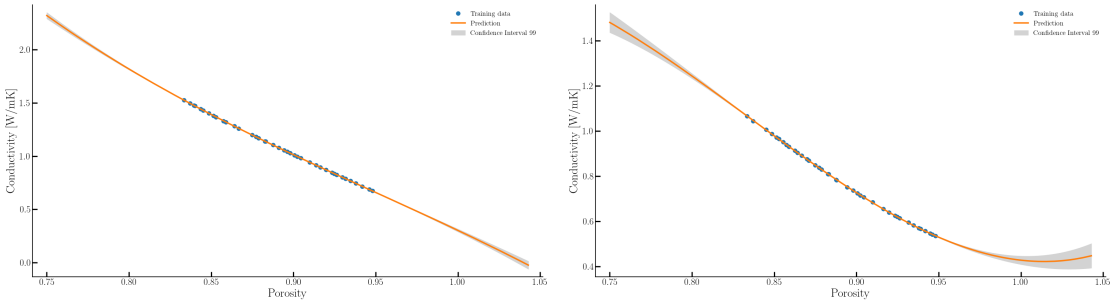

(a) In-Plane. (b) Through-Thickness.

Figure 4.10: Representation of one-dimensional data interpolation for porosity with 50 training points.

It is possible to observe good conformity in the results, having an adequate prediction of the model's behaviour. Model accuracy is usually evaluated by comparing the response data produced by the initial sampling with the corresponding data predicted by the surrogate model. To do so, cross-validation was selected since it works with a small number of sample points, avoids overfitting and underfitting and does not require any further simulations. The results are presented in Figures 4.11 and 4.12.

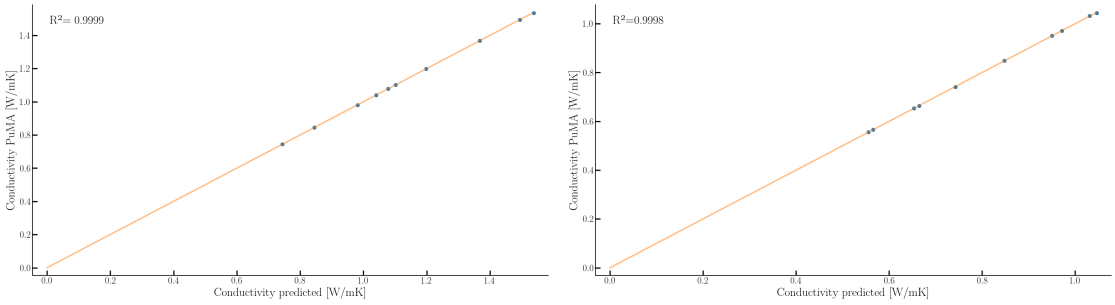

(a) In-Plane. (b) Through-Thickness.

Figure 4.11: Training accuracy of the proposed surrogate model.

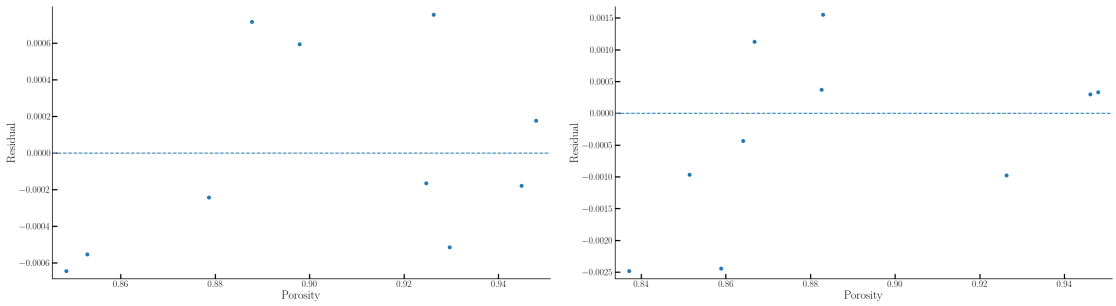

(a) In-Plane. (b) Through-Thickness.

Figure 4.12: Residual plot describing the difference between actual and predicted values of porosity.

Figure 4.11 evaluates the model's performance, determining how effectively the regression model predicts different response values. For a perfect prediction, the predicted values should be equal to the actual values. The prediction error for a point is represented by the vertical distance from the line to that point. From the graphs in both IP and TT directions, it is possible to conclude that all the points lie on a diagonal line, making this model very efficient. In Figure 4.12 it can be noticed that the points are scattered randomly around the 0 line, exhibiting no pattern. This agrees with the conclusions taken before that the Kriging method implemented is accurate for the model prediction.

Subsequently, the surrogate model was employed in our initial problem with the three variables and 296 training points. An assessment of the accuracy was also made by splitting the data into $80\,\%$ for training and $20\,\%$ for testing and is presented in Figure 4.13.

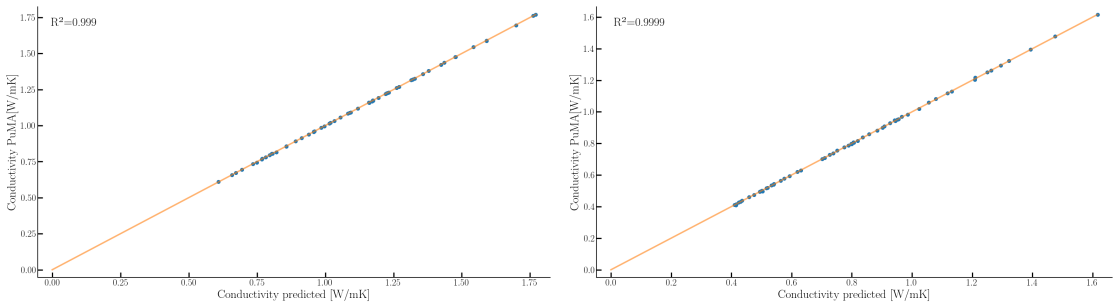

(a) In-Plane. (b) Through-Thickness.

Figure 4.13: Training accuracy of the proposed surrogate model for three variables.

Once constructed and validated, the surrogate model is used to compute Sobol indices. Figures 4.14, 4.15 and 4.16 provide information on the number of samples required to converge each Sobol indices for each variable and direction.

It can be inferred that the second-order indices are the most critical, requiring more samples to converge. Figures 4.17a, 4.17b and 4.17c show the results from the sensitivity anal-

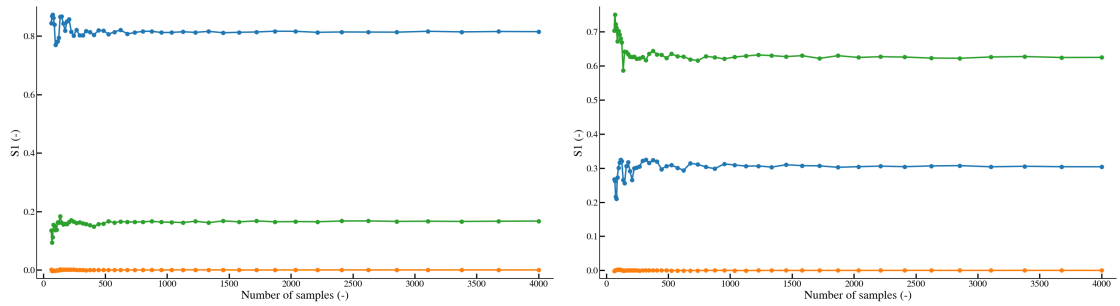

(a) In-Plane. (b) Through-Thickness.

Figure 4.14: Number of samples required to achieve the convergency of the first-order indices. The porosity is represented in blue, the fiber orientation in green and the length in orange.

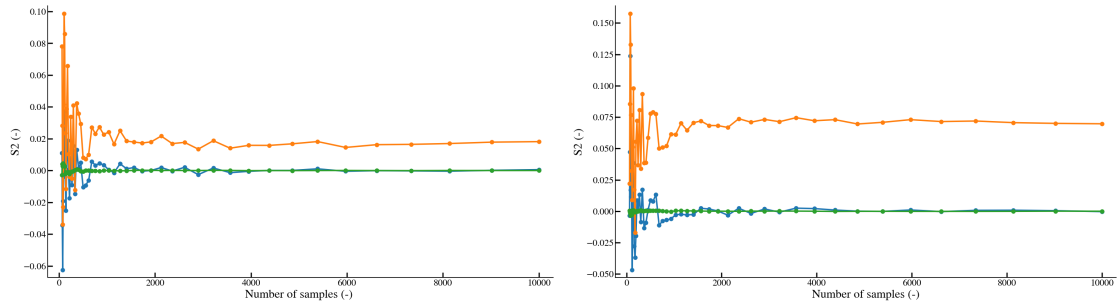

(a) In-Plane. (b) Through-Thickness.

Figure 4.15: Number of samples required to achieve the convergency of the second-order indices. The blue bar represents the influence of porosity-length, the orange bar the effect of porosity-angle and the green bar the impact of the fiber's length-angle on the effective thermal conductivity.

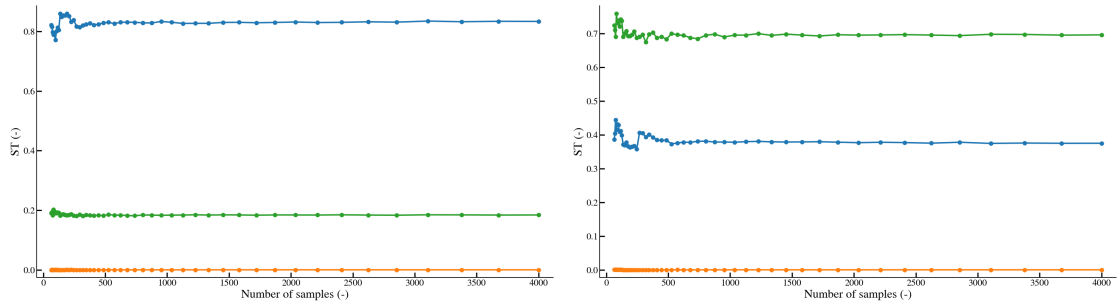

(a) In-Plane. (b) Through-Thickness.

Figure 4.16: Number of samples required to achieve the convergency of the total-order indices. The porosity is represented in blue, the fiber orientation in green and the length in orange.

ysis for helium at $943.87\,\mathrm{K}$ for the three variables at the IP and TT direction with 12000 samples. The first-order indices independently measure the contribution to each variable's output variance. In contrast, the second-order indices estimate the contribution to the output variance induced by the interaction of two input parameters. The total order includes the sensitivity of both first-order effects and the sensitivity due to interactions described by the second-order indices.

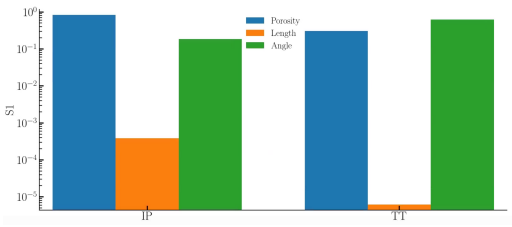

(a) First-order indices.

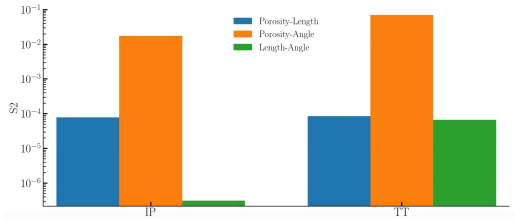

(b) Second-order indices.

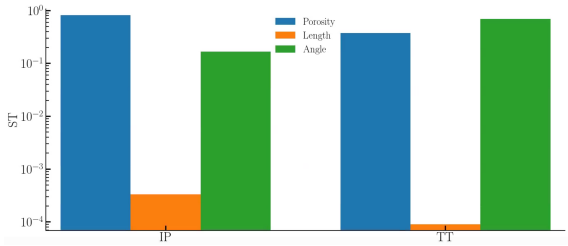

(c) Total-order indices.

Figure 4.17: Sobol indices are given for each variable accounting for effect on the effective thermal conductivity ($\mathrm{W\,m^{-1}\,K^{-1}}$).

The results follow the outcomes of the parametric study conducted in Section 4.1.2. For the IP direction, porosity has a more considerable influence on the thermal conductivity, whereas in the TT plane is the fiber orientation. The length has a very low impact. Due to the scarcity of information in the literature about the contribution of the interaction of two input parameters on the thermal conductivity for ablators materials, Figure 4.17b is essential and allows to conclude that porosity and angle have a considerable influence over the final output.

4.2 Development of the CALCARB CBCF 18-2000 material model

Considering that the python version of PuMA has a material generator implemented with a uniform distribution for the fiber´s orientation, $\mathcal{U}(-\sigma\sigma_f, \sigma_f)$, in both IP and TT directions, it was necessary to adjust the code to our material, CALCARB CBCF $18-2000$, which has a uniform distribution in the TT direction. A new implementation of the fiber distribution model was developed to establish a uniform distribution of fibers in the IP, $\mathcal{U}(0,\ 360)$, whereas in the through-plane a normal distribution $\mathcal{N}(0, \sigma_f)$ was specified. As already mentioned, σ_f represents the standard deviation of the angle between the IP and in the case of our material, CALCARB CBCF 18-2000, is $30°$ [15]. If the uniform distribution between $-30°$ and $30°$ was kept, it would not allow for any variation of the fibers out

of these bounds. In microscopy, it is possible to sometimes observe a small number of fibers that go outside these values. So, a uniform distribution would not comply with the actual material. Figure 4.18 shows the differences between both implementations in the IP plane and the implication that it will have in the effective thermal conductivity.

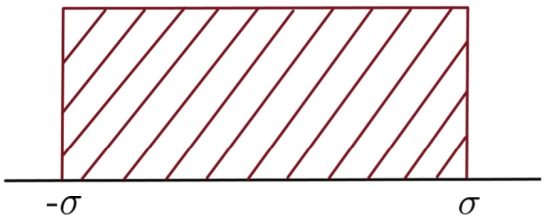

(a) Uniform distribution (PuMA original code).

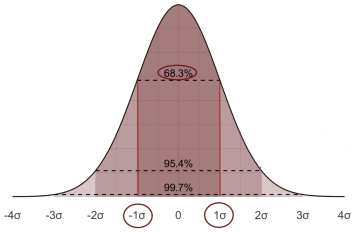

(b) Normal distribution (new implementation).

Figure 4.18: Differences between both implementation of the quantity of fibers present in the IP plane.

Consequently, a new geometry generator was developed. The first phase consisted of understanding the necessary steps to develop a fiber, as illustrated in Figure 4.19. A point is randomly selected and its coordinates are restricted to the maximum and minimum values of the domain. To define the second point, the last coordinate of the fiber, it is required first to construct the orientation vector since the length is known as an input. To accomplish that, the angles must be assigned. Figure 4.19 shows that θ was set as the azimuth and has a uniform distribution, while ϕ was defined as the elevation with a normal distribution. Thereupon, a rotation of the azimuth angle around the z axis, equation 4.1, followed by the rotation of the elevation angle in the y axis, equation 4.2, was necessary to construct the orientation vector. Finally, a volume is assembled around the fiber's centerline.

$$R1 = \begin{bmatrix} \cos & \sin\theta & 0 \\ -\sin\theta & \cos & 0 \\ 0 & 0 & 0 \end{bmatrix} \quad (4.1) \qquad R2 = \begin{bmatrix} \cos\phi & 0 & -\sin\phi \\ 0 & 1 & 0 \\ \sin\phi & 0 & \cos\phi \end{bmatrix} \quad (4.2)$$

To ensure that the angle's orientation part of the implementation was valid, a verification was conducted with a test case where 300 centred fibers were generated in the middle of the domain. The test example is displayed in Figure 4.20.

Histograms of both uniform and normal distributions were plotted for additional verification. Figure 4.21a shows that for the uniform distribution implementation the code is working properly, since it agrees with the range values selected for the azimuth, $0°$ and $360°$. For the normal distribution, $\mathcal{N}(0, \sigma_f)$, σ_f should be bigger than the selected value

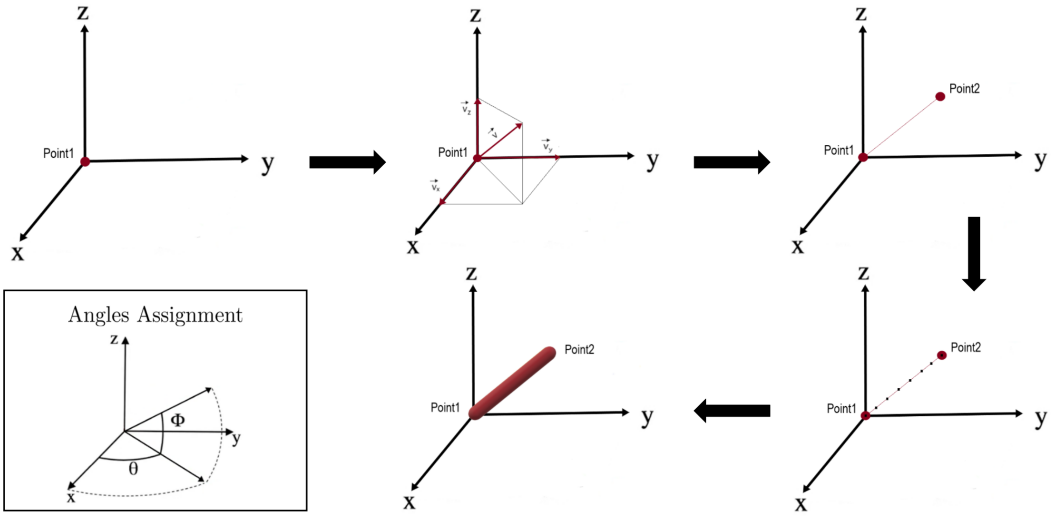

Figure 4.19: Successive steps of the fiber's development.

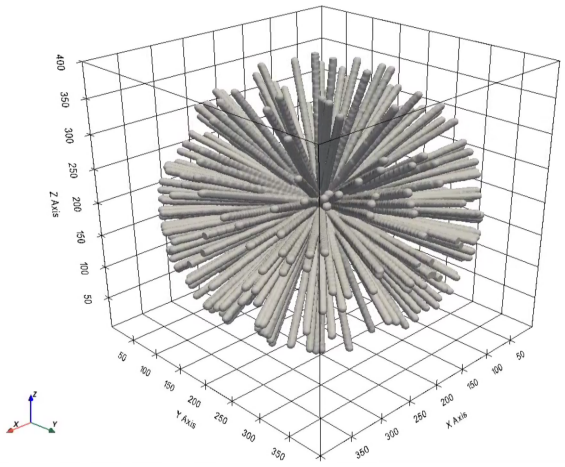

Figure 4.20: Visualization of multiple fibers generated centred in the middle of the domain.

for σ_f. This values agree with the mean, μ, and standard deviation, σ_f, in Figure 4.21b.

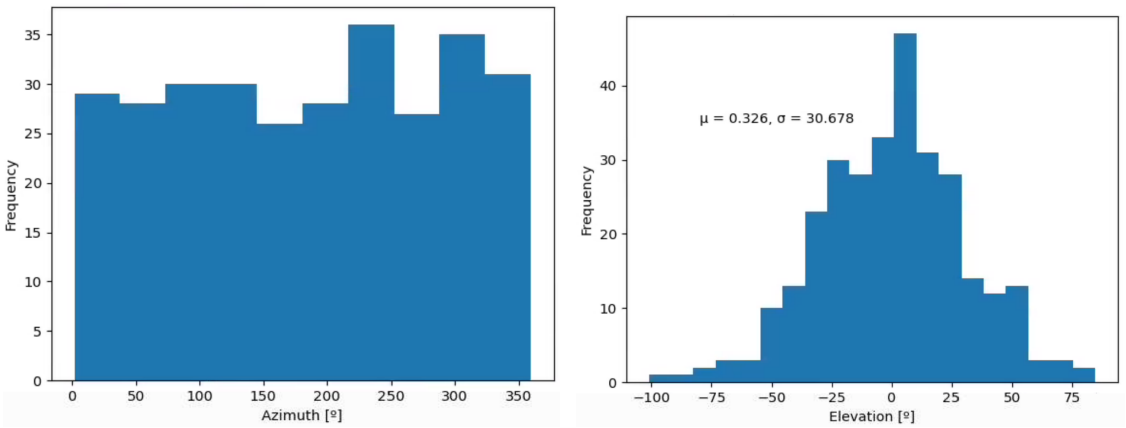

(a) Uniform distribution.

(b) Normal distribution.

Figure 4.21: Verification of the angle distributions implemented.

Once this part is verified, the second step consisted in generating random fibers in the domain. These fibers were built in a way that they randomly intersect one another. Consequently, the periodic boundary conditions were applied. Figure 4.22 exemplifies its employment to fibers in a 2D illustration. A colour depicts each part of the fiber that overpasses the domain. With the periodic boundary condition applied, that part of the fiber appears at the same position on the opposite side of the domain with the same orientation. The same approach is utilized in a 3D domain.

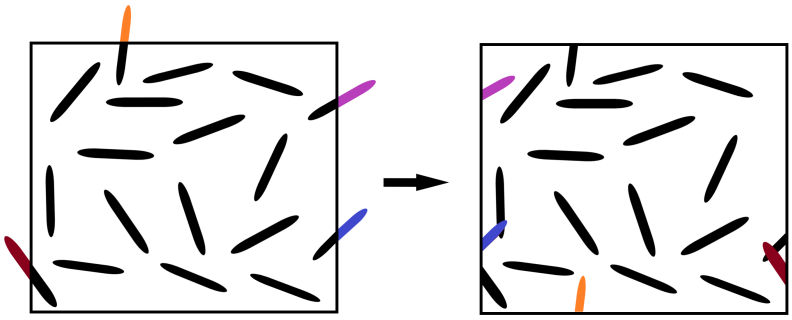

Figure 4.22: 2D representation of the periodic boundary conditions applied.

After creating all the fiber points in the code, they enter a loop to inspect if there is any point with coordinates bigger or lower than the domain. By construction, this last case can only happen to the coordinates in the z axis. If so, periodic boundary conditions are applied. As long fibers can cross over the domain more than once, using it one time cannot be enough. To overcome this problem, an iterative process was carried out to ensure that fibers lie within the domain. At the end of the generation function an ID for each phase (i.e. fiber and medium) was settled as 1 and 0, correspondingly. In Figure 4.23 it is possible to visualize 1 fiber randomly generated with the periodic boundary conditions applied, confirming that this part of the code is functioning correctly.

At this point, as a first step, generation was only based on the inputted number of fibers. However, for a real material application, the provided property is porosity. For that reason, the possibility of generating fibers by taking into account the number of fibers needed to attain the target porosity given by the user was added. Since the radius of the fiber is known, it is possible to estimate the volume of each of them. With this and the total volume of the domain, the volume fraction of the total fibers contained in the domain is determined and, consequently, approximates the number of fibers required. It is also important to mention that this number of fibers is not an exact value due to the possibility of fiber intersection and this is why the implementation of the generation loop is neces-

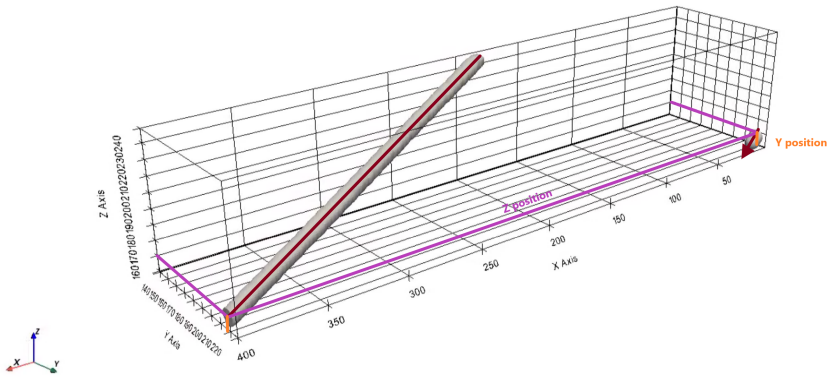

Figure 4.23: Demonstration of a test case of 1 fiber generated with the applied periodic boundary conditions.

sary. To ensure that less fibers are generated in the first loop, only 80 % of the calculated number is used. The computed porosity is set initially as 1 and while this value is higher than the defined target porosity, new fibers are generated inside the loop. After the generation, the porosity is retrieved. A volume fraction of the new generated fibers is computed as well as the number of needed fibers. The while loop is stopped if the latest is equal to 0. If not, more fibers will be added until the required number is achieved. It is important to mention that the new generated fibers are added to the previous ones in the domain. As they can overlap, after the generation function an ID of 2, which corresponds to the sum of two fibers, is fixed as 1. The ID allows for the identification of the different phases, which in this case corresponds to the medium and fiber. Figure 4.24 showcases the generation of random straight fibers given a target porosity of the overall material equal to 0.89.

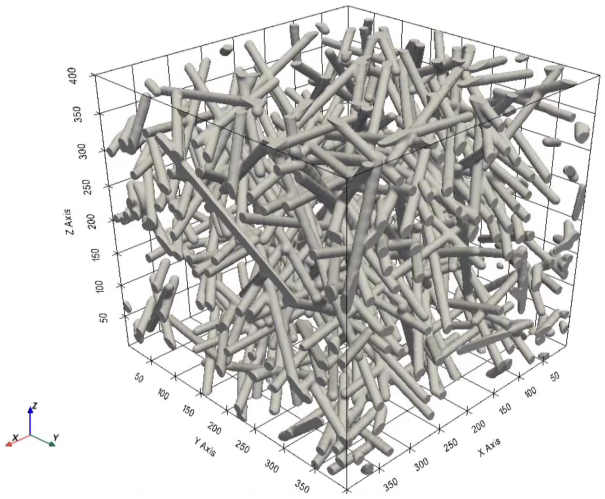

Figure 4.24: Artificial generation of random straight fibers for a given porosity of 0.89.

4.2.1 Validation with experimental data

The developed model in Section 4.2 can be applied to transversely isotropic ablator materials, if validated from available experimental measurements, to simulate and predict the effective thermal conductivity of the experiments under different conditions.

The conductivity simulations of the material model were compared against the available experimental data from Mersen Ltd [41, 42]. These measurements are provided as functions of the temperature and the medium in which the experiment was conducted and are presented in Table 2.1. Since there is no information regarding the direction of the measurements, private communication with the manufacturer clarified that it is in the TT direction. As a result, a reasonably accurate approximation of the effective conductivity computed using the *pumapy* model compared with the measurements should be achieved in the through-plane.

The simulations of the effective conductivity were executed in two different mediums, argon and nitrogen, as a function of the temperature. The range of temperatures used followed the data available for the intrinsic thermal conductivity of the rayon fibers preheated at HTT = $2500\,\mathrm{K}$ from Pradere [44]. For the corresponding temperatures, the medium's conductivity was retrieved through Mutation++ [43]. The parameters provided in Section 4.1.1 were used to generate the material, with a domain volume of 600 vx.

It is important to note that a $\pm 2\ \%$ porosity variation was included in both simulations to account for the variability in the bulk density encountered in the real material. However, due to the execution time required per simulation, this was only imposed at the minimum and maximum temperature. In spite of that, it is still possible to infer about the $\pm 2\,\%$ trend curve. Besides that, it was also decided to plot the values of the effective conductivity for the IP and TT directions from the original PuMA code to demonstrate that the previous implementation was not accurate for the material in the study. The results obtained from the simulations in argon and nitrogen are depicted in Figures 4.25 and 4.26, respectively.

There is a good agreement between the effective conductivity values obtained experimentally and computationally in the argon environment (Figure 4.25). For the nitrogen environment (Figure 4.26), it is possible to observe that the experimental values are slightly higher, particularly for lower temperatures, when compared with the simulated ones. This could be due to a variation in porosity. A smaller porosity of the material would increase

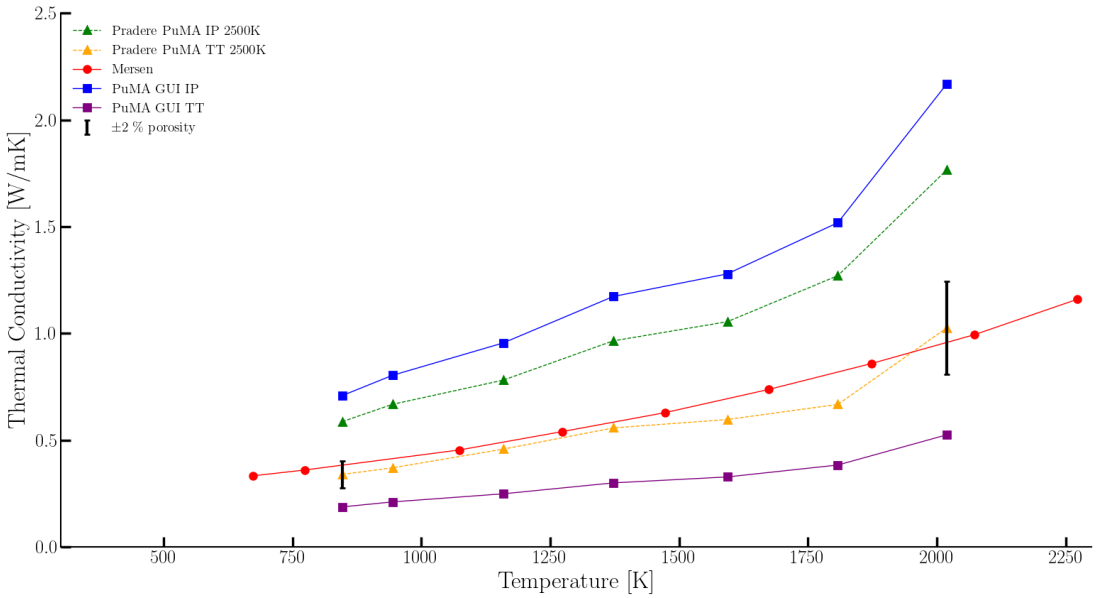

Figure 4.25: Comparison of experimental and computationally determined values for the effective thermal conductivity of Calcarb CBCF 18-2000 as a function of temperature in an argon environment.

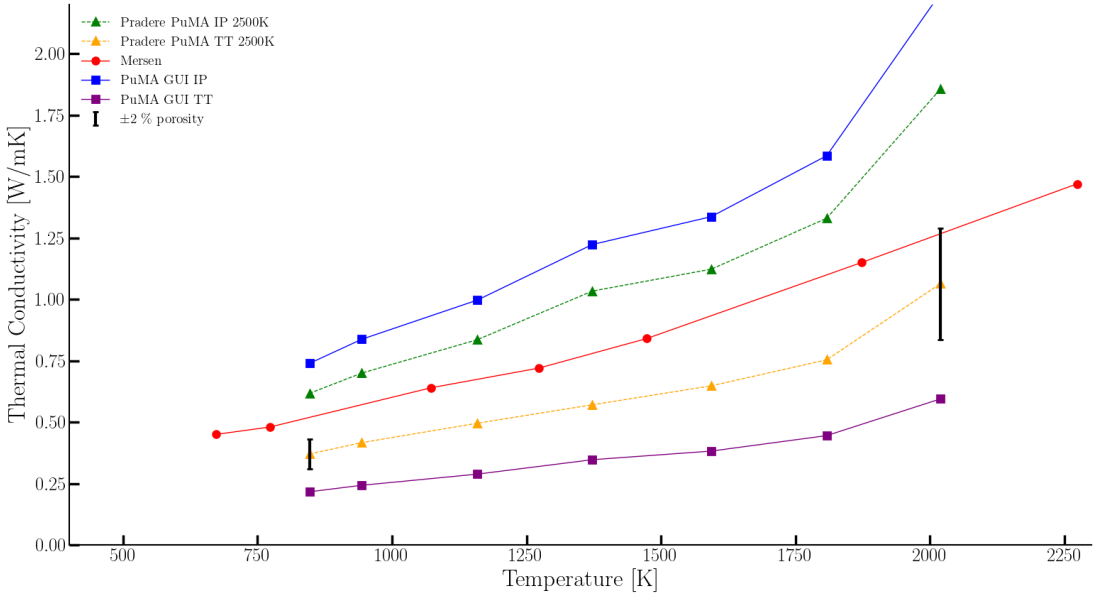

Figure 4.26: Comparison of experimental and computationally determined values for the effective thermal conductivity of Calcarb CBCF 18-2000 as a function of temperature in a nitrogen environment.

the effective conductivity, enhancing the comparison. In a porous material this variability is reasonable. Validation from experimental data was also conducted for vacuum but not reported here, revealing also a great agreement.

The current study validates the CALCARB CBCF 18-2000 material model, meaning that the developed response code is reliable for estimating the thermal behaviour of the real

material.

4.3 Material model with fiber coating

As previously addressed in Section 2.1, ablative materials, when exposed to high-enthalpy flow conditions during the atmospheric entry, experience a series of physical and chemical processes. As the temperature of the material increases, the resin that is a component of the composite, gets pyrolyzed, which can be defined by its degradation and carbonization, generating a carbonaceous char. A significant part of this char gets attached to the carbon fibers and can also fuse with them [18]. The material is then in a charred state.

Adding the char leads to a variation in the porosity and effective thermal conductivity of the overall material. Hence, it is necessary to accurately characterise the material's thermal response after pyrolysis. Since PuMA does not include the possibility to generate and simulate the conductivity of a material in a charred state, this section covers the development of a model of coated fibers in *pumapy*.

SEM pictures of charred ZURAM, presented in Figure 4.27a, confirm that the fibers are covered with charred resin. The char seems to be displayed in a web of interconnected spheres formed on top of the fibers. However, in Figure 4.27b it is possible to observe that the deposition of char on the fibers appears to have a uniform distribution, similar to a coating around all the fiber.

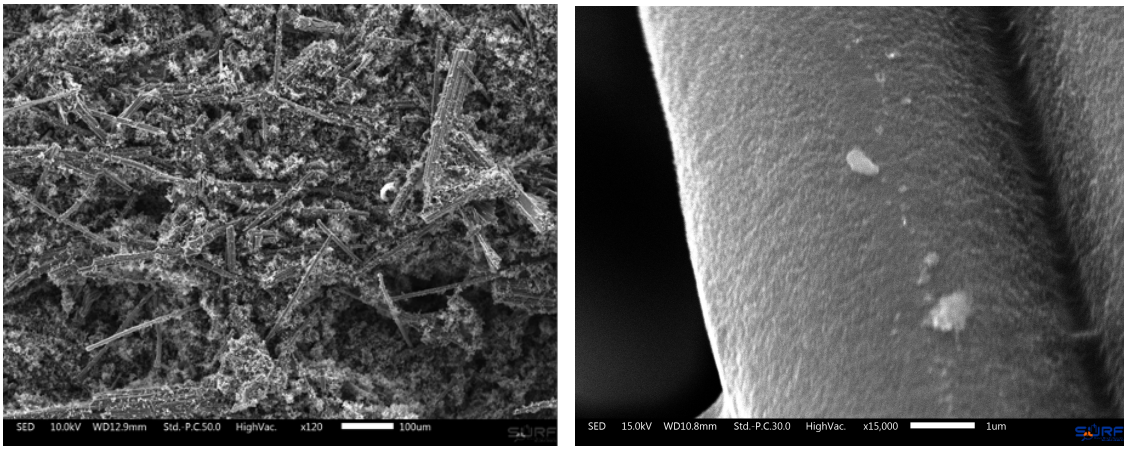

(a) ZURAM [18].

(b) CALCARB CBCF 18-2000 [2].

Figure 4.27: SEM pictures of a charred state material taken at a different scales.

Since it was the first attempt to develop a numerical code that enclosed fibers and charred

resin, it was decided to assume a uniform coating due to its simplicity. So the model will try to replicate Figure 4.27b. Furthermore, it was considered that all fibers have a coating of charred resin, even though this might not be a precise representation of the real material.

The biggest challenge is ensuring that fibers and coating have the exact coordinates and orientation. Since the fibers are randomly allocated in the domain and for each porosity loop new fibers are created without storing the previous position, the only feasible solution found was to generate both at the same time in the same workspace. To accomplish that, two cylinders with the same centerline and length but different radius were generated, as portrayed in Figure 4.28.

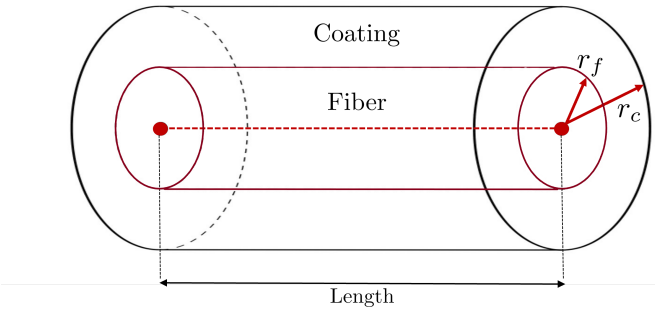

Figure 4.28: Visualization of the geometrical implementation of the charred resin coating.

The fibers are created as in Section 4.2. When creating the volume of the fibers, a second volume is added for the coating with the corresponding radius that the user can input. It should be noted that the input radius is not the thickness of the coating but the radius starting from the centerline, as depicted in Figure 4.28. If the user does not know the radius of the coating, the target volume fraction of the charred resin for the overall material can be used and the radius will be automatically determined. These two parameters, as well as the ones described in Section 4.2, are required to generate coated fibers. Consequently, to discern between both materials, the next step was to define an ID for them. An ID of 1 was appointed for the fibers, 20 for the coating and 0 for the medium. The number 20 was chosen to avoid confusion as clarified hereafter. At the end of each iteration, since fibers are allowed to intersect, the interconnection of the materials and consequent sum of material ID can happen, which is not desired. To avoid it, a matrix with all possible intersections was assembled, as exemplified in Table 4.2.

At this point, only the intersection between the coating and the fiber material is concerning. The coating should not exist inside the fibers, so the ID of 21 should be fixed again as

Table 4.2: Possibility matrix of the material intersections at the end of the generation function.

	Medium	fiber	Coating
Medium	0	-	-
fiber	1	-	-
Coating	20	~~21~~ 1	-

1. For a better understanding, a 2D demonstration follows in Figure 4.29.

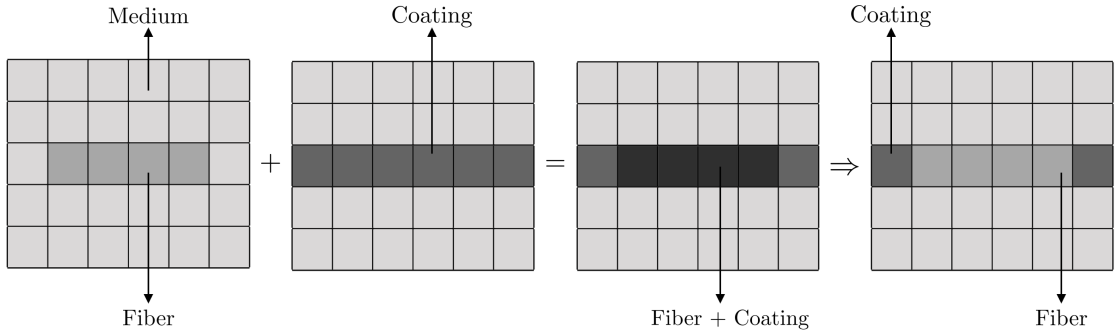

Figure 4.29: 2D representation of a possible intersection between fiber and coating and solution.

As shown in Section 4.2, the calculation of porosity is an iterative process and a function of the number of fibers required to achieve the target porosity. Therefore, if at the end of each loop the number of fibers is still not the desired, more will be generated. Since this means that fibers with coating will be created at different moments, Table 4.2 needs to be extended as presented in Table 4.3. Moreover, to ensure that coating is not added in more quantities than it should according to the given volume fraction, only a percentage of the coating is added to the first porosity iteration. As more fibers are generated, more coating will be added. This percentage can be modified in order to achieve the desired volume fraction of the coating.

Table 4.3: Possibility matrix of the material intersections at the end of each porosity loop.

	Medium	fiber	Coating
Medium	0	-	-
fiber	1	~~2~~ 1	-
Coating	20	~~21~~ 1	~~40~~ 20

Choosing an ID of the coating equal to 20 ensures no confusion and allows for the differentiation of the material. At the end of each porosity loop, the correct ID values are re-assigned. The sum of fibers plus fibers is established as fiber (ID=1), fibers plus coating as fibers (ID=1) and coating plus coating as coating (ID=20). A 2D representation of possible intersections is depicted in Figure 4.30

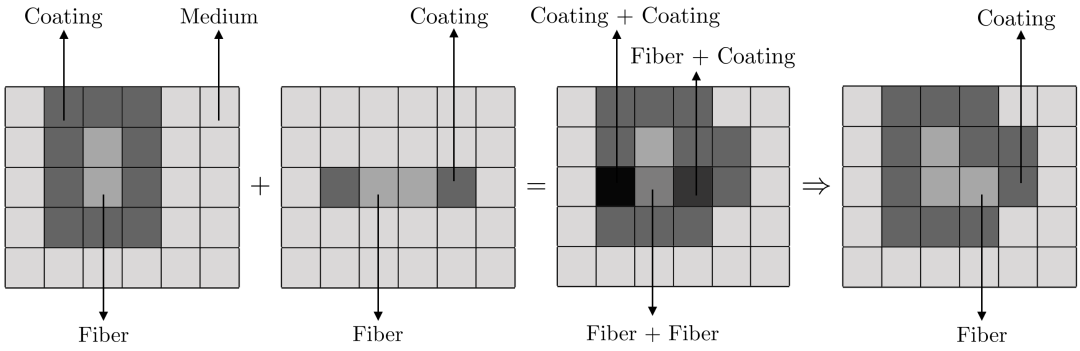

Figure 4.30: 2D representation of a possible intersection between coated fibers and solution.

To visualize this generation, a test case was executed and it is showcased in Figure 4.31. It can be seen that the coating is uniformly formed around all fibers of the domain. A verification of this implementation is described in Section 4.3.1.

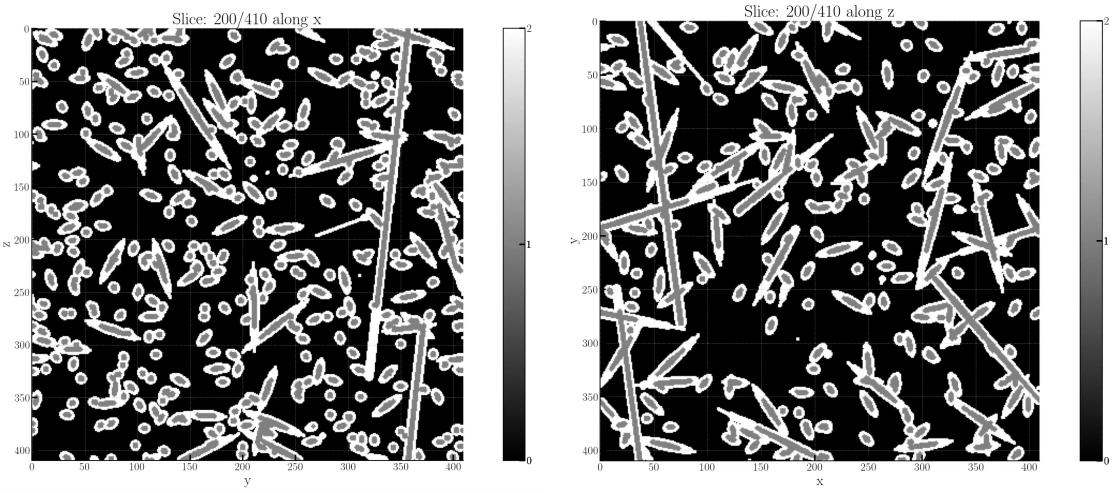

Figure 4.31: Visualization of a slice of the material at the same position for the implementation of the coating in a test case.

4.3.1 Verification of the simulated model

To verify the developed model, a test case was conducted and consisted in imposing the same volume fraction for the fibers and charred resin. Thus, it would be achievable to evaluate its precision by retrieving the computed volume fractions based on the code described in Section 4.3 and comparing them with the expected values.

For the artificial generation, the input parameters are equal to those described in Section 4.1.1 with a domain size of 410 voxels in each direction. The only exception is the porosity

which was selected as 0.9[1]. Since the volume of the fibers is equal to the volume of the coating, for a fiber´s radius of 3 voxels, according to equation 4.3, the radius of the coating from the centerline should be equal to 4 voxels.

$$\text{Volume}_{\text{coating}} = \text{Volume}_{\text{fiber}} \Rightarrow r_{\text{coating}} = \sqrt{2r_{\text{fiber}}^2} \quad (4.3)$$

For a target porosity equal to 0.9, the volume fraction of the fibers is 0.1. Considering that the coating has the same volume fraction, the computed porosity is expected to be 0.8. The comparison between the expected and the computed results are shown in Table 4.4.

Table 4.4: Test case results comparison.

	Expected values	Computed values
Volume fraction of fibers	0.1	0.10
Volume fraction of coating	0.1	0.08
Porosity	0.8	0.82

The obtained results are very similar to the expected values. This is explained by the fact that the computation of porosity is an iterative process and because only integers can be inserted for the radius. Subsequently, the value for the radius to generate the same volume fraction should be 4.25.

In addition, another test case was executed to verify if the developed code and the thermal conductivity iterative solver operate as intended. This second test imposes that $K_{coating} = K_{fibres}$, which simply represents thicker fibers. It compares the thermal conductivity output of the CALCARB material model generated in Section 4.2 with the thermal conductivity results from the coating model developed in Section 4.3. For the generation of the CALCARB model, the required inputs are stated in Section 4.1.1. The differences remain in the diameter of the fiber, which was established as $5\,\mu\text{m}$. The number of fibers needed to achieve a porosity equal to 0.86 was found to be 223. For the thermal simulation, a fiber conductivity of $15.63\,\text{W}\,\text{m}^{-1}\,\text{K}^{-1}$ was set. Regarding the artificial generation of the coating model, a fiber and coating radius from the centerline equal to 3 and 5, respectively was specified. The remaining inputs are the same as those selected for fiber generation. Both simulations were conducted in a helium environment at $846.54\,\text{K}$. Table 4.5 depicts the results.

It can be concluded that the developed code is effective and can be applied to Section 5.1.

[1]Refers to the porosity of CARLCARB CBCF $18 - 2000$ without coating.

Table 4.5: Comparison of the outcomes of the CALCARB CBCF 18-2000 and coating thermal conductivity simulations in both IP and TT directions. The conditions given are: k_{coat}=k_f=15.63 $\mathrm{W\,m^{-1}\,K^{-1}}$ and k_{gas}=0.318 $\mathrm{W\,m^{-1}\,K^{-1}}$.

	CALCARB model	Coating model
k_{IP}	1.11	1.10
k_{TT}	0.76	0.78

4.4 Artificial generation of ZURAM virgin material

The manufacturing process of ZURAM consists of impregnating the carbon preform CALCARB with a porous phenolic resin. So it can be assumed that the resin fills the spaces between the fibers. From Figure 4.32, it is conceivable to presume that the material geometry resembles a foam. The bubbles that the material seems to have are related to the gas that is trapped inside. With the intent of developing a numerical tool replicating virgin ZURAM, it is necessary to consider the artificial generation of a multiphase material assembled by fibers, resin and the medium. This code will be used in Section 5.2 to compare with the results obtained under the European Space Agency (ESA) project, the TRP ReChar (Reliable material characterisation methods for Thermal Protection Systems critical ablative materials).

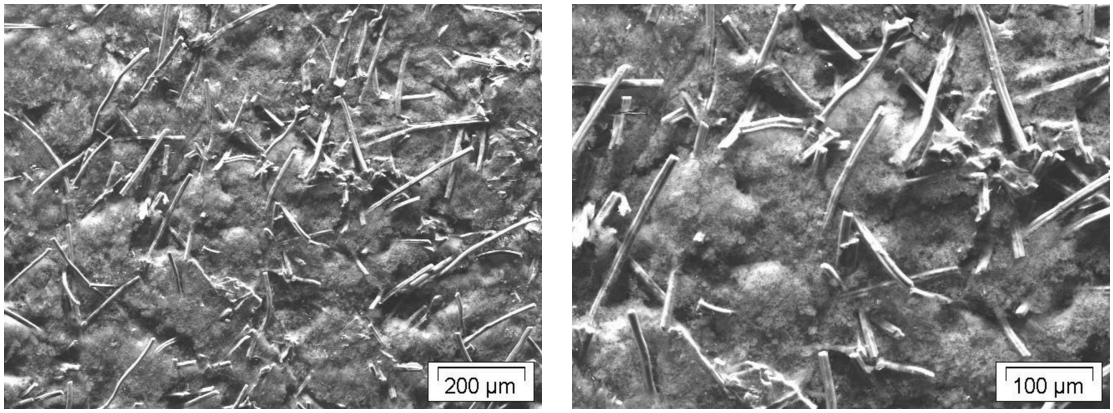

Figure 4.32: SEM micrograph of virgin ZURAM showing the carbon fibers surrounded by the phenolic resin.

The formation of this material consisted of three steps. First, the carbon fiber preform was generated according to the material model of CALCARB CBCF 18-2000 presented in Section 4.2. Then, since the gas seems to be in what appears to be spheres within the material, a first approach consisted of generating a material of random spherical structures. For this, the random intersecting spheres function implemented in *pumapy* was used. Lastly, the two materials are combined into a single domain. To be able to distinguish the different phases of this material, it was settled on an ID of 1 for the fibers, 2

for the spheres (gas) and 0 for the medium that is the phenolic resin. Moreover, it was defined that in case of overlapping of the materials, the fibers inside are always only made of carbon.

However, as it will be explained in Section 5.2 in more detail, this geometry was not suitable due to the minimum sphere diameter. Also, it was considered physically incorrect since the bubbles would be very small in the real material. As a solution, instead of spheres, a cloud of uniformly distributed voxels in the domain was generated. This allows for a higher number of structures due to their small dimensions, increasing the volume fraction of the gas, which was the previous problem. The implementation of the square voxels generation was built based on the code presented in Section 4.2. The dissimilarity is in the generation function of the structure once for the voxel, only a random point in the domain needs to be designated.

Figure 4.33 shows a slide of both implementations in the same material at the same position along the z direction. The decision to plot a 2D slice of the material consists of the difficulty of having the correct opacity to be able to contrast the three phases of the material in a 3D visualization.

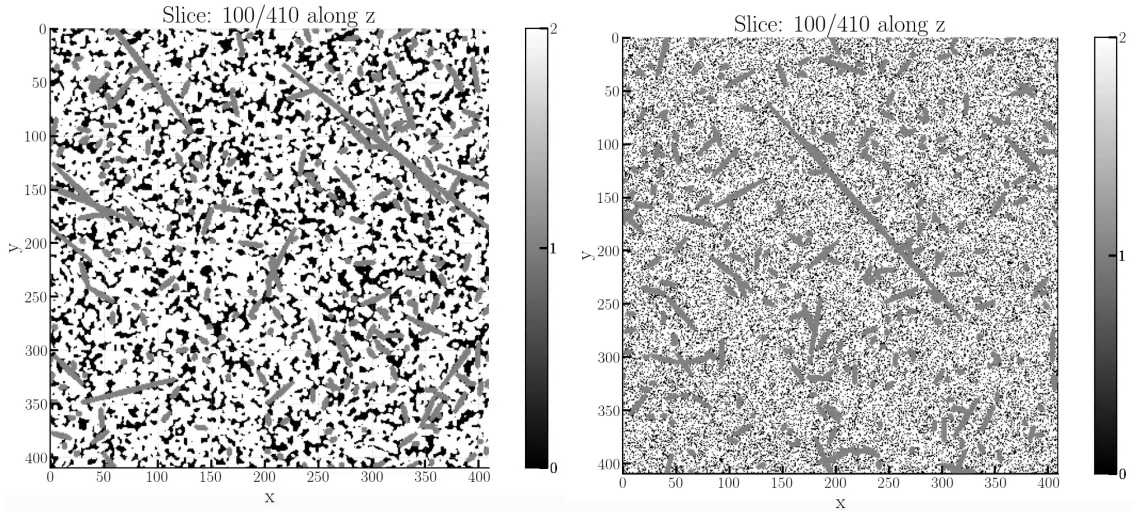

(a) Spheres generated as phenolic resin

(b) Voxels generated as phenolic resin

Figure 4.33: Visualization of a slice of the material at the same position along z direction for both implementations. fibers are represented in grey, the phenolic resin in white and the gas trapped in black.

Chapter 5

Application

In this chapter, simulations with the models developed in Sections 4.2 and 4.3 for both virgin and charred ZURAM material are compared with experimental data for the thermal conductivity of virgin and charred ZURAM[1]. Finally, a study of CALCARB CBCF 18-200 in PuMA software is performed to understand the effect of graphitization on the intrinsic thermal conductivity of the carbon fibers.

5.1 Reproduction of Laser Flash Analysis test cases for fully charred material

As aforementioned in Section 2.1, ZURAM material at a charred state contains char produced during the pyrolysis of the phenolic resin. Part of this can be deposited on the fibers and melt with them. Previous studies have shown that the material model developed for CALCARB in Section 4.2 is not very suitable to be applied to charred ZURAM. Even though just a small quantity of char remains attached to the fibers, since the other part falls from the material, applying the model for CALCARB CBCF 18-200 to compare with the experimental measurements will not translate into a good agreement. The inclusion of the char can affect the porosity and effective thermal conductivity of the material. Thus, the model presented in Section 4.3 was applied to compare the simulation results to the available experimental data to understand if the developed numerical tool can accurately simulate the material's thermal response after pyrolysis.

The experiment results were obtained by means of LFA in an inert helium atmosphere at ambient pressure. These analyses used samples of ZURAM material pre-charred in an argon environment at 1100 K for three hours. This thermal treatment allows for the pyrolysis of the resin. For the thermal diffusivity measurements, the samples were submitted to high temperatures up to 3060 K and the effective thermal conductivity was compared

[1]Obtained under the ESA TPR ReChar project

in the IP and TT directions [34].

To perform the simulations in *pumapy*, the known required parameters are equal to the ones referred to in Section 4.1.1 for CALCARB generation (fiber's length and radius, ε and angle variation), as well as the volume fraction of the charred resin or the radius of the coating. Since the simulations considered the medium as the testing gas, helium, the domain size, according to Section 2.3, is equal to 410^3 vx. This study will only use the volume fraction of the char since from pyconmetry it is possible to asses about its value.

From the measurements available through pyconmetry of fully charred ZURAM, the porosity of the bulk material (fibers + char) is equal to 0.843. Knowing that the volume fraction of CALCARB is equivalent to 0.11 it is possible to determine the volume fraction of the charred resin as 0.046. Is it essential to note that first, the preform material, in this case CALRCARB, is generated by setting it to its nominal porosity. Then, the fibers are coated and the char is added, which in the end provides a new true porosity. In order to have the desired final porosity, the volume fraction of the char needs to be properly adjusted. This value is iterated by the user since the option of fiber intersection reduces the real porosity and cannot be assessed beforehand.

At the end of the fibers and coating generation the volume fraction of the fibers, coating and porosity were retrieved to evaluate if the previous values were achieved. Table 5.1 shows the difference between the simulated and measured values.

Table 5.1: Comparison between the volume fractions measured and simulated for charred ZURAM and error associated.

	Measured (-)	Simulated (-)	Error (%)
Porosity	0.8435	0.8413	0.26
Volume fraction fibers	0.11	0.1099	0.09
Volume fraction coating	0.0464	0.0486	4.74

It is possible to conclude that the geometry generator is precise for this case since the associated error is small. As already mentioned, the value of the volume fraction of the char is iterated and for this study, the best accomplished result was with a $60\,\%$ of the volume fraction of the coating.

To conduct the bulk thermal conductivity simulations of charred ZURAM and compare with the experimental data, the thermal conductivities of each phase ought to be known. Both intrinsic conductivities for fibers and medium are a function of the temperature. The intrinsic conductivity of the fibers was computed from [44], while the conductivity of

helium was determined using Mutation++ [43]. The conductivity of the charred resin is unknown. However, literature [77] reports the intrinsic thermal conductivity of phenolic char in the order of $1\,\mathrm{W\,m^{-1}\,K^{-1}}$. Therefore, this value was employed.

However, since there was some disparity between the simulated and the experiment results in both IP and TT directions, it was decided to investigate the final retrieved porosity's effect by increasing it to a selected value of 0.86. The outcome of this analysis is displayed in Figure 5.1

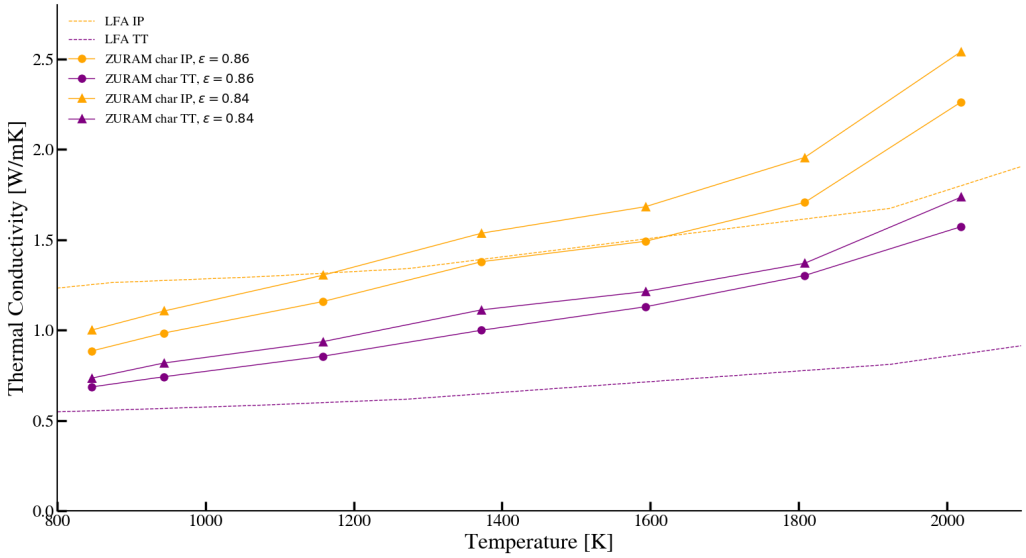

Figure 5.1: Comparison between the simulations from PuMA and the experiments on LFA (dashed lines) for a final porosity of 0.84 and 0.86 of charred ZURAM.

After concluding that a bulk porosity of 0.86 fits better, it was decided to study the intrinsic conductivity of the char by selecting a value equal to $0.01\,\mathrm{W\,m^{-1}\,K^{-1}}$. The results are showcased in Figure 5.2.

As referred before in Section 4.3, considering a uniform distribution for the charred resin on the fibers might not be a strong assumption. In this case it is being considered that the coating involves all fiber, which can be the reason for having higher conductivities.

5.2 Comparison with experimental data on virgin ZURAM

The thermal conductivity of virgin ZURAM was measured by means of LFA and GHP. The experiments were conducted in a helium environment at ambient pressure, and the thermal conductivity outcomes are supplied in the IP and TT directions for the LFA and

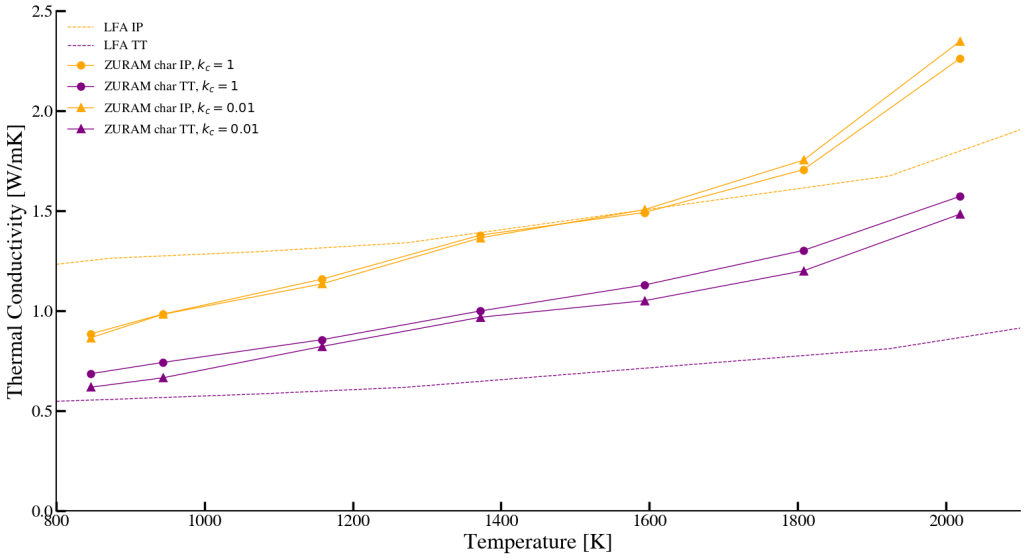

Figure 5.2: Comparison between the simulations from PuMA and the experiments on LFA (dashed lines) for both 1 and 0.01 $\mathrm{W\,m^{-1}\,K^{-1}}$ of charred ZURAM.

in the TT direction for the GHP. The samples of virgin ZURAM were only submitted to temperatures up to $473.15\,\mathrm{K}$ to avoid thermal decomposition.

Three steps were required to artificially generate this multiphase material, as seen in Section 4.4. The same domain of 410^3 vx was used.

The first idea consisted in generating the CALCARB geometry according to the parameters defined in 4.1.1. Afterwards, a uniformly distributed spherical material was generated. Since the spheres illustrate the testing gas trapped inside the material, the needed inputs are the volume fraction of the spheres, the bulk porosity and the diameter of the spheres. The latest will be inputted to achieve the target volume fraction. In this case, porosity corresponds to the volume fraction of the resin because the medium represents the phenolic resin, and the volume fraction of spheres is equal to the volume fraction of helium. Pycnometry provides the volume fraction of virgin ZURAM as 0.2420. Since the volume fraction of the preform is equal to 0.11, it is possible to determine the volume fraction of resin to have a value of 0.1328. By having the volume fraction of resin and fibers and knowing that in a material the sum of all volume fractions is equal to 1, it is possible to calculate the volume fraction of gas as being 0.7572.

The final step combined the two materials into a single domain. Then, the volume fractions of the fibers, resin and gas were retrieved to assess if the previous values given by picnometry were accomplished. The results are presented in Table 5.2.

Table 5.2: Comparison between the volume fractions measured and simulated for virgin ZURAM and error associated. Case for spheres generation.

	Measured (-)	Simulated (-)	Error (%)
Volume fraction gas	0.7572	0.6738	11
Volume fraction fibers	0.11	0.1099	0.1
Volume fraction resin	0.1328	0.2162	62.8

From the results, it is possible to infer that the minimum diameter allowed for spheres is not physically representative of the real material. Besides that, it is not possible to achieve the desired volume fraction. The simulated volume fraction is very low compared to the one given by pycnometry. Therefore, to increase it, a higher amount of gas is required.

The solution found was to generate, instead of the spheres, a cloud of uniformly distributed voxels in the domain to simulate the trapped gas, as depicted in Section 4.4. For this generation, the values fixed for porosity correspond to the volume fraction of resin, whereas the volume fraction of the voxels is equal to the gas. To apprehend if, at the end of the combination of the two generations, the volume fractions of the three phases (fibers, resin and gas) retrieved are in accordance with the pyconometry data, Table 5.3 was assembled.

Table 5.3: Comparison between the volume fractions measured and simulated for virgin ZURAM and error associated. Case for voxels generation.

	Measured (-)	Simulated (-)	Error (%)
Volume fraction gas	0.7572	0.6737	11.03
Volume fraction fibers	0.11	0.1099	0.1
Volume fraction resin	0.1328	0.2163	62.8

Even though this implementation is more accurate when portraying virgin ZURAM, the retrieved volume fraction of the gas (voxels) remains significantly small. This can be explained by the overlapping of the material in which parts will be removed. Therefore, to overcome this problem, when generating the voxels (gas), the volume fraction inputted for the generation should be higher to consider this overlap. To achieve the most possible approximation of desired gas volume fraction (0.7572), a value equal to 0.85 was inputted. Table 5.4 presents the volume fractions accomplished for each phase of the material.

Table 5.4: Comparison between the volume fractions measured and simulated for virgin ZURAM and error associated. Case for the volume fraction of the gas equal to 0.85.

	Measured (-)	Simulated (-)	Error (%)
Volume fraction gas	0.7572	0.7564	0.11
Volume fraction fibers	0.11	0.1099	0.1
Volume fraction resin	0.1328	0.1337	0.67

For the conductivity simulations, a new problem arises. The measurements were conducted in a temperature range between $293\,\mathrm{K}$ and $473\,\mathrm{K}$. However, the lower temperature of the data available for the intrinsic thermal conductivity of the fibers pre-heated at HTT = $2500\,\mathrm{K}$ from Pradere [44] is $846\,\mathrm{K}$. From Figure 2.11, it is seen that between $800\,\mathrm{K}$ and $1400\,\mathrm{K}$ the thermal conductivity behaves linearly. A linear regression was used to extrapolate the intrinsic thermal conductivity that meets each of the temperatures of the measurements. The intrinsic conductivity of helium for the corresponding temperatures was determined using Mutation++ [43].

Moreover, it is also required to know the thermal conductivity of the resin, despite the manufacturer not furnishing it. From the data available, it is possible to conclude that the conductivity of the resin should be in the same or lower order as the gas. In order to find the best value that suits to reproduce the available experimental results, it was decided to survey the effect of resin conductivity. Two values for the resin conductivity were selected to perform the simulations. These values are 0.1 and $0.001\,\mathrm{W\,m^{-1}\,K^{-1}}$. Once all necessary initial parameters have been established and selected, the simulations are executed, and their outcomes are presented in Figure 5.3.

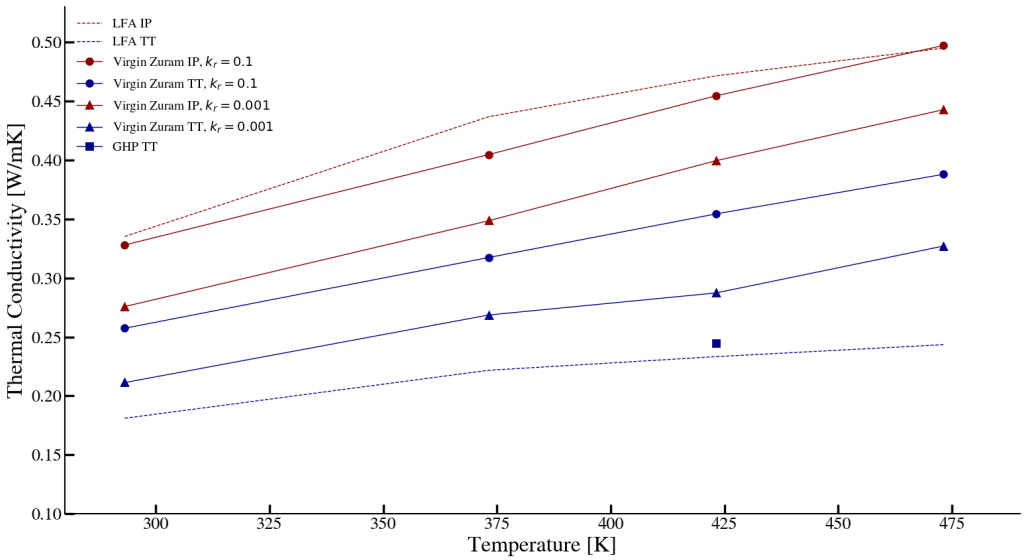

Figure 5.3: Comparison between the simulations from PuMA and the experiments on LFA (dashed lines) for both porosity of 0.1 and 0.001 for virgin ZURAM material.

Even though it can be seen that the simulated and measured results have similar behaviours, the disparity can reside in the fact that the resin's and the fibers' intrinsic conductivity at the experiments' temperature are unknown, which can lead to an error in the output of the effective thermal conductivity simulations. The geometry of the virgin ma-

terial can also not be the most appropriate since the reproduction of the gas inside the material continues to maintain a considerable size.

5.3 Assessing the effect of graphitization

From the experimental data of charred ZURAM presented in Figure 5.1, it is possible to infer that when the material is subjected to temperatures that start to exceed the HTT of CALCARB CBCF 18-2000 (2273 K) there is an increase of the measured effective thermal conductivity. Besides that, from Figure 5.4, it is possible to verify that the effective conductivity increases during the cooldown measurements. From the literature, this occurrence is due to the graphitization process, as previously explained in Section 2.4.

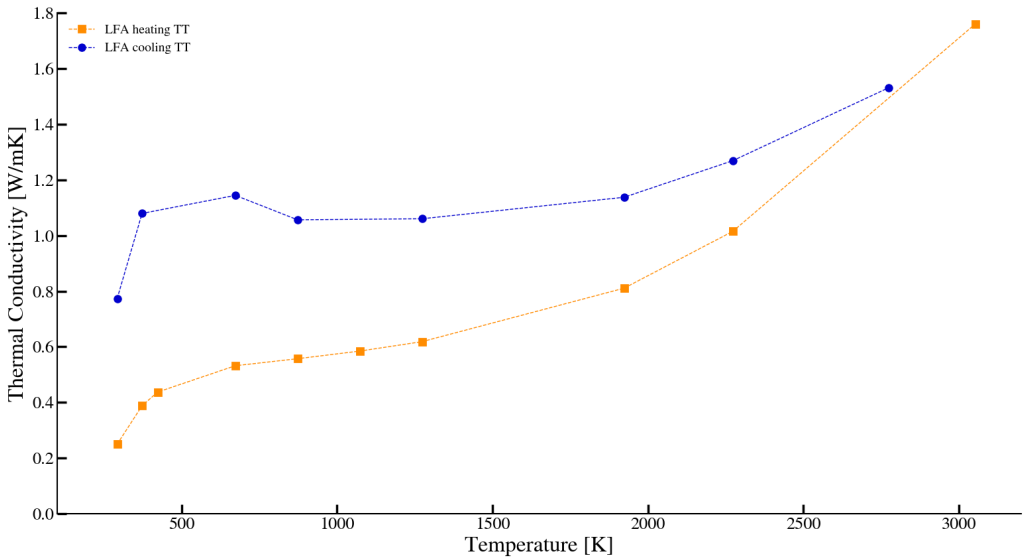

Figure 5.4: The behaviour of the effective thermal conductivity through the heating and cooling process in the TT plane on charred ZURAM.

This phenomenon is very significant for atmospheric entry, where such high temperatures are frequently encountered. Therefore, it should be carefully addressed and studied. Since the assumption of this process relies on the fact that the re-arrangement of the fibers leads to an increase of their intrinsic conductivities, the objective of this section is to compute the intrinsic conductivity.

By a reverse-engineering process, knowing that the effective thermal conductivity from the LFA measurements is equal to the sum of the intrinsic conductivity of the fibers and testing gas (helium), it is possible to assess the intrinsic conductivity behaviour. By means

of simulation in PuMA, taking into account that only thermal conductivity measurements for the TT plane were provided for the cooling process, the intrinsic conductivity of the fibers is manually inputted in order to achieve to the desired effective conductivity.

The simulation results showed an increase in the intrinsic conductivity of the fibers after the cooldown process, agreeing with the predicted values published by Pradere [44] of the rise in thermal conductivity for a single fiber. Even though these simulations study graphitization in a very simplified way, the increase is not negligible. Thus, it should be further developed.

Chapter 6

Conclusions and future work

6.1 Conclusions

By addressing the objectives set out in Section 1.2, this thesis evaluated how the microstructure and intrinsic properties of carbon fiber felts affect their effective thermal conductivity. Besides that, it contributed to the enhancement of numerical simulators to reproduce and predict the phenomena and behaviour of ablative heat shield materials during atmospheric entry. This chapter presents the summarized results and conclusions obtained throughout the project as well as recommendations for future work.

The primary conclusion retrieved from this thesis is that the use of numerical software, such as PuMA, allows an accurate characterisation and modelling of ablative materials. Hence, they are a very important tool and should be in constant development to improve their performance and promote a more effective design of the TPS. The results presented are structured by the objectives previously assigned in Section 1.2.

Objective 1. To approach the problem, a numerical model for CALCARB 18-2000, the carbon preform of the material in the study, ZURAM, was development by artificially generating a transversely isotropic material with a normal distribution in the TT and a uniform distribution in the IP direction. Later, this code was compared with available experimental data as a validation. It was seen that in fact, there is a good agreement between the effective conductivity values obtained experimentally and computationally. A REV analysis was performed to determine the minimal representative size possible to assume, minimising computational resources. For an argon environment, size of 600 vx was the largest domain size feasible to be generated, whereas for a helium environment a domain size of 410 vx was selected. Based on these results, it was possible to conclude that increasing the intrinsic medium conductivity has a positive effect on the reduction of the REV while increasing the temperature has the opposite effect. This can be explained by the ratio between the medium and fiber conductivity. When the ratio tends to a value closer to 1 the REV converges faster since the domain becomes more homogeneous. After-

wards, a general parametric study was conducted to evaluate the impact of microscopical parameters on thermal conductivity, such as porosity, fiber length and diameter and angular variation of the fiber orientation on the synthetic model previously developed. This analysis consisted in evaluating three cases: the influence of porosity and fibers' orientation, the influence of length and fibers' orientation and the influence of radius and fibers' orientation on the effective thermal conductivity. From this study, it was concluded that the IP plane's effective thermal conductivity is more affected by porosity than by the angular variation of the fibers and the contrary occurs in the TT plane. Increasing the porosity decreases the effective thermal conductivity regardless of the direction, since there is a reduction in the number of fibers and the medium is less conductive than the fibers. Besides that, the IP direction is less sensitive to the angle variation. Additionally, it can be seen that a reduction of the influence on the angle variation of the fibers is obtained while increasing the porosity. Increasing the length leads to a higher possibility of intersection between fibers, which results in higher heat transferred and, consequently, in an increase in the effective thermal conductivity. The radius has opposite behaviour compared to the length. Finally, to quantify how porosity, angle variation and length influence the overall performance of a real porous material, a sensitivity analysis based on a surrogate model was executed. The outcomes of this analysis follow the parametric study. It also allowed to infer about the contribution of the interaction of two input parameters on the thermal conductivity as there is no information in the literature. Porosity and angle were found to have a higher influence over the final output.

Objective 2. To study the effect of thermal conductivity on charred and virgin ZURAM, two material models were generated. First, a geometry generator for the material in the charred state that creates a uniform coating on top of the fiber by generating a coaxial cylinder was developed. Secondly, to mimic the virgin material, fibers, gas and phenolic resin must be taken into account when developing the artificial model. It combines the code for the carbon fiber preform with a generation of uniformly distributed voxels in a phenolic resin medium, where the former simulates the gas trapped inside the material. Both models were verified by the execution of test cases.

Objective 3. From the analysis of the charred state material, it is feasible to retrieve that the addition of the char decreases the bulk porosity of the material. Moreover, the effective thermal conductivity is affected by it and this is why it was necessary to implement a new material model. From the comparison of the simulated and experimental results,

it can be inferred that the simulated effective conductivity is still very high compared to the experimental one. Even though the volume fraction for each phase of the material measured by pycnometry was achieved during the material generation, the fact that the char conductivity is unknown and that the overall synthetic material might not reproduce exactly the real material has an impact on the final results. Despite the fact that there is a tendency observed between both outcomes, simulated and experimental, this requires further investigation. The results of the artificial generator of the virgin ZURAM material are more difficult to interpret. The disparity between the results can be explained by the lack of information about the resin conductivity and the fiber intrinsic conductivity at such lower temperatures. The behaviour of both results is similar however, the simulated results for both plane directions are lower.

Objective 4. The increase of intrinsic thermal conductivity of the carbon fibers and, consequently increase of the effective one improve heat transport to the material's interior. This can jeopardise the material substructure or lead to inaccurate assumptions of how the material would react. This impact should be taken into regard during the TPS design and especially if the reusability of this material is being considered.

6.2 Recommendations for future work

This thesis, in terms of characterization of thermal response of carbon/phenolic TPS submitted to high temperatures, provided improved knowledge and innovative approaches, especially in terms of material model development. However, much work remains to be improved for further developments:

- Improving the artificially generated material models. These models are still very simple and require an adjustment of the assumptions to consider a more realistic physical geometry. From SEM images it is possible to observe that fibers are stacked together as clusters. Therefore, this should be included in the model of the preform material. For the charred state model, a new code should be developed to make fibers not be completely covered by the char but the char be randomly dispersed in spherical forms on top of the fibers. In the virgin artificial generator material, the assumptions of voxels as the gas trapped inside need further verification and improvement by reducing its size.

- Assessing the charred and virgin resin conductivities with experimental measurements.
- Evaluating the rayon fibers' intrinsic thermal conductivity. The extrapolation of this property at temperatures not referred to in the literature should be carefully evaluated and validated.
- Modelling the radiative transfer within the pores. Even though this was out of the scope of the current work, accounting for the impact of radiative heat inside the porous material becomes relevant at high temperatures and influences effective thermal conductivity. This would require extensive development. This could be achieved by implementing an additional solver in PuMA. Additionally, it could be added as a contribution component as a function of the temperature.
- Tailoring pores sizes. Previous studies [78] have shown that porosity promotes radiation scattering and consequently decreases the radiative contribution to the thermal conductivity of the porous material at such temperature. As a consequence, a study should be conducted to evaluate the effect of different pores sizes on the effective thermal conductivity. The possibility of adding the option to input pore sizes on the material models developed should be investigated.

Bibliography

[1] M. José, P.-G. Isabel, and S.-A. Angel, *Spacecraft Thermal Control*. Woodhead Publishing, 2016.

[2] Torres Herrador, Francisco José, Ph.D. dissertation, VKI, title = Thermal response of carbon composites submitted to high temperatures : application to atmospheric entry, year = 2022,.

[3] B. Laub and E. Venkatapathy, "Thermal protection system technology and facility needs for demanding future planetary missions," in *Planetary Probe Atmospheric Entry and Descent Trajectory Analysis and Science*, ser. ESA Special Publication, A. Wilson, Ed., vol. 544, 2004, pp. 239–247.

[4] S. Löhle, T. Hermann, and F. Zander, "Experimental assessment of the performance of ablative heat shield materials from plasma wind tunnel testing," *CEAS Space Journal*, vol. 10, 2017.

[5] H. K. Tran, C. E. Johnson, D. J. Rasky, F. Y. C. Hui, M. ta Hsu, T. S. Chen, Y.-K. Chen, D. Paragas, and L. Kobayashi, "Phenolic impregnated carbon ablators (PICA) as thermal protection systems for discovery missions," 1997.

[6] T. Reimer, C. Zuber, J. Rieser, and T. Rothermel, "Determination of the mechanical properties of the lightweight material zuram," 2016.

[7] M. Stackpoole, S. Sepka, I. Cozmuta, and D. Kontinos, "Post-flight evaluation of stardust sample return capsule forebody heatshield material," 2008.

[8] K. Edquist, B. Hollis, C. Johnston, D. Bose, T. White, and M. Mahzari, "Mars science laboratory heat shield aerothermodynamics: Design and reconstruction," *Journal of Spacecraft and Rockets*, vol. 51, pp. 1106–1124, 2014.

[9] "Mars 2020 thermal protection systems (TPS) - nasa technical reports server (ntrs)."

[10] M. Stackpoole, G. Gonzales, V. Qu, and D. Kao, "Post-flight evaluation of PICA & PICA-X - comparisons of the stardust SRC & Space-X Dragon forebody heatshield materials."

[11] M. Rivier, J. Lachaud, and P. Congedo, "Ablative thermal protection system under uncertainties including pyrolysis gas composition," *Aerospace Science and Technology*, vol. 84, pp. 1059–1069, 2019.

[12] J. Rico-Orero, "Computational study on the effect of the microstructure on macroscopic properties for carbon fiber felts," Master's thesis, von Karman Institute for Fluid Dynamics, 2020.

[13] J. C. Ferguson, F. Panerai, A. Borner, and N. N. Mansour, "Puma: The porous microstructure analysis software," *SoftwareX*, vol. 7, pp. 81–87, 2018.

[14] J. C. Ferguson, F. Semeraro, J. M. Thornton, F. Panerai, A. Borner, and N. N. Mansour, "Update 3.0 to puma: The porous microstructure analysis software," *SoftwareX*, vol. 15, p. 100775, 2021.

[15] B. Helber, C. O. Asma, Y. Babou, A. Hubin, O. Chazot, and T. E. Magin, "Material response characterization of a low-density carbon composite ablator in high-enthalpy plasma flows," *Journal of Materials Science*, vol. 49, pp. 4530–4543, 2014.

[16] B. Helber, A. Turchi, J. Scoggins, A. Hubin, and T. Magin, "Experimental investigation of ablation and pyrolysis processes of carbon-phenolic ablators in atmospheric entry plasmas," *International Journal of Heat and Mass Transfer*, vol. 100, pp. 810–824, 2016.

[17] A. Riccio, F. Raimondo, A. Sellitto, V. Carandente, R. Scigliano, and D. Tescione, "Optimum design of ablative thermal protection systems for atmospheric entry vehicles," *Applied Thermal Engineering*, vol. 119, p. 541–552, 2017.

[18] A. Turchi, F. Torres Herrador, B. Helber, G. Pintsuk, C. Zuber, H. Ritter, and T. Magin, "Thermal conductivity evolution of carbon-fiber ablators submitted to high temperatures," *Journal of Thermophysics and Heat Transfer*, pp. 1–11, 2022.

[19] G. Pulci, J. Tirillò, F. Marra, F. Fossati, C. Bartuli, and T. Valente, "Carbon-phenolic ablative materials for re-entry space vehicles: Manufacturing and properties," *Composites Part A: Applied Science and Manufacturing*, vol. 41, pp. 1483–1490, 2010.

[20] B. Laub and E. Venkatapathy, "Thermal protection system technology and facility needs for demanding future planetary missions," vol. 544, pp. 239–247, 2004.

[21] Daniele Bianchi, "Modeling of ablation phenomena in space applications," Ph.D. dissertation, Università degli Studi di Roma, 2007.

[22] G. Duffa, *Ablative Thermal Protection Systems Modeling*, 2013.

[23] J. Lundell, R. Wakefield, and J. Jones, "Experimental investigation of a charring ablative material exposed to combined convective and radiative heating in oxidizing and nonoxidizing environments," *Entry Technology Conference*, 1964.

[24] J. T. Culp, "Chapter 5 - flexible solid sorbents for co2 capture and separation," in *Novel Materials for Carbon Dioxide Mitigation Technology*, F. Shi and B. Morreale, Eds. Elsevier, 2015, pp. 149–176.

[25] J. Rouquerol, C. Fairbridge, D. Everett, J. Haynes, N. Pernicone, J. Ramsay, K. Sing, and K. Unger, "Recommendations for the characterization of porous solids," *Pure and Applied Chemistry*, vol. 66, pp. 1739–, 1994.

[26] "Experimental measurements of the permeability of fibrous carbon at high-temperature," *International Journal of Heat and Mass Transfer*, vol. 101, pp. 267–273, 2016.

[27] S. Van Vlierberghe, G.-J. Graulus, S. Keshari Samal, I. Van Nieuwenhove, and P. Dubruel, "12 - porous hydrogel biomedical foam scaffolds for tissue repair," in *Biomedical Foams for Tissue Engineering Applications*, P. A. Netti, Ed. Woodhead Publishing, 2014, pp. 335–390.

[28] E. N. Landis and D. T. Keane, "X-ray microtomography," *Materials Characterization*, vol. 61, no. 12, pp. 1305–1316, 2010.

[29] P. A. García-Salaberri, I. V. Zenyuk, A. D. Shum, G. Hwang, M. Vera, A. Z. Weber, and J. T. Gostick, "Analysis of representative elementary volume and through-plane regional characteristics of carbon-fiber papers: diffusivity, permeability and electrical/thermal conductivity," *International Journal of Heat and Mass Transfer*, vol. 127, pp. 687–703, 2018.

[30] M. Zhang, "Multiscale lattice boltzmann-finite element modelling of transport properties in cement-based materials," Ph.D. dissertation, 2013.

[31] T. L. Bergman, A. Lavine, and F. P. Incropera, *Fundamentals of heat and mass transfer*. John Wiley amp; Sons, Inc., 2019.

[32] D. Smith, A. Alzina, J. Bourret, B. Nait-Ali, F. Pennec, N. Tessier-Doyen, K. Otsu, H. Matsubara, P. Elser, and U. Gonzenbach, "Thermal conductivity of porous materials," *Journal of Materials Research*, vol. 28, 2013.

[33] I. Sumirat, Y. Ando, and S. Shimamura, “Theoretical consideration of the effect of porosity on thermal conductivity of porous materials,” *Journal of Porous Materials*, vol. 13, pp. 439–443, 2006.

[34] B. Helber, F. Torres Herrador, A. Turchi, T. Magin, O. Chazot, A. Denis, C. Zuber, T. Reimer, G. Pintsuk, G. Pinaud, P. Congedo, F. Hemberger, and D. Girolamo, “RECHAR: Assessment of reliable material characterisation methods for charring ablators,” 2022.

[35] Y.-H. Zhao, Z.-K. Wu, and S.-L. Bai, “Thermal resistance measurement of 3d graphene foam/polymer composite by laser flash analysis,” *International Journal of Heat and Mass Transfer*, vol. 101, pp. 470–475, 2016.

[36] W. J. Parker, R. J. Jenkins, C. P. Butler, and G. L. Abbott, “Flash method of determining thermal diffusivity, heat capacity, and thermal conductivity,” *Journal of Applied Physics*, vol. 32, no. 9, p. 1679–1684, 1961.

[37] J. B. Henderson, Y. P. Verma, M. R. Tant, and G. R. Moore, *Measurement of the thermal conductivity of polymer composites to high temperatures using the line source technique*, 1983, vol. 4, no. 4.

[38] “The guarded hot plate method is a steady state method,” 2020.

[39] A. Alhawari and P. Mukhopadhyaya, “Construction and calibration of a unique hot box apparatus,” *Energies*, vol. 15, no. 13, 2022.

[40] M. Loretz, E. Maire, and D. Baillis, “Analytical modelling of the radiative properties of metallic foams: Contribution of tomography,” *Advanced Engineering Materials*, vol. 10, pp. 352 – 360, 2008.

[41] Mersen, “Properties of calcarb, rigid carbon insulation CBCF 18-2000,” Mersen, Tech. Rep., February 2009.

[42] ——, “Calcarb rigid carbon insulation,” Mersen, Tech. Rep., February 2013.

[43] J. B. Scoggins, V. Leroy, G. Bellas-Chatzigeorgis, B. Dias, and T. E. Magin, “Mutation++: Multicomponent thermodynamic and transport properties for ionized gases,” *SoftwareX*, vol. 12, 2020.

[44] C. Pradere, J. Batsale, J. Goyhénèche, R. Pailler, and S. Dilhaire, “Thermal properties of carbon fibers at very high temperature,” *Carbon*, vol. 47, no. 3, pp. 737–743, 2009.

[45] H. Marsh and F. Rodríguez-Reinoso, “Chapter 9 - production and reference material,” in *Activated Carbon*, H. Marsh and F. Rodríguez-Reinoso, Eds. Oxford: Elsevier Science Ltd, 2006, pp. 454–508.

[46] F. Torres Herrador, S. Tovey, B. Helber, A. Turchi, J. Blondeau, K. Van Geem, and T. Magin, “Investigating the Graphitization of Carbon and its Effect by Means of Multi-Scale Numerical Simulations,” in *2nd International Conference on Flight Vehicles, Aerothermodynamics and Re-entry Missions & Engineering (FAR)*. Heilbronn, Germany: ESA, 2022.

[47] A. Gupta, S. R. Dhakate, P. Pal, A. Dey, P. K. Iyer, and D. K. Singh, “Effect of graphitization temperature on structure and electrical conductivity of poly-acrylonitrile based carbon fibers,” *Diamond and Related Materials*, vol. 78, pp. 31–38, 2017.

[48] X. Qin, Y. Lu, H. Xiao, Y. Wen, and T. Yu, “A comparison of the effect of graphitization on microstructures and properties of polyacrylonitrile and mesophase pitch-based carbon fibers,” *Carbon*, vol. 50, no. 12, pp. 4459–4469, 2012.

[49] J. Lachaud and N. Mansour, “Porous-material analysis toolbox based on openfoam-extend and applications,” *44th AIAA Thermophysics Conference*, 2013.

[50] E. Maire, J.-y. Buffiere, L. Salvo, J. Blandin, W. Ludwig, and J. Létang, “On the application of x-ray microtomography in the field of materials science,” *Advanced Engineering Materials*, vol. 3, pp. 539 – 546, 2001.

[51] C. Arns, M. Knackstedt, M. Pinczewski, and W. Lindquist, “Accurate estimation of transport properties from microtomographic images,” *Geophysical Research Letters*, vol. 28, pp. 3361–3364, 2001.

[52] “Geodict software.” [Online]. Available: https://www.geodict.com/geodict-software/geodict-base-modules.html

[53] “Avizo software extensions.” [Online]. Available: https://www.thermofisher.com/be/en/home/industrial/electron-microscopy/electron-microscopy-instruments-workflow-solutions/3d-visualization-analysis-software/avizo-software-extensions.html

[54] “3d image processing solutions - simpleware.” [Online]. Available: https://www.synopsys.com/simpleware.html

[55] S. Cooper, A. Bertei, P. Shearing, J. Kilner, and N. Brandon, "Taufactor: An open-source application for calculating tortuosity factors from tomographic data," *SoftwareX*, vol. 5, pp. 203–210, 2016.

[56] "Imorph software." [Online]. Available: https://imorph.sourceforge.net/

[57] G. Melenka, "Digital volume correlation analysis of braided composites," 2018.

[58] F. Girault, "Uncertainty characterization of ablative materials for atmospheric reentry of spacecrafts using puma," Master's thesis, Institut Polytechnique de Paris, 2021.

[59] M. Rivier, J. Lachaud, and P. Congedo, "Ablative thermal protection system under uncertainties including pyrolysis gas composition," *Aerospace Science and Technology*, vol. 84, 2018.

[60] "Front matter," in *Porous Materials*, P. Liu and G. Chen, Eds. Boston: Butterworth-Heinemann, 2014.

[61] W. E. Lorensen and H. E. Cline, "Marching cubes: A high resolution 3d surface construction algorithm," *SIGGRAPH Comput. Graph.*, vol. 21, no. 4, p. 163–169, 1987.

[62] G. Treece, R. Prager, and A. Gee, "Regularised marching tetrahedra: improved iso-surface extraction," *Computers Graphics*, vol. 23, no. 4, pp. 583–598, 1999.

[63] X. Wang, S. Gao, M. Wang, and Z. Duan, "A marching cube algorithm based on edge growth," *Virtual Reality Intelligent Hardware*, vol. 3, no. 4, pp. 336–349, 2021.

[64] F. Semeraro, J. C. Ferguson, F. Panerai, R. J. King, and N. N. Mansour, "Anisotropic analysis of fibrous and woven materials part 1: Estimation of local orientation," *Computational Materials Science*, vol. 178, p. 109631, 2020.

[65] F. Semeraro, J. C. Ferguson, M. Acin, F. Panerai, and N. N. Mansour, "Anisotropic analysis of fibrous and woven materials part 2: Computation of effective conductivity," *Computational Materials Science*, vol. 186, p. 109956, 2021.

[66] "Finite volume methods for elasticity with weak symmetry," *International Journal for Numerical Methods in Engineering*, vol. 112, no. 8, 2017.

[67] A. Wiegmann and A. Zemitis, "Ej-heat: A fast explicit jump harmonic averaging solver for the effective heat conductivity of composite materials," *Berichte des Fraunhofer ITWM*, vol. 94, 2006.

[68] H. A. van der Vorst, "Bi-cgstab: A fast and smoothly converging variant of bi-cg for the solution of nonsymmetric linear systems," *Journal on Scientific and Statistical Computing*, vol. 13, no. 2, pp. 631–644, 1992.

[69] G. Matheron, "Principles of geostatistics," *Economic Geology*, vol. 58, no. 8, pp. 1246–1266, 1963.

[70] D. Krige, "A statistical approach to some basic mine valuation problems on the witwatersrand," *Journal of the Southern African Institute of Mining and Metallurgy*, vol. 52, no. 6, pp. 119–139, 1951.

[71] B. Helber, O. Chazot, A. Hubin, and T. E. Magin, "Microstructure and gas-surface interaction studies of a low-density carbon-bonded carbon fiber composite in atmospheric entry plasmas," *Composites Part A: Applied Science and Manufacturing*, vol. 72, pp. 96–107, 2015.

[72] C. Schneider, W. Rasband, and K. Eliceiri, "Nih image to imagej: 25 years of image analysis," *Nature Methods*, vol. 9, 2012.

[73] F. Panerai, J. D. White, T. J. Cochell, O. M. Schroeder, N. N. Mansour, M. J. Wright, and A. Martin, "Experimental measurements of the permeability of fibrous carbon at high-temperature," *International Journal of Heat and Mass Transfer*, vol. 101, pp. 267–273, 2016.

[74] J. Herman and W. Usher, "SALib: An open-source python library for sensitivity analysis," *The Journal of Open Source Software*, vol. 2, no. 9, 2017.

[75] T. Iwanaga, W. Usher, and J. Herman, "Toward SALib 2.0: Advancing the accessibility and interpretability of global sensitivity analyses," *Socio-Environmental Systems Modelling*, vol. 4, p. 18155, 2022.

[76] M. A. Bouhlel, J. T. Hwang, N. Bartoli, R. Lafage, J. Morlier, and J. R. R. A. Martins, "A python surrogate modeling framework with derivatives," *Advances in Engineering Software*, p. 102662, 2019.

[77] J. F. L. W. A. Clayton, T. J. Fabish, "Thermal conductivity of phenolic carbon chars," Boeing Co Seattle Wa Aerospace Systems Division, Tech. Rep., December 1969.

[78] E. Poloni, F. Bouville, A. L. Schmid, P. I. Pelissari, V. C. Pandolfelli, M. L. Sousa, E. Tervoort, G. Christidis, V. Shklover, J. Leuthold, and A. R. Studart, "Carbon ab-

lators with porosity tailored for aerospace thermal protection during atmospheric re-entry," *Carbon*, vol. 195, pp. 80–91, 2022.

[79] M. Wolverton, "Piercing the plasma," *Scientific American*, vol. 301, p. 28–30, 2009.

[80] J. Lachaud and G. Vignoles, "A brownian motion technique to simulate gasification and its application to c/c composite ablation," *Computational Materials Science*, vol. 44, no. 4, pp. 1034–1041, 2009.

[81] J. Lachaud, I. Cozmuta, N. Mansour, G. Vignoles, Y. Aspa, I. Boyd, R. Moser, and M. Marchetti, "Multiscale approach to ablation modeling of phenolic impregnated carbon ablators," *Journal of Spacecraft and Rockets*, vol. 47, pp. 910–921, 2010.

[82] W. E. Lorensen and H. E. Cline, "Marching cubes: A high resolution 3d surface construction algorithm." New York, NY, USA: Association for Computing Machinery, 1987, p. 163–169.

[83] F. Semeraro, J. C. Ferguson, F. Panerai, R. J. King, and N. N. Mansour, "Anisotropic analysis of fibrous and woven materials part 1: Estimation of local orientation," *Computational Materials Science*, vol. 178, p. 109631, 2020.

[84] J. C. Ferguson, A. Borner, F. Panerai, S. Close, and N. N. Mansour, "Continuum to rarefied diffusive tortuosity factors in porous media from x-ray microtomography," *Computational Materials Science*, vol. 203, p. 111030, 2022.

[85] "Tortuosity of porous media: Image analysis and physical simulation," *Earth-Science Reviews*, vol. 212, p. 103439, 2021.

[86] P. Adler, *Porous media: Geometry and transports*. Butterworth-Heinemann, 1992.

[87] F. Usseglio-Viretta, P. Patel, E. Bernhardt, A. Mistry, P. Mukherjee, J. Allen, S. Cooper, J. Laurencin, and K. Smith, "Matbox: An open-source microstructure analysis toolbox for microstructure generation, segmentation, characterization, visualization, correlation, and meshing," *SoftwareX*, vol. 17, p. 100915, 2022.

[88] R. Fu, H. Weng, J. Wenk, and A. Martin, "Thermal expansion for charring ablative materials," *Journal of Thermophysics and Heat Transfer*, vol. 34, pp. 1–9, 2019.

[89] M. Hestenes and E. Stiefel, "Methods of conjugate gradients for solving linear systems," *Journal of Research of the National Bureau of Standards*, vol. 49, no. 6, 1952.

[90] S. Löhle, T. Stäbler, T. Reimer, and A. Cefalu, “Photogrammetric surface analysis of ablation processes in high-enthalpy air plasma flow,” *AIAA Journal*, vol. 53, 2015.

[91] C. Cercignani and M. Lampis, “Kinetic models for gas-surface interactions,” *Transport Theory and Statistical Physics*, vol. 1, no. 2, pp. 101–114, 1971.

[92] O., Joshi, “Fluid-structure thermal coupling and ablation effects in atmospheric entry,” Ph.D. dissertation, École polytechnique fédérale de Lausanne, 2014.

Appendix A

PuMA effective material properties

A.1 Tortuosity

The tortuosity factor, η, is a material property that quantifies the material´s approximate resistance to a diffusive flux, which is a significant component when modelling flows in porous microstructures at the macroscale [84]. However, the concept of this property can have multiple definitions and be incorrectly understood depending on the context. For the same porous media, distinct evaluations can be found for the geometrical and physical tortuosities, leaning on the specific assessment and the evaluation method adopted. This makes it controvertible to directly use the geometrical as a replacement for physical tortuosity, a standard practice in the literature. Geometric tortuosity is defined as the ratio of the shortest path through a porous medium to the straight-line path [85, 86].

The Knudsen number, Kn, which is commonly defined as the ratio of the flow mean free path length to a given length scale of the porous domain, l_{D}, as according to equation A.1, must be addressed when modelling diffusion in porous media to establish if the continuum assumption is valid at the length scale of concern.

$$\mathrm{Kn} = \frac{\bar{\lambda}}{l_{\mathrm{D}}} \quad \text{(A.1)}$$

From equation A.2 it is possible to determine the tortuosity factor that is defined for each direction, since not all of the materials are necessarily isotropic

$$\eta = \varepsilon \frac{D_{\mathrm{ref}}}{D_{\mathrm{eff}}} \quad \text{(A.2)}$$

where D_{ref} is the reference diffusion coefficient, D_{eff} is the effective diffusion coefficient in the porous material, and ε is the porosity. Applying the Bosanquet approximation to single-species diffusion in a capillary direction, D_{ref} can be expressed as in equation A.1,

$$D_{\mathrm{ref}} = \frac{1}{3}\bar{v}\left(\frac{\bar{\lambda} l_{\mathrm{D}}}{\bar{\lambda} + l_{\mathrm{D}}}\right) \quad \text{(A.3)}$$

where $\bar{v}$ is the mean thermal velocity and $\bar{\lambda}$ the mean free path of the gas. In the continuum regime Kn is lower than 1, which implies that the reference diffusion coefficient can be simply defined as the single-species bulk diffusion coefficient [84] as depicted in equation A.4.

$$D_{\mathrm{ref}} = D_{\mathrm{bulk}} \approx \frac{1}{3}\bar{v}\bar{\lambda} \quad \text{(A.4)}$$

After, the tortuosity factor can be calculated by computing D_{eff} and solving η in equation A.2. For the non-continuum regime equation A.1 needs o be used . In PuMA, the length scale of interest specified by the term l_{D} is a geometric property and not a function of the Kn. For that reason, the characteristic length l_{D} in each direction must be estimated in high Kn by equation A.5,

$$\frac{1}{l_{\mathrm{D}}} = \frac{\bar{v}}{3\eta D_{\mathrm{eff}}} - \frac{1}{\bar{\lambda}} \quad \text{(A.5)}$$

where η is the bulk tortuosity factor computed using continuum assumptions, D_{eff} is the computed effective diffusion coefficient of the high Knudsen number simulation, $\bar{v}$ is the mean thermal velocity and $\bar{\lambda}$ is the mean free path.

PuMA allows for the computation of bulk tortuosity factors of continuum and non-continuum regimes using finite difference and random walk method. To calculate the tortuosity factor by equation A.2, it is first necessary to determine D_{ref}, D_{eff} and ε. To do so, the first step is to solve the steady-state diffusion equation A.6,

$$\nabla \cdot (D_{\mathrm{ref}} \nabla \phi) = 0 \quad \text{(A.6)}$$

where D_{ref} is the local diffusion coefficient and ϕ the local concentration and can be solved in PuMA in three different ways. For low Kn, both finite element methods and random walk method can be utilised, and for high Kn in rarefied and transitional regimes can only be employed the random walk method. Two finite difference methods are incorporated into the software, the Finite Difference (FD) and the Explicit-Jump Finite Difference method (EJFD). For both, the solver imposes a concentration gradient at the boundaries in the direction of interest until the concentration field converges to a steady-state. Then, the average diffusion flux can be computed, and from Fick´s first law of diffusion, equation A.7, the effective diffusion coefficient, D_{eff}, can be determined and used in equation

A.2 to retrieve the tortuosity factor.

$$\mathcal{F} = -D_{\text{eff}} \nabla \langle \phi \rangle \quad \text{(A.7)}$$

Both finite methods should give similar results. The only difference is regarding the boundary condition in the simulation direction. In the FD, it is possible to choose from either periodic or reflective boundary conditions in the side direction, and in the simulation direction uses Dirichlet boundary conditions, while in the EJFD in all the directions, the boundary condition are periodic [67]. Nevertheless, the latter method is faster and uses Fast Fourier Transformers (FFT) to accelerate the solution.

The random walk method implemented [13] can solve, for any Kn, the value of the effective diffusion coefficient, D_{eff}. Instead of continuum-based solvers, this method uses particles placed inside the domain's void space and diffused randomly through the material. Whenever collisions occur with the surface, they are treated as fully diffusive. Reflective boundary conditions are used. Once the simulation has converged, D_{eff}, is determined as presented in equation A.8,

$$D_{\text{eff}} = \frac{\langle \xi^2 \rangle}{2t} \quad \text{(A.8)}$$

where $\langle \xi^2 \rangle$ is the mean square displacement of the particles in the direction of interest, and t is the simulation time. At last, this value, along with the mean free path, $\bar{\lambda}$, can be used in equation A.5 to calculate the characteristic length to after compute D_{ref} from equation A.1.

A.2 Electrical conductivity

The effective electrical conductivity is determined in the same way as described for the effective thermal conductivity in Section 3.2. The steady-state equation for electrical conduction, defined by A.9 where V denotes the local voltage potential, can be solved, by PuMA, in three different ways.

$$\nabla \cdot (\sigma \nabla V) = 0 \quad \text{(A.9)}$$

The FD method, the EJFD method and the random walk method are explained in more detail in Section 3.2.

A.3 Permeability

For atmospheric entry, ablators materials are used as TPS. These materials are highly porous, which means that the gas can easily flow within these materials. As a result, it is important to understand how this will affect the overall material response [26]. To do so, it is key to compute permeability, K, since it measures the capacity and ability of that fluid to flow through a porous material.

In PuMA, the permeability is determined by solving the Stokes equation A.10, only valid for slow creeping regimes ($Re \approx 0$), in which permeability is a material property depending on the microstructure.

$$-\mu\nabla^2\boldsymbol{u} + \nabla p = \boldsymbol{f} \quad \text{(A.10)}$$

There are two ways to approximate and solve the Stokes equation. One method imposes a pressure gradient in the three Cartesian directions, creating a velocity field through the domain. Then, the mean velocity throughout the domain can be inserted into Darcy´s law to give effective permeability. Another approach is to impose a body force yielding a mean flow rate that will also be input into Darcy´s equation, from which it is possible to retrieve the permeability. This is solved using finite element analysis. Two discretization methods are implemented in PuMA. The first one uses first-order elements in both pressure and velocity, requiring the addition of a pressure stabilization term. The second employs Taylor-Hood second-order elements in pressure, resulting in a more stable analysis. As a result, by applying a unit body force in three Cartesian directions, the homogenized permeability effective tensor, as shown in equation A.11, can be obtained.

$$\begin{bmatrix} K_{xx} & K_{xy} & K_{xz} \\ K_{xy} & K_{yy} & K_{yz} \\ K_{xz} & K_{yz} & K_{zz} \end{bmatrix} = \frac{l^3}{|V|}\int_V u_i dV \quad \text{(A.11)}$$

A.4 Material response

As described above, this is only a feature present in version 2.0 of the software and includes an implementation of a microscale oxidation model. It attempts to replicate some of the physics involved in a high-temperature decomposition, in this case, of carbon materials. Studies have shown that quantifying the oxidation of preform materials is crucial since it is one of the main decomposition mechanisms of fibrous carbon/phenolic ablators [81]. It is driven by the reactant diffusion inside the porous media and reaction rates at the fiber surface. In highly porous materials, where the reactive gases can percolate in-depth, the oxidation phenomena should be considered at the scale of the fibers. Lauchaud and Vignoles [80] presented a method for this problem. A Brownian motion is used to represent the gas-surface interactions during ablation, and Random Walk rules are presented close to the fibers to effectively simulate mass transfer in low Péclet numbers (Pe). It was later applied on artificially generated materials [81].

In PuMA, this is achieved with a basic single value reaction model as a function of temperature and diffusion of oxygen as particles. Using this model, it is feasible to assess the evolution of the effective material properties during the decomposition of carbon fibers due to their interaction with oxygen reactants. It also allows for studying the oxidation of the phenolic resin used in the ablative materials by adding a second material phase. Figure A.1 showcases an example of microscale oxidation simulated on PuMA of fiberForm, the carbon preform of the carbon/phenolic ablator PICA used in ablative thermal protection systems.

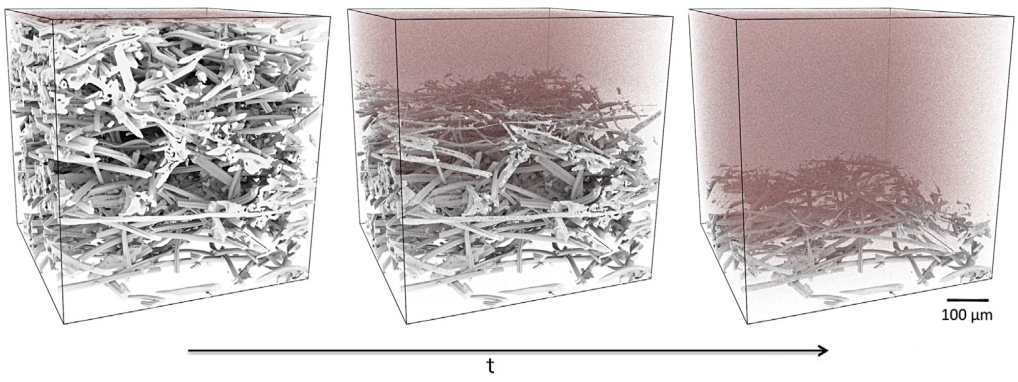

Figure A.1: Microscale oxidation simulation on a carbon fiber preform material, fiberForm [13].

Appendix B

Conference abstract

The annual Ablation Workshop provides a platform for the interdisciplinary research community of worldwide scientists and engineers working on aerothermodynamic ablation. The goal of this conference is to encourage increased cross-national communication, bringing new experimental approaches, sharing new ideas and discussing the difficulties encountered in adjusting existing techniques to new applications. Promoting innovation through collaboration allows for rapid development in this field.

This year the 12^{th} Ablation Workshop conference took place in Lexington, Michigan, US, from 9 to 10 of November.

Simulation of heat transfer of carbon fibers felts and microstructure effects on thermal conductivity of carbon/phenolic ablators

D. Martins[a,b], F. Torres-Herrador[b], B. Helber[b], A. Turchi[b], P. Gamboa[c], T. Magin[b]

[a] *Department of Aerospace Sciences, Universidade da Beira Interior, Covilhã, Portugal*
[b] *Aeronautics and Aerospace department, von Karman Institute for Fluid Dynamics, 1640 Rhode Saint Genese, Belgium*
[c] *Centre for Mechanical and Aerospace Science and Technologies (C-MAST-UBI), Universidade da Beira Interior, Covilhã, Portugal*

Abstract

Accurate modeling of the thermal response of Thermal Protection Systems (TPS) requires adequate characterization of thermophysical properties. According to the literature [1], the effective thermal conductivity of carbon/phenolic ablators is one of the significant factors of heat transfer towards the interior of the material. It is primarily driven by the intrinsic thermal conductivity of carbon fibre felts and it is influenced by the geometry and arrangement of the constituents. With increased computational capabilities, numerical simulations of materials at microscale resolution have become more affordable. These simulations allow obtaining effective properties, which can be used in volume-averaged design codes, minimizing the need for expensive experimental campaigns. For example, one can simulate the heat transfer inside a carbon fiber felt and obtain the effective thermal conductivity. This can be achieved with the Porous Microstructure Analysis software (PuMA) and its Python version pumapy, developed by NASA Ames Research Center. [2, 3]. In this work, we have analysed the effect of the microstructure and the different intrinsic properties on the effective thermal conductivity.

The first step consisted in developing a numerical model for CALCARB 18-2000, the carbon preform of the material in the study, ZURAM, by artificially generating a transverse isotropic material with a normal distribution in the Through-Thickness (TT) and a uniform distribution in the In-Plane (IP). This material model was verified and validated from available experimental measurements furnished by the manufacturer [4, 5]. For the thermal simulation, it is necessary to know the intrinsic conductivity of each material constituent. The intrinsic conductivity of the fibers was obtained from Pradere [6], while the conductivity of the gas was determined using Mutation++. Therefore, it was possible to conduct a general parametric study to evaluate the impact of microscopical parameters on thermal conductivity, such as porosity, fiber length and diameter and angular variation of the fiber orientation on the developed numerical model of CALCARB. Afterwards, a sensitivity analysis based on a surrogate model was performed to quantify how the previous most important parameters, such as porosity, fiber length and angular variation, influence the overall performance of porous materials. We observe that for the IP direction, porosity has a more considerable influence on the thermal conductivity, whereas in the TT plane is the fiber orientation and that porosity and angle associated have a considerable effect. The results of this analysis are showcased in Figs. 2 to 4.

In addition, two cases have been analyzed: charred and virgin carbon/phenolic materials. The char resulting from pyrolysis, as depicted in Figure 1, leads to a variation in the overall material's porosity and effective thermal conductivity. Hence, it is necessary to accurately characterize the material's thermal response after pyrolysis. A geometry generator for the material in the charred state that creates a uniform coating on top of the fiber by generating a coaxial cylinder was developed in pumapy. This code was later applied to compare the simulation results to the available experimental data [7] to understand if the developed numerical tool can accurately simulate the material's thermal response after pyrolysis. To study the virgin carbon/phenolic, it must be taken into account that the material comprises fibers, gas and phenolic resin. A new material generator has been implemented which combines the previous code developed for CALCARB with a generation of uniformly distributed voxels in the domain that mimics the gas trapped inside the material. In the latter, the medium represents the phenolic resin. Finally, the effect of the change in the conductivity due to the graphitization of the fibers was also evaluated.

The results obtained in both thermal simulations differ from the experimental results. Even though it is fair to say that there is an agreement between the behaviour of the simulated and measured conductivities, the disparity can reside in the fact that some of the properties are not known. For the coating simulation, the charred resin's intrinsic

conductivity is unknown. In the case of the virgin material simulation, the resin's and the fibres' intrinsic conductivity at the experiments' temperature are also unknown. These factors, along with the simplicity in the assumption for both geometry generations, can lead to an error in the output of the effective thermal conductivity simulations.

This work provides important information about the effect of the different components and geometrical features of the microscopic properties of porous ablative materials on their macroscopic model evaluation.

As further developments, the artificially generated material models should be improved since they require adjusting the assumptions to consider a more realistic physical geometry. The charred and virgin resin conductivities should be assessed with experimental measurements. Extrapolation of the intrinsic conductivity of the fibers at temperatures not referred to in the literature should be carefully evaluated and validated. The inability to account for the impacts of radiative heat transport on thermal models at high temperatures should be solved.

Keywords: Thermal protection systems, carbon/phenolic ablators, thermal conductivity, microscale numerical simulations

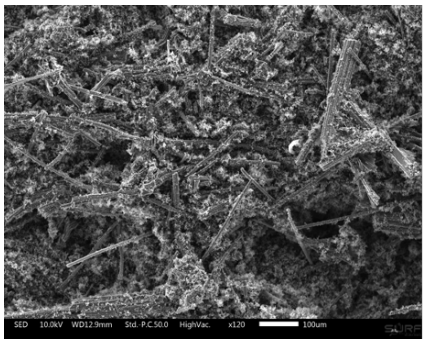

Figure 1: SEM picture of ZURAM at a charred state [7].

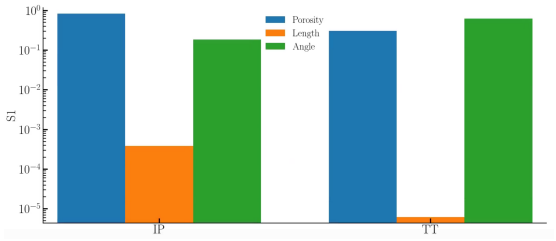

Figure 2: First-order indices. The blue bar represents the influence of porosity, the orange bar the effect of length and the green bar the impact of the fiber's orientation on the effective thermal conductivity.

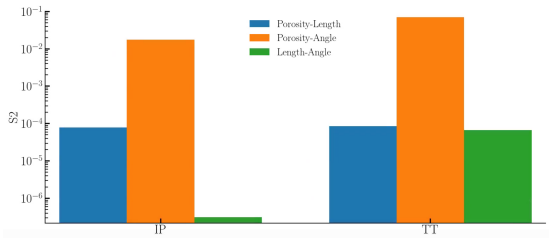

Figure 3: Second-order indices. The blue bar represents the influence of porosity-length, the orange bar the effect of porosity-angle and the green bar the impact of the fiber's length-angle on the effective thermal conductivity.

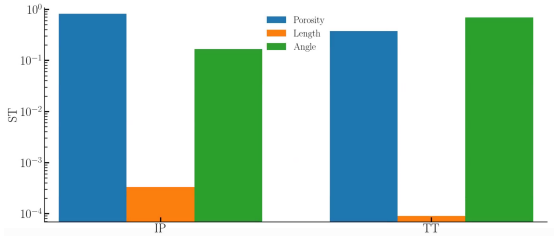

Figure 4: Total-order indices. The blue bar represents the influence of porosity, the orange bar the effect of length and the green bar the impact of the fiber's orientation on the effective thermal conductivity.

References

[1] M. Rivier, J. Lachaud, P. Congedo, Ablative thermal protection system under uncertainties including pyrolysis gas composition, Aerospace Science and Technology 84 (2019) 1059–1069. doi:https://doi.org/10.1016/j.ast.2018.11.048.

[2] J. C. Ferguson, F. Panerai, A. Borner, N. N. Mansour, Puma: The porous microstructure analysis software, SoftwareX 7 (2018) 81–87.

[3] J. C. Ferguson, F. Semeraro, J. M. Thornton, F. Panerai, A. Borner, N. N. Mansour, Update 3.0 to puma: The porous microstructure analysis software, SoftwareX 15 (2021) 100775.

*Corresponding author.
Email address: diana.martins@vki.ac.be (D. Martins)

[4] Mersen, Properties of calcarb, rigid carbon insulation CBCF 18-2000, Tech. rep., Mersen (February 2009).
[5] Mersen, Calcarb rigid carbon insulation, Tech. rep., Mersen (February 2013).
[6] C. Pradere, J. Batsale, J. Goyhénèche, R. Pailler, S. Dilhaire, Thermal properties of carbon fibers at very high temperature, Carbon 47 (3) (2009) 737–743. doi:https://doi.org/10.1016/j.carbon.2008.11.015.
URL https://www.sciencedirect.com/science/article/pii/S0008622308006015
[7] A. Turchi, F. Torres Herrador, B. Helber, G. Pintsuk, C. Zuber, H. Ritter, T. Magin, Thermal conductivity evolution of carbon-fiber ablators submitted to high temperatures, Journal of Thermophysics and Heat Transfer (2022) 1–11doi:10.2514/1.T6485.